

Femtosecond pulse length and arrival time measurement of hard X-Ray FELs

THÈSE N° 7370 (2016)

PRÉSENTÉE LE 16 DÉCEMBRE 2016

À LA FACULTÉ DES SCIENCES DE BASE

LABORATOIRE DE PHYSIQUE DES ACCÉLÉRATEURS DE PARTICULES

PROGRAMME DOCTORAL EN PHYSIQUE

ÉCOLE POLYTECHNIQUE FÉDÉRALE DE LAUSANNE

POUR L'OBTENTION DU GRADE DE DOCTEUR ÈS SCIENCES

PAR

Ishkhan GORGISYAN

acceptée sur proposition du jury:

Prof. F. Mila, président du jury
Prof. L. Rivkin, Dr R. Ischebeck, directeurs de thèse
Prof. J. Hastings, rapporteur
Prof. T. Feurer, rapporteur
Prof. F. Carbone, rapporteur



ÉCOLE POLYTECHNIQUE
FÉDÉRALE DE LAUSANNE

Suisse
2016

Think of your life as a greatest miracle
and it will become one.
— Tvigern

To Samvel Gorgisyan and Gohar Israyelyan...

Acknowledgements

I would like to express my deepest gratitude to my three supervisors, who have guided me throughout my thesis and taught me so much, and without whom it would be impossible to accomplish this project; Leonid Rivkin for constructive criticism, his valuable advice and support, Rasmus Ischebeck for his supervision, his endless positivity and for motivating and helping me to develop as a researcher, and Pavle Juranic for sharing his experience and knowledge with me, for all the fruitful discussions, for his assistance and guidance to keep me on the right track in the project. I further thank Luc Patthey, Rafael Abela and Christoph Hauri for supporting the measurements performed during my thesis. Special gratitude to Sven Reiche and Eduard Prat for helping me to interpret some measurement results and explaining different phenomena of the FEL process. I thank the colleagues from SACLA for providing a great support during the measurements, particularly to Makina Yabashi, Shigeki Owada, Tetsuo Katayama and Tadashi Togashi. Special thanks to the technical staff at PSI and SACLA for helping during the preparations for the measurements, especially to Beat Rippstein, who also practiced German with me. I thank my colleagues from the Advanced Instrumentation group, who always gave useful feedback to my work. In addition to my group, I am also thankful to the Beam Dynamics group for the nice discussions over lunch and coffee breaks, for ping-pong matches and table-soccer battles. I would like to thank all my colleagues and collaborators, who helped me during my PhD and contributed to my growth as a scientist.

I want to thank all my friends for making my life so bright, colorful and full of adventures during these exciting years of my PhD. I can never thank my family enough, who was always there for me, supported me in everything and made me the person I am now, with special thanks to my wife Jenny Gorgisyan for motivating and inspiring me.

I am also grateful to Frédéric Chopin, Johann Sebastian Bach, Giuseppe Verdi and Antonio Vivaldi for their priceless works that inspired me and kept me focused during my work, as well as to Paco, Swift Guad, D12 and Stromae for giving me extra motivation when I needed it the most.

PSI, 21 September 2016

I. Gorgisyan.

Preface

Free electron lasers have become the brightest X-rays sources in the world, enabling scientists to perform research on the dynamics of molecular systems by providing femtosecond X-ray pulses. The metrology for the arrival time and pulse length plays a central role for time-resolved experiments. This work presents the first measurement of pulse length and arrival time of hard X-rays, with photon energies up to 10000 eV. It is based on terahertz streaking of photoionized electrons generated by the X-ray pulse in a dilute gas target. As such, this diagnostics is transparent and can be operated along user experiments. The instrument developed in the framework of this thesis will be used for the temporal characterization of the X-ray pulses in SwissFEL, and will provide users with valuable diagnostics of pulse arrival time and pulse length.

The present manuscript details the construction of the chamber, first tests using a high harmonic laser-based source, and measurements at the free electron laser SACLA at SPring-8 in Japan. This also includes the individual measurement of the two pulses in the two-color mode, a recent upgrade of the facility that provides two overlapping X-ray pulses with different wavelength and variable delay that can be used for pump-probe experiments.

PSI, 02 September 2016

Abstract

The ultra-bright short-pulsed radiation provided by the free electron lasers (FEL) is used for many new discoveries in different fields of science and industry. The advancement of the FEL technologies allows the generation of shorter photon pulses with higher photon energies or shorter radiation wavelengths that open new horizons for the new research. In order to better understand the measurements using the free electron laser pulses, it is important to know the properties of these pulses. Particularly, for the time-resolved experiments the temporal properties of the photon pulses such as their relative arrival times and the temporal durations, are of utmost importance.

One of the techniques to measure these parameters of the FEL pulses is the THz streaking method. Thus far, this method has been used only for the photon pulses in ultraviolet and soft X-ray regions. This thesis provides a full characterization of the method and demonstrates its applicability in the hard X-ray photon energy range, measuring FEL pulses with photon energies of up to 10000 electronvolts. Measurement accuracies of sub-10 femtoseconds were achieved for both the arrival time and the pulse length measurements. Furthermore, it is shown here that the THz streaking method is able to simultaneously measure two FEL pulses of different energies. The results from some measurements were also compared to other independent measurement techniques.

In addition to the performed measurements, simulation of the THz streaking effect was performed to better understand the measurement method. The simulations showed the ways of achieving higher accuracies with the THz streaking techniques. The results obtained from the experiments were consistent with the results provided by the simulations.

The results obtained in this thesis provide new possibilities for the applications of the THz streaking method. They enable temporal diagnostics for photon pulses with a wide range of wavelengths and temporal durations. Such diagnostics can contribute largely to the success of the experiments performed at free electron laser sources.

Key words: Free electron laser, Temporal diagnostics, Femtosecond metrology, THz streak camera, Electron time-of-flight spectrometers, High harmonic generation, Hard X-ray

Zusammenfassung

Freie-Elektronen-Laser (FEL) generieren kurze Pulse extrem brillanter Röntgenstrahlung, welche für viele Entdeckungen in verschiedenen Gebieten der Wissenschaft und Industrie verwendet werden. Der Fortschritt in der FEL-Technologie erlaubt die Erzeugung von kürzeren Photonenpulsen mit höherer Photonenenergie, entsprechend kürzerer Wellenlänge, welches neue Horizonte für die Forschung öffnet. Um Messungen mit den Pulsen von Freie-Elektronen-Lasern besser zu verstehen, ist es wichtig, die Eigenschaften dieser Pulse zu kennen. Insbesondere für zeitaufgelöste Experimente sind Eigenschaften wie ihre relative Ankunftszeit und Pulsdauer von höchster Wichtigkeit.

Eine der Möglichkeiten, diese Parameter von FEL-Pulsen zu messen, ist die Methode des THz Streaking. Bis dahin wurde diese Methode nur für Photonenpulse im weichen Röntgenbereich verwendet. In dieser Doktorarbeit wird die Methode vollständig charakterisiert, und die Anwendbarkeit für harte Röntgenstrahlen demonstriert, bei Photonenenergien von bis zu 10000 Elektronenvolt. Messgenauigkeiten von besser als 10 Femtosekunden wurden sowohl für die Ankunftszeit- als auch die Pulslängenmessung erreicht. Darüberhinaus wird hier gezeigt, dass die THz-Streaking-Methode in der Lage ist, simultan die Ankunftszeit von zwei FEL-Pulsen unterschiedlicher Energie zu messen. Die Ergebnisse dieser Messungen werden mit unabhängigen Methoden verglichen.

Zusätzlich zu diesen Messungen wurden Simulationen des THz-Streaking-Effekts durchgeführt, um die Messmethodik besser zu verstehen. Diese Simulationen zeigen den Weg, mit THz-Streaking-Methoden eine höhere Genauigkeit zu erreichen. Die Ergebnisse der Experimente sind im Einklang mit den Resultaten der Simulationen.

Die Resultate dieser Doktorarbeit zeigen neue Anwendungsmöglichkeiten der THz-Streaking-Methode auf. Sie ermöglichen eine zeitaufgelöste Diagnostik von Photonenpulsen mit einer weiten Spanne von Wellenlängen und Pulsdauern. Eine solche Diagnostik kann entscheidend zum Erfolg von Experimenten an Freie-Elektronen-Lasern beitragen.

Stichwörter: Freie-Elektronen-Laser, zeitaufgelöste Diagnostik, Metrologie für Femtosekundenpulse, Terahertz-Streak-Kamera, Elektronen-Flugzeitspektrometer, Erzeugung höherer Harmonischer, harte Röntgenstrahlen

Contents

Acknowledgements	i
Preface	iii
Abstract (English/Deutsch)	v
List of figures	xi
List of tables	xv
List of abbreviations	xvii
Introduction	1
1 Theory	5
1.1 FEL radiation	5
1.1.1 Undulator radiation	5
1.1.2 Low-gain FEL regime	6
1.1.3 SASE FEL regime (high-gain mode)	8
1.2 Methods for temporal diagnostics of pulses	9
1.3 Photoionization in external streaking field	12
1.3.1 Quantum model	12
1.3.2 Semiclassical model	15
1.3.3 Photon pulse length calculation	16
1.4 THz generation	18
1.5 High harmonic generation	21
2 Simulation of the streaking process	25
2.1 Simulation model	25
2.2 Simulation procedure	27
2.2.1 Simulation of the FEL pulses	28
2.2.2 Simulation of the ionization and streaking	28
2.2.3 Pulse length calculation	29
2.3 Results of simulation and discussion	31

Contents

3	Experimental setup	37
3.1	Prototype setup	37
3.2	Second generation setup	41
3.3	Accuracy considerations for the experimental setup	43
4	Measurements	49
4.1	Measurements with an HHG source	49
4.1.1	Measurement procedure with the HHG pulses and data processing	49
4.1.2	Results of the HHG measurements	56
4.2	First measurements of hard X-ray FEL pulses at SACLA	60
4.2.1	Procedure of FEL pulse measurement and data processing	61
4.2.2	Results from the first FEL measurements	70
4.3	FEL measurements with the second generation setup	75
4.3.1	Single-shot measurement procedure and the data processing	76
4.3.2	Results from the single-shot measurements	83
5	Discussion	91
5.1	Discussion of the experimental results	91
5.2	Outlook	98
6	Conclusion	101
A	Simulation code in MATLAB	103
	Bibliography	118
	Curriculum Vitae	119

List of Figures

1.1	Demonstration of the streaking process. The photoelectron spectra become broader because of the streaking by the laser field.	17
1.2	Schematic view of the velocity matching using the tilted pulse front method.	19
2.1	Energy spectra (a) and temporal profiles (b) of two photon pulses for Swiss-FEL long-pulse (blue) and short-pulse (red) operation modes and the Gaussian spectrum corresponding to a 50 as mean ionization time (green).	26
2.2	Energy distribution of the photoelectrons generated by the simulation. Distributions (a) and (b) correspond to the electrons created by a 1.5 fs-long pulse and show the non-streaked and streaked spectra, respectively. Analogously, (c) and (d) are the corresponding spectra of electrons from a 16 fs-long photon pulse.	30
2.3	Simulation results for Gaussian fitting (a) and the rms widths (b). The blue diagonal line represents the initial rms pulse lengths, the green triangles and the red circles are the calculated average lengths for photon energies of 12400 eV and 1240 eV, respectively. The vertical bars correspond to the standard deviations from 100 shots.	33
2.4	Subfigures (a) and (b) show the absolute accuracies, while (c) and (d) show the standard deviations from 100 simulations for each pulse length. The plots on the left correspond to photon energy of 12400 eV, and the ones on the right - to 1240 eV. The blue circles indicate the results from Gaussian fitting whereas the red crosses show the results from the method using the rms widths.	34
3.1	Schematic view of the prototype PALM setup. The red arrow represents the X-ray beam while the blue line corresponds to the streaking THz pulse that enters the chamber from the side. The gas jet shown by a brown arrow comes from the top.	38
3.2	Graphical view of the eTOF and the trajectories of the electrons tracked by SIMON simulation tool.	40
3.3	Outline of the second generation PALM setup with two interaction regions. The pink and green arrows show the FEL and THz beams, respectively. The two gas jets are shown by the red arrows. The THz radiation is generated on the optical table positioned next to the vacuum chamber.	42

List of Figures

3.4	Illustration of the Gouy phase shift effect. The THz beam shown in blue is focused at the position $z = 0$ and it experiences a phase shift along the interaction region.	44
4.1	Spectrum of the HHG pulse containing the harmonics from 15th to 31st, measured by a grating spectrometer.	50
4.2	Photoelectron spectra from xenon gas (a) and helium gas (b) measured by eTOF spectrometers and averaged for 100 consecutive spectra. The spectra are shown in terms of flight time and each spike corresponds to a certain kinetic energy of the electrons shown in the figure.	51
4.3	Calibration curves for eTOF1 (a) and eTOF2 (b). The red circles correspond to the data points and the green lines show the fitted curves.	52
4.4	The change of the photoelectron spectra during the delay scan between the THz pulse and the HHG pulse. Subfigure (a) corresponds to the scan with Xe, while (b) shows the results for He gas.	53
4.5	Gaussian profiles with linear background fitted to each spike of the measured spectra. The blue dots correspond to the measured points while the red lines show the fitted curves.	54
4.6	Spectrum from the two electron shells of Xe corresponding to the 27th harmonic of HHG, and a double Gaussian profile fitted to it. The blue dots correspond to the measured points while the red line shows the fitted curve.	55
4.7	The durations of the five different harmonics calculated from the measurements at the second slope of the vector potential.	58
4.8	Electric field of the THz pulse calculated from the measurements. The blue line corresponds to the measurements from eTOF1, while the green line shows the field obtained from eTOF2.	59
4.9	The change of the flight time of the electrons measured by eTOF1 during the calibration scan for the photon energy of 9000 eV. Each waveform in the figure corresponds to the value of the retarding voltage indicated on the right part of the figure.	63
4.10	Calibration curves of eTOF1 (a) and eTOF2 (b) from the measurements with a photon energy of 5000 eV. The red circles correspond to the data points and the green lines show the fitted curves.	64
4.11	Normalized spectra of the photoelectrons from the two eTOFs during the delay scan at 9000 eV photon energy. The subfigures on the left correspond to the pink beam, while the ones on the right correspond to the beam with the monochromator.	65
4.12	Distributions of the shifted energy peak positions at the minimum (a), linear part (b) and the maximum (c) of the vector potential. The histograms correspond to the measurements with a photon energy of 10000 eV.	66

4.13	Linear area of the THz vector potential before the correction shown in blue and after the correction shown in red. The green and the cyan circles show the average values of the 10 largest absolute energy shifts, respectively, in direction of the THz field and opposite to it.	67
4.14	Gaussian fits (blue curves) applied to a streaked (green circles) and a non-streaked (red crosses) photoelectron spectra.	68
4.15	The dependence of the rms widths of the spectra on the central energies for the two eTOFs and the corresponding 3rd order polynomial fits. The plots correspond to the calibration measurements with the 9000 eV photon beam with the monochromator. The vertical bars correspond to the standard deviation from 100 measurements.	70
4.16	Distributions of the FEL arrival times relative to the experimental laser for different photon beams.	72
4.17	Distributions of the rms FEL pulse durations measured for different photon beam configurations.	74
4.18	Electric field strength of the THz pulse reconstructed from the delay scan measurements.	75
4.19	The schematic view of the SACLA photon diagnostics system and the experimental setup in the experimental hutches.	76
4.20	Calibration curves and the corresponding coefficients obtained for all three eTOFs. Subfigures (a), (b) and (c) show the results for eTOF1, eTOF2 and eTOF3, respectively.	78
4.21	Evolution of the normalized spectra during the delay scan between the FEL and the THz beams. The plots on the left side show the scan during the standard operation mode with 9000 eV photon beam, while the ones on the right side correspond to the operation in 2-color mode.	79
4.22	The energy shifts of the photoelectron spectra during the delay scan. The curves in blue and red show the energy shifts of the spectra measured by eTOF1 with respect to eTOF3 before and after correction, respectively. The curves in green and magenta correspond to the energy shifts relative to eTOF3, respectively, before and after correction measured by eTOF2.	80
4.23	Normalized photoelectron spectra measured by all three eTOFs for the single-color 9000 eV photon energy mode (a) and the 2-color mode (b). The spectra correspond to the arrival of the FEL pulses at the linear part of the THz vector potential.	82
4.24	Comparison of the arrival time measurements from PALM and SACLA time monitor. Subfigure (a) shows the distribution of the difference between the two methods, (b) shows the correlation between the two measurement values and (c) shows the arrival time values measured by the two methods.	84
4.25	The delay values between the two FEL pulses set by the magnetic chicane and measured by the THz streak camera.	85
4.26	Distributions of the rms FEL pulse durations measured during different runs.	87

List of Figures

4.27	Electric field of the THz pulse reconstructed from the measurements with eTOF1 (blue curve) and eTOF2 (red curve).	89
5.1	Pulse lengths depending on the photon energy (a) and the time of the measurements (b). Letters (p) and (m) in X-axis of (b) denote pink and monochromatic beams, respectively.	92
5.2	Energy spikes from the FEL spectra measured by the high-resolution spectrometer of SACLA. The red crosses correspond to the measured points in the spikes.	95
5.3	Energy spectra of different FEL pulses measured by the wide bandwidth spectrometer of SACLA.	96
5.4	The concept of PALM performance with a large dynamic range utilizing two THz pulses with 90° shift between each other.	99
5.5	Sketch showing the concept of high-resolution measurement mode with two THz pulses. The first THz pulse has longer duration but smaller electric field, while the second one has a shorter duration but a stronger field.	100

List of Tables

2.1	Photon pulse lengths calculated by performing Gaussian fits. Mean values of the obtained lengths (Calc. mean) with their standard deviations (St. dev.) and accuracies (Acc.) are compared with the initial lengths (Initial).	31
2.2	Photon pulse lengths calculated using the rms widths of the spectra. Mean values of the obtained lengths (Calc. mean) with their standard deviations (St. dev.) and accuracies (Acc.) are compared with the initial lengths (Initial).	32
4.1	The rms durations of the HHG pulses calculated using Xe for different harmonics with their standard deviations from 4 different calculations and the obtained linear chirps. The results are presented for the streaking at the two slopes of the THz pulse including also the corresponding streaking strengths.	56
4.2	The rms jitter of the FEL pulses relative to the THz pulses for different photon beams. The terms ‘pink’ and ‘mono’ correspond to the beam without the monochromator and with it, respectively.	71
4.3	The average FEL pulse lengths and their standard deviations for different photon beams, uncertainties from the eTOF measurements and the average chirps.	73
4.4	Comparison of the relative arrival time measurements from PALM and the SACLA timing tool for 5 different runs. The rms jitter between the two measurements and the total uncertainty from both of the monitors are presented as well as the correlation coefficients.	83
4.5	The average FEL pulse lengths and their standard deviations for different runs, uncertainties from the eTOF measurements and the average chirps.	86
4.6	Average rms durations of the FEL pulses and their standard deviations measured during the 2-color operation mode for different delay values. The measurement accuracy of the eTOFs, pulse length jitter and the linear energy chirp are presented for each FEL pulse.	88

List of Abbreviations

FEL	Free Electron Laser
PSI	Paul Scherrer Institut
RF	Radio Frequency
IR	Infrared
FWHM	Full Width at Half Maximum
RMS	Root Mean Square
SASE	Self-amplified Spontaneous Emission
UV	Ultraviolet
TDC	Transverse Deflecting Cavity
HHG	High Harmonic Generation
eTOF	Electron Time-of-flight Spectrometer
PALM	Pulse Arrival and Length Monitor
MCP	Microchannel Plate
EH	Experimental Hutch
BL	Beamline
DCM	Double-crystal Monochromator

Introduction

In the recent years there has been a growing scientific interest in free electron lasers (FELs), the brightest sources of short-pulsed coherent X-ray radiation in the world [1, 2]. Free electron lasers are able to produce radiation pulses in both soft and hard X-ray regions with typical pulse lengths of tens of femtoseconds or shorter ($1 \text{ fs} = 10^{-15} \text{ s}$). At such short pulse lengths a peak radiation power of about 10 GW can be achieved, which is orders of magnitude higher than at the 3rd generation synchrotron light sources. At present there are several operating FEL facilities around the world, such as the Free electron LASer in Hamburg (FLASH) at DESY in Germany [3], the Linac Coherent Light Source (LCLS) at Stanford in USA [4], FERMI at ELETTRA in Italy [5] and the SPring-8 Angstrom Compact free electron LASer (SACLA) in Japan [6]. Apart from these fully operational machines there are also some upcoming facilities as the XFEL at Pohang Accelerator Laboratory (PAL) in South Korea [7, 8], the European XFEL in Germany [9] and the Swiss Free Electron Laser (SwissFEL) at Paul Scherrer Institute (PSI) in Switzerland [10]. The total length of the SwissFEL facility is only about 800 meters, consisting of an electron source (photo-cathode with an RF gun), a compact linear accelerator of 5.8 GeV, permanent magnetic undulators and photon beam lines for the experiments. The first beam line to be commissioned in 2017 is Aramis. It will provide hard X-ray radiation pulses at wavelengths between 0.1 nm and 0.7 nm with linear polarization and photon pulse lengths of 20 fs and 2 fs for standard and short-pulse operation modes, respectively.

The exceptional power of FEL radiation has been extensively used in different fields of science and industry, contributing to many new discoveries in biochemistry, material science, nanotechnology, atomic spectroscopy, molecular biology and many more. The short radiation wavelengths and the pulse durations in the femtosecond range allow the users to penetrate into molecular and atomic scales and observe dynamic processes in ultrafast time domain. FEL radiation is used for imaging nanostructure objects, studies of electron dynamics in atoms, spectroscopy of plasmas, generation of new states of matter etc. Typical experiments most commonly carried out at FEL facilities are the pump-probe experiments, where a sample is first pumped by the experimental laser and then probed by the FEL pulse to observe the changes in the sample caused by the pumping laser pulse. The resolution of such measurements is mostly dependent on the pumping and probing pulse durations and the stability of the time delay between these two pulses. It is possible to improve the resolution of these experiments by closely monitoring the temporal properties of the FEL pulses. Characterizing the arrival times and lengths of X-ray pulses delivered by the FEL facilities not only helps the

Introduction

users to perform high-resolution measurements and better understand their results, but also provides useful information for the operators to set up the machine itself and monitor its operation stability. Providing comprehensive and accurate temporal diagnostics for photon pulses in femtosecond timescale is, however, challenging.

With the advancement of FEL technologies several methods have been proposed and developed for accurate measurements of the FEL pulse durations and their arrival times relative to the experimental laser. The most common technique to measure the arrival time is the temporal cross-correlation of the FEL pulses with the experimental optical laser using the X-ray induced transient transmission/reflectivity change to encode the arrival time in the spectral [11] or spatial [12, 13, 14] profiles or the intensity [15, 16] of the optical laser. Another method used at FLASH measures the arrival time of the X-ray pulse by cross-correlation of the optical laser with THz coherent edge radiation emitted by the electron bunch synchronously with the FEL [17]. A recent arrival time measurement at LCLS with a spatial encoding setup achieved a temporal resolution of sub-femtosecond using a soft X-ray beam of 800 eV [18]. Various methods currently exist also for the measurement of the temporal duration of X-ray FEL pulses, such as measuring the electron bunch temporal profile with a radio-frequency (RF) deflecting cavity after FEL radiation [19], measuring the spike widths of the FEL energy spectra [20], cross-correlation of the FEL pulse with an optical laser using transient transmission [21] and others [22, 23, 24].

Aside from the mentioned methods, streak camera is another technique capable of simultaneously measuring both the pulse lengths and the relative arrival times of light pulses. The concept of the conventional streak camera is to use a photocathode to generate photoelectrons from the photon pulses with the photoelectric effect [25]. The temporal structure of the electrons mimics that of the photon pulse, which is then converted to transverse distribution by applying a time-varying electric field to the electrons. Measuring the spatial distribution of the photoelectrons and knowing the speed of the electric field change, the temporal properties of the photon pulses can be extracted. The conventional streak cameras can measure the photon pulse lengths with an accuracy of few hundreds of femtoseconds [26, 27], being limited by the strength and the frequency of the streaking electric field. Additional uncertainty comes from the energy dispersion of the electrons from the photocathode. In order to improve the resolution of the measurements it has been suggested [28, 29, 30, 31, 32] to use a gas target instead of the photocathode and utilize terahertz (THz) or infrared (IR) radiation to streak the electron spectra with much faster oscillating electric fields. The light-field streaking idea was first applied for free electron lasers at DESY, measuring soft X-ray pulses with an accuracy of a few femtoseconds [33, 34, 35, 36]. Recent measurements performed at LCLS used a near infrared laser (wavelength of $2.4 \mu\text{m}$) for streaking to measure FEL pulses with a duration as short as 4.4 fs full width at half maximum (FWHM) [37] at a photon energy of about 1800 eV. Until now, the light-field streaking method has not been applied to measure FEL pulses in the hard X-ray region with photon energies higher than 2000 eV. The difficulty for the THz/IR streak camera that appears at high photon energies is caused by the fact that the photoionization cross-section of the gas target in the streak camera is a few orders of magnitude smaller compared to the cross-section for soft X-ray photons [38]. This reduces the number of created

photoelectrons, causing large statistical fluctuations in their energy spectra.

The goal of this thesis is to apply the light-field streaking method for hard X-ray pulses with photon energies up to 10000 eV and higher, equivalent to a radiation wavelength of 1.24 Å (1 Ångström = 10^{-10} m). More specific objectives are to simulate the photoionization, the streaking process and the operation of the streak camera, design and assemble a system for hard X-ray FEL pulse measurements and perform proof-of-concept measurements with the setup at an operating FEL beamline. The aim of this work is to achieve an accuracy of sub-10 femtoseconds in root mean square (rms) for both the pulse length and the relative arrival time measurements.

The experimental setup assembled for the measurements will be further used at SwissFEL for temporal photon diagnostics, providing valuable information both for the operators and the users of the facility. This measurement system must be transparent for the FEL beam and should provide diagnostics without affecting the properties of the FEL pulses. It should also be capable of measuring the FEL pulses on a single-shot basis delivering the pulse length and the relative arrival time of every FEL pulse.

The material given in this thesis is structured as follows. The first chapter discusses the theory of various physical phenomena that were used in this project, the second chapter gives a description of a simulation procedure that models the performance of the THz streak camera. Chapter three provides an overview of the experimental setup that was used during the measurements. All the measurements carried out during this project and the results obtained from them are described in chapter four. The fifth chapter gives a comprehensive discussion about the measurements and the obtained results, discussing also possible ways of improving the current method, while the sixth chapter draws some conclusions about the performed work and achieved results.

1 Theory

This chapter presents a brief overview of several phenomena that are relevant for understanding the concept of the light-field streaking method and different measurements performed by the experimental setup. The chapter also discusses various measurement techniques that are currently being used for the temporal photon diagnostics.

1.1 FEL radiation

In order to proof the concept of this thesis, measurements have been performed using FEL beam. This section provides an overview of the FEL radiation theory and describes the origin of different properties of the FEL pulses. Most of the derivations written in this section are based on [39] and [40].

1.1.1 Undulator radiation

It is well known that the relativistic charged particles emit electromagnetic radiation while undergoing a circular motion [41]. When an electron passes through a periodic array of magnets of opposite polarities, called undulator, it follows a periodic wiggling motion [42]. Such a motion is a simple transverse oscillation in a reference frame co-moving with the particle in the longitudinal direction. In this frame the oscillating particle emits radiation with a wavelength related to the oscillation frequency, which is given by the period of the undulator λ_u . As the undulator period length is Lorentz-contracted in the co-moving frame, the radiation wavelength in this frame can be written as $\lambda_\gamma^* = \lambda_u / \hat{\gamma}$, where $\hat{\gamma}$ is the Lorentz factor defined by the longitudinal velocity of the electron. When observing in the laboratory frame, the radiation emitted in different directions due to the oscillations of the particle, experience different Doppler shifts. Applying the Lorentz transformation from the co-moving frame to the laboratory frame and taking into account the trajectory of the particle motion along the undulator in this frame, an expression for the radiation wavelength can be derived

as follows:

$$\lambda_\gamma = \frac{\lambda_u}{2\gamma^2} \left(1 + \frac{1}{2}K^2 + \gamma^2\theta^2 \right). \quad (1.1)$$

Here θ is the observation angle, γ is the Lorentz factor and K is the undulator parameter, which defines the oscillating motion of the particle in the undulator and is given by the formula

$$K = \frac{eB_0\lambda_u}{2\pi m_e c}, \quad (1.2)$$

where B_0 is the magnetic field of the undulator, c is the speed of light and e and m_e are the electron charge and mass, respectively. Equation 1.1 gives a simple relation between the fundamental wavelength of undulator radiation and the undulator parameters.

1.1.2 Low-gain FEL regime

The principle of the free electron laser is to use an electron beam as an active medium to enhance the radiation. When an electron beam passes through an undulator it emits undulator radiation. The discussion here starts with a setup that recycles this radiation in an optical cavity and overlaps it with another electron beam entering the undulator. As the radiation and the electron beam co-propagate through the undulator, an energy transfer takes place between the electrons and the transverse electric field of the radiation. This happens only due to the fact that the motion of the electrons has a transverse component in the undulator. When the phase of the electron oscillation is in a certain relation with the phase of the co-propagating radiation, the electron can continuously lose energy to the external radiation performing a stimulated radiation emission. If this condition holds during several periods, a growth in the radiation intensity will take place. However, as the electron bunch is longer than the radiation wavelength, different electrons along the bunch will experience different phases of the radiation. Furthermore, as the electrons perform oscillating motion in the undulator, they travel forward slower than the radiation. As a consequence, the radiation propagates along the electron bunch and interacts differently with different parts of the bunch. A quantitative approach is needed to understand the conditions under which an average energy transfer from the electron beam to the radiation is possible.

In the following derivations it is assumed that the amount of energy transferred from the electron beam to the radiation is small and it does not affect the motion of the electrons. The energy transfer ΔW between an electron and the electric component of the radiation can be expressed as follows:

$$\Delta W = e \int \mathbf{E}_L d\mathbf{r} = e \int \mathbf{E}_L \mathbf{v} dt. \quad (1.3)$$

Here \mathbf{E}_L is the electric field of the radiation, \mathbf{v} is the velocity of the electron and \mathbf{r} is its coordinate. As the energy transfer is possible only when the electron motion has a transverse component, we consider only the transverse velocity v_\perp of the electron in equation 1.3, which

is defined by the undulator and can be derived as

$$v_{\perp} = \beta c \frac{K}{\gamma} \sin(k_u z), \quad (1.4)$$

where βc is the velocity of the particle, K is the undulator parameter, k_u is the wavenumber defined by the undulator period and z is the longitudinal coordinate. Inserting equation 1.4 in 1.3 and writing the electric field as $E_L = E_{L0} \cos(\omega_L t - k_L z + \phi_0)$, the amount of the energy transfer can be brought to the following form:

$$\Delta W = \frac{1}{2} e \beta c \frac{K}{\gamma} E_{L0} \int (\sin \Psi^+ - \sin \Psi^-) dt. \quad (1.5)$$

In the equation Ψ^{\pm} is defined as

$$\Psi^{\pm} = \omega_L t - (k_L \pm k_u) z + \phi_0, \quad (1.6)$$

with ω_L and k_L being the radiation frequency and the wavenumber, respectively. It is clear from equation 1.5 that the energy transfer can be continuous under the condition that $\Psi^{\pm} = \text{const}$, namely

$$\frac{d\Psi^{\pm}}{dt} = \omega_L - (k_L \pm k_u) \dot{z} = 0. \quad (1.7)$$

The term \dot{z} is the longitudinal velocity of the electron in the undulator. The equations of motion of the electron in the undulator are derived in [39] and [40] and the velocity \dot{z} can be written as

$$\dot{z} = \frac{dz}{dt} = \beta c \left[1 - \frac{K^2}{2\beta^2 \gamma^2} \sin^2(k_u z) \right]. \quad (1.8)$$

Inserting this expression for the longitudinal velocity in the undulator into equation 1.7 yields the condition of the continuous energy transfer in the following form:

$$-\frac{k_L}{2\gamma^2} \left(1 + \frac{1}{2} K^2 \right) \pm k_u = 0. \quad (1.9)$$

This equation holds only for + sign and can be written also in terms of radiation wavelength:

$$\lambda_L = \frac{\lambda_u}{2\gamma^2} \left(1 + \frac{1}{2} K^2 \right). \quad (1.10)$$

This is exactly the same as equation 1.1 at observation angle $\theta = 0$. This means that the condition of the continuous energy transfer between the electrons and the radiation is satisfied for the fundamental wavelength of the undulator radiation, and the FEL process can take place for this wavelength. In a planar undulator the lasing condition holds also for odd harmonics of the fundamental wavelength: $\lambda_h = \lambda_L/h$, where h is an odd integer (the even harmonics are 0 due to the symmetric motion inside the undulator). Equation 1.10 gives an important

information about the wavelength of the FEL radiation that can be achieved for a certain type of undulator and specific energy of the electron beam.

The amount of the energy transferred to the radiation is given by the FEL gain, which is defined as

$$G = \frac{\langle \Delta W_L \rangle}{W_L}. \quad (1.11)$$

The term W_L in the equation is the energy of the laser field and $\langle \Delta W_L \rangle$ is its average growth per pass through the undulator.

In the discussed setup the radiation intensity increases only by few percents per cycle and the energy transferred from the electron beam to the radiation is too small to affect the motion of the electrons. This corresponds to so-called low-gain (small-gain) FEL regime, when only moderate values can be achieved for the FEL power.

1.1.3 SASE FEL regime (high-gain mode)

When the distance between radiating charged particles is smaller than the radiation wavelength, the emitted radiation is coherent. In this case the radiation power is proportional to the square of the number of radiating particles. The electron bunches delivered in the FEL facilities are typically much longer than the radiation wavelengths in the ultraviolet (UV) or X-ray region, and coherent radiation from all the electrons in the bunch is not possible. Instead, it is possible to obtain a substructure within the electron bunch (micro bunching) such that each micro bunch has a size of the wavelength of interest. In this case each substructure of the bunch can radiate coherently at the defined wavelength.

The micro bunching can occur in the electron beam traveling through a very long undulator. As the distribution of the electrons inside the bunch is not perfectly uniform, there are different density fluctuations along the bunch. When there is a small density fluctuation with a size of a certain wavelength, it will radiate coherently at that particular wavelength with a certain bandwidth. As the electrons perform oscillating motion, they move slower than the radiation and, therefore, there will be a slippage between the radiation and the electron beam. Only the radiation at the fundamental wavelength, moving along the electron beam, will interact constructively with the other electrons along the bunch and will grow at every period of the undulator (in accordance to equation 1.10). After some distance inside the undulator, when the radiation energy is high enough, the interaction of electron beam with this radiation will induce an energy modulation inside the beam with the same wavelength. Due to the dispersion caused by the undulator, the energy modulation will transform into a density modulation resulting in micro bunching of the electrons. These micro bunches will radiate coherently at the fundamental wavelength of the undulator.

The process of micro bunching and the FEL radiation described here is initiated by a stochastic process of density fluctuations inside the electron bunch. This regime of FEL generation is called self-amplified-spontaneous-emission (SASE). The radiation intensity in this case grows

exponentially, and the growth can be presented in the following form:

$$I_{SASE} \propto I_0 \exp\left(\frac{z}{L_G}\right). \quad (1.12)$$

Here L_G is called the power gain length and is derived in the theory of SASE FEL ([39, 40]) as

$$L_G = \frac{\lambda_u}{4\sqrt{3}\pi\rho}. \quad (1.13)$$

The term ρ in this equation is the FEL parameter. It defines the gain length of the SASE power and can be found from the theory to be

$$\rho = \left(\frac{KJJ}{4\sqrt{2}} \cdot \frac{\lambda_u\Omega_p}{2\pi c\gamma}\right)^{2/3}, \quad (1.14)$$

where Ω_p is called plasma frequency and is defined by the density of the electrons n_e in the bunch as $\Omega_p = \sqrt{4\pi c^2 r_e n_e / \gamma}$. The JJ function used in the equation 1.14 is given by Bessel functions and is dependent on the undulator parameter K :

$$JJ = J_0\left(\frac{K^2}{4+2K^2}\right) - J_1\left(\frac{K^2}{4+2K^2}\right). \quad (1.15)$$

The FEL parameter is one of the quantities that define the peak power of the FEL radiation from an electron beam when the saturation is reached:

$$P_{peak} \approx \rho I_{peak} \frac{E}{e}, \quad (1.16)$$

with I_{peak} being the peak current of the electron beam and E being the energy of the electrons. The typical power delivered with high-gain FEL regime is at the order of 10 GW.

1.2 Methods for temporal diagnostics of pulses

This section includes short descriptions of various techniques that are being utilized at different facilities for FEL pulse length and arrival time measurements.

Electro-optical method: This method is used for the arrival time measurement relative to the experimental optical laser. The basic principle is to overlap the FEL and optical pulses on a crystal and observe the FEL-induced transmission (reflectivity) change in the crystal. When the UV/X-ray FEL pulse propagates through the crystal, it increases the number of the free carriers in the medium by photoionization. This induces a change in the optical properties of the medium, namely, the optical transmission (reflectivity) of the crystal. This change can be encoded in the spectral, spatial or temporal distribution of the optical pulse. By finding the transmission edge along the optical pulse, it is possible to obtain the relative arrival time of the two pulses. This method can measure the FEL relative arrival time with an accuracy of few femtoseconds. It is non-invasive for X-ray pulses and can perform measurements for each single FEL pulse. The method, however, is not able to measure the duration of the short photon

pulses due to a long relaxation time of the crystal (in order of a picosecond). A possible way of retrieving the pulse length from this method is described in [21]. This study demonstrates that the number of the free carriers grows linearly along the XUV pulse, changing the transmission of the medium accordingly. Measuring the range of this linear change gives an information about the ionizing photon pulse duration.

Transverse deflecting cavity after the undulator: This method uses a transverse deflecting cavity (TDC) positioned behind the undulator to measure the longitudinal distribution of the electron bunch in phase-space after the radiation. The comparison of the distributions with and without the FEL radiation allows to derive the temporal profile of the FEL pulses. This method is currently being used at LCLS for temporal photon diagnostics [19]. The derivations here are mainly based on this study. The method of measuring the longitudinal profile of the electron beam by a deflecting radio-frequency (RF) cavity was first proposed by [43]. The idea is to apply a time-varying transverse deflecting electric field on the electron bunch to encode the temporal structure of the bunch in the transverse coordinate. The small angular deflection $\Delta x'$ experienced by the electron at a certain phase of the cavity is given as

$$\Delta x' = \frac{eV_0}{pc} \left(\frac{2\pi}{\lambda} ct \cos \phi + \sin \phi \right), \quad (1.17)$$

where V_0 is the peak voltage of the cavity, λ and ϕ are the RF wavelength and phase, respectively, and p is the momentum of the electron. The coordinate t in the expression gives the position of an electron with respect to the bunch center. In order to obtain the corresponding spatial distribution on the screen, one needs the element R_{12} of the transfer matrix from the deflector to the screen, where the electrons are registered. This element provides the transfer from the angular coordinate to the spatial coordinate and is given as $R_{12} = \sqrt{\beta_d \beta_s} \sin \Delta \Psi$, where β_d and β_s are the transverse beta functions at the deflector and the screen, respectively, while $\Delta \Psi$ is the horizontal phase advance between the two positions. The transverse position corresponding to $\Delta x'$ deflection can be written as

$$\Delta x = \frac{eV_0}{pc} \sqrt{\beta_d \beta_s} \cdot |\sin(\Delta \Psi)| \left(\frac{2\pi}{\lambda} ct \cos \phi + \sin \phi \right). \quad (1.18)$$

It can be seen from the equation that the highest sensitivity can be achieved at the zero-crossing ($\phi = 0$) of the deflector. It is possible to calibrate the measurements by varying the phase around the zero-crossing and measuring the position of the bunch center on the screen. With the calibration constant S the temporal duration can be obtained from the horizontal distribution on the screen:

$$\sigma_t = \frac{\sigma_x}{cS}, \quad (1.19)$$

where σ_x is the rms width of the transverse distribution. In order to obtain also the energy spectrum of the beam, a dispersion section in vertical plane is positioned before the screen. This gives a direct relation between the vertical coordinate on the screen and the energy distribution in the bunch. Therefore, the rms size σ_y of the vertical distribution on the screen

is given by the energy spread of the electron beam:

$$\sigma_y = \eta_{ys} \frac{\Delta E}{E_0}, \quad (1.20)$$

with η_{ys} being the vertical dispersion function, while ΔE and E_0 are the energy spread and the central energy of the electron bunch, respectively.

Having the described two calibrations, it is possible to obtain the image of the electron bunch in the longitudinal phase-space from the spatial image on the screen. It is possible to extract the temporal profile and the energy spectrum of the FEL pulse by comparing the two images of the electron bunch in phase-space with and without FEL radiation. This measurement method is able to provide the FEL pulse duration with only a few femtoseconds resolution. The measurements can be done with FEL pulses in range of few hundreds of femtoseconds and wavelengths in both soft and hard X-ray region. The disadvantage of the method is its cost, which grows rapidly with the energy of the electron beam.

Spectral method: This method uses the relation between the photon pulse structure in temporal and frequency domains. The simplest way to describe the method is to point out that the Fourier transform of the smallest structure in the frequency domain (energy spectrum) provides information about the part of the temporal profile that contributes to the mentioned frequencies. Therefore, by utilizing a spectrometer that can resolve separate spikes of the SASE spectrum, one can obtain information about the photon pulse duration from the energy spike widths. This method works better for short pulses (10 fs and less), given the fact that the spikes in the spectrum are wider in this case, and the requirements on the resolution of the spectrometer are less strict. SACLA photon diagnostics are currently using this technique for a single-shot FEL pulse length measurement [20]. This method is relatively cheap compared to the TDC technique. The pulse length measurement with this spectral method is, however, very sensitive to the spectral content of the FEL pulse, especially to an energy chirp along the pulse. The reason is that the spectrometer can measure with a high resolution only a small part of the whole FEL spectrum and some important information about the phase along the pulse may be missed out. The obtained information in this case is only about the part of the temporal profile that contributes to the frequency (energy) range that has been measured.

Another method to obtain the pulse duration from the spectral analysis of the FEL pulses is described in [44, 45, 46]. The idea is to find the second order spectral correlation function of the radiation:

$$g_2(\omega, \omega') = \frac{\langle I(\omega)I(\omega') \rangle}{\langle I(\omega) \rangle \langle I(\omega') \rangle}, \quad (1.21)$$

where $I(\omega)$ is the spectral intensity of the radiation. The function $g_2(\omega, \omega')$ is related to the Fourier transform of the temporal profile of radiation pulse. This method is not single-shot and an average of many measured FEL spectra is required for the calculation of the second order spectral correlation function.

1.3 Photoionization in external streaking field

The principle of the streak camera is to encode the temporal properties of the photon pulse in the energy spectrum of photoelectrons produced by this pulse. In the light-field streaking setup it is done by the time-varying electric field of a laser pulse that is present during the ionization. The basic idea of THz/IR streak camera is described in [33, 47]. More detailed theory of photoionization in presence of a streaking field and photon pulse length calculation is well discussed in [30, 48, 49]. This section briefly covers both the quantum mechanical and the semiclassical models of the theory. Most of the derivations are based on the mentioned references.

1.3.1 Quantum model

In this model, for the sake of simplicity, the Planck constant \hbar and electron mass m_e and charge e are assumed to be unity to avoid bulky mathematical expressions. We start with a strong ionizing field interacting with a single electron and assume that the effect from the other electrons present in the atom is negligible. Due to the interaction the electron moves from its ground state to a continuum state denoted as $|\mathbf{v}\rangle$ and corresponding to a momentum of \mathbf{v} . The probability amplitude of such a transition is derived using the perturbation theory and can be written as

$$a_{\mathbf{v}} = -i \int_{-\infty}^{+\infty} dt \cdot \mathbf{d}_{\mathbf{v}} \cdot \mathbf{E}_x(t) \exp[i(W + I_p)t]. \quad (1.22)$$

In this expression $\mathbf{E}_x \propto \exp[\omega_x t]$ is the ionizing field of the X-ray radiation with a central frequency of ω_x , I_p is the ionization potential of the electron, $\mathbf{d}_{\mathbf{v}}$ is the element of the dipole transition matrix from the ground I_p state to the $|\mathbf{v}\rangle$ state and $W = \mathbf{v}^2/2$ is the energy of the electron at the final state with momentum \mathbf{v} . The final energy is obtained by the ionizing field frequency and the ionization potential from $\omega_x = I_p + W$. Equation 1.22 gives a direct relation between the energy spectrum of the ionizing pulse and the wavepacket of the electron created by the pulse. The integration over time in the equation shows that the ionization can take place at any time t and its probability is proportional to the instantaneous field strength $\mathbf{E}_x(t)$ and the dipole transition matrix element. The final energy of the ionized electron is defined by the phase $I_p t$ accumulated at the ground state until the moment t of the ionization and the phase accumulated in the free motion. It is assumed in this derivations that the field of the ion created after the ejection of the electron does not affect the dynamics of the electron.

When the ionization takes place in presence of a low-frequency streaking light pulse, an interaction between the electron and the laser field occurs. The energy of the electron after the ionization, therefore, starts changing in time due to the interaction and at a certain point in time it is written as:

$$W_L(t) = \frac{\mathbf{v}_L^2(t)}{2}, \quad (1.23)$$

1.3. Photoionization in external streaking field

where $\mathbf{v}_L(t)$ is the momentum of the electron in the laser field at time t of the interaction and is given as the vector sum of the momentum without the laser field and the vector potential of the laser at the moment t : $\mathbf{v}_L(t) = \mathbf{v} + \mathbf{A}_L(t)$. Inserting this expression into 1.23 we obtain

$$W_L(t) = W + \left(\mathbf{v}\mathbf{A}_L(t) + \frac{\mathbf{A}_L^2(t)}{2} \right), \quad (1.24)$$

where the term in the brackets is the contribution from the external laser field. The expression 1.24 needs to be inserted in equation 1.22 to apply a correction to the transition amplitude $a_{\mathbf{v}}$ of the electron to its final state. After both the ionizing X-ray field and the streaking laser field have disappeared the term $a_{\mathbf{v}}$ has the following form for a τ delay between the two fields:

$$a_{\mathbf{v}_L}(\tau) = -i \int_{-\infty}^{+\infty} dt \cdot \exp[i\phi(t)] \cdot \mathbf{d}_{\mathbf{v}_L(t)} \cdot \mathbf{E}_x(t - \tau) \exp[i(W + I_p)t], \quad (1.25)$$

where the newly introduced term $\phi(t)$ is the phase accumulated during the interaction of the electron with the laser field and it is written as

$$\phi(t) = - \int_t^{+\infty} \left(\mathbf{v}\mathbf{A}_L(t') + \frac{\mathbf{A}_L^2(t')}{2} \right) dt'. \quad (1.26)$$

The integration here is performed starting from the time of ionization t , when the free electron starts interacting with the streaking field. During this interaction the energy of the electron changes depending on the observation time t' until the streaking field vanishes. Equations 1.25 and 1.26 show the temporal phase modulation induced by the laser field on the electron wavepacket injected in continuum by the X-ray field. Assuming a linearly polarized electric field: $\mathbf{A}_L(t) = -\frac{\mathbf{E}_L(t)}{\omega_L} \sin \omega_L t$ with a slowly varying envelope $\mathbf{E}_L \approx \text{const}$, the term $\phi(t)$ can be written in a different form, to better understand the effect of the laser field:

$$\phi(t) = - \int_t^{+\infty} \left(\frac{E_L^2(t')}{2\omega_L^2} \sin^2(\omega_L t') - \frac{vE_L(t')}{\omega_L} \sin(\omega_L t') \cos \theta \right) dt' \approx \phi_1(t) + \phi_2(t) + \phi_3(t), \quad (1.27)$$

where θ is the angle between the laser field and the electron momentum before the streaking and the three components are

$$\begin{aligned} \phi_1(t) &= - \int_t^{+\infty} U_p(t') dt', \\ \phi_2(t) &= \frac{\sqrt{8WU_p(t)}}{\omega_L} \cos \theta \cdot \cos(\omega_L t), \\ \phi_3(t) &= - \frac{U_p(t)}{2\omega_L} \sin(2\omega_L t). \end{aligned} \quad (1.28)$$

Here $U_p(t) = E_L^2(t)/4\omega_L^2$ is the ponderomotive potential of the field. It changes slowly in time with the change of the envelope of the laser field. The terms $\phi_2(t)$ and $\phi_3(t)$, on the other hand, vary fast with the frequency of the laser field and its second harmonic, respectively. In most of the practical cases the energy of the ionized electron W is much bigger than the

Chapter 1. Theory

ponderomotive potential U_p . For this reason the main contribution to the phase $\phi(t)$ comes from $\phi_2(t)$, which depends on the observation angle and on the phase of the streaking field $\omega_L t$. The term $\phi_2(t)$ defines the temporal modulation of the phase of the electron wavepacket in a continuum state with momentum \mathbf{v} in 1.25.

We now assume that the ionizing X-ray field given in 1.25 is Gaussian with a linear chirp. It can be written as

$$\mathbf{E}_x(t) = \mathbf{E}_{0x} \cdot \exp[-a(t - t_0)^2] \cdot \exp[i(\omega_x(t - t_0) + c(t - t_0)^2)], \quad (1.29)$$

where \mathbf{E}_{0x} is the field amplitude, c is the linear chirp along the X-ray pulse and a is defined by the rms duration τ_x of the pulse: $a = 1/(2\tau_x^2)$. The spectral intensity of the ionizing pulse $I_x = |E_x(\omega)|^2$ can be obtained from the Fourier transformation of 1.29. The calculations show the following relation:

$$I_x(\omega) \propto \exp\left[-\frac{a(\omega - \omega_x)^2}{2(a^2 + c^2)}\right]. \quad (1.30)$$

Such a result shows that the rms spectral width of the X-ray pulse is $\sigma_x = \sqrt{\frac{a^2 + c^2}{a}}$.

The spectrum of the photoelectrons is given as the square of the transition amplitude from the bound state to a continuum state with momentum \mathbf{v}_L in presence of streaking laser field: $S(\omega) = |a_{\mathbf{v}_L}|^2$. Taking into account 1.25, 1.28 and 1.29, the photoelectron spectrum is written as

$$S(\omega) = \left| - \int_{-\infty}^{+\infty} dt \cdot \exp[i\phi_2(t)] \cdot \mathbf{d}_{\mathbf{v}_L(t)} \cdot \mathbf{E}_{0x} \exp[-a(t - t_0)^2] \times \right. \\ \left. \times \exp[i(\omega_x(t - t_0) + c(t - t_0)^2)] \exp[i(W + I_p)t] \right|^2. \quad (1.31)$$

In order to compute this integral, some assumptions are made. The probability for the ionization to take place is taken to be unity: $\mathbf{d}_{\mathbf{v}_L} = 1$. As mentioned before, the energy of the ionized electrons without the streaking field is assumed much bigger than the ponderomotive potential $W \gg U_p$, which allows to replace $\phi(t)$ by $\phi_2(t)$. It is also considered that the duration of the X-ray pulse is much shorter than the period of the laser field. This assumption is true for most of the practical cases of interest and allows to rewrite $\phi_2(t)$ in the following form:

$$\phi_2(t) \approx \frac{\sqrt{8WU_p}}{\omega_L} \cos\theta \cdot \left(1 - \frac{\omega_L^2 t^2}{2}\right). \quad (1.32)$$

After calculating the integral 1.31 numerically, the spectrum of the electrons propagating parallel to the streaking field ($\cos\theta = \pm 1$) obtains the following form:

$$S(\omega) \propto \exp\left[\frac{-a(\omega - \omega_0)^2}{2(a^2 + (c \pm s/2)^2)}\right], \quad (1.33)$$

where term s is the streaking strength (speed) that shows the change of the electron energy per unit time due to the streaking field: $s = (\partial\delta W)/\partial t$. Equation 1.33 shows that the rms width

of the spectral envelope of the streaked electrons is

$$\sigma_{st} = \sqrt{\frac{a^2 + (c \pm s/2)^2}{a}}. \quad (1.34)$$

The sign \pm here corresponds to the electrons propagating in the direction of the streaking field and opposite to it. Equation 1.34 can be rewritten in terms of temporal duration of the X-ray pulse τ_x and it's spectral width σ_x :

$$\sigma_{st}^2 = \sigma_x^2 + \tau_x^2 (s^2 \pm 4cs). \quad (1.35)$$

This expression shows that the spectral width changes in presence of a streaking field due to the duration of the ionizing pulse and a linear energy chirp along it. Equation 1.35 gives an important relation between the duration of the X-ray pulse and the spectrum of the photoelectrons, which is used in the temporal diagnostics of short photon pulses. Assuming that in absence of the streaking laser field the spectrum of the photoelectrons mimics the spectrum of the X-ray pulse $\sigma_0 = \sigma_x$, the rms length of the X-ray pulse can be written as

$$\tau_x = \sqrt{\frac{\sigma_{st}^2 - \sigma_0^2}{s^2 \pm 4cs}}. \quad (1.36)$$

The same result can be obtained with the semiclassical approach.

1.3.2 Semiclassical model

When an electron is ionized in an external laser field, the frequency of the ionizing field is much higher than the frequency of the streaking field, and the processes of the ionization and the streaking take place in different time scales. The semiclassical model first discusses the ionization process and then the interaction of the ionized electron with the external laser field. The initial kinetic energy of the electron after the ionization and before the interaction with the laser field is given as $W_0 = m_e v_0^2 / 2 = \hbar\omega_x - I_p$, where v_0 is the velocity of the electron and $\hbar\omega_x$ is the energy of the X-ray field. For the discussed process $I_p \gg \hbar\omega_L$, meaning that the field of the streaking laser is too weak to affect the bounded state of the electron inside the atom and $\hbar\omega_x \gg I_p$, meaning that the effect of the ionic field on the ejected electron is negligible. For such conditions the velocity of the electron in time is written as

$$\mathbf{v}(t) = -\frac{e\mathbf{A}(t)}{m_e} + \left[\mathbf{v}_0 + \frac{e\mathbf{A}(t_i)}{m_e} \right]. \quad (1.37)$$

Here it is taken into account that at the moment of the ionization $t = t_i$ the initial velocity is $\mathbf{v}(t_i) = \mathbf{v}_0$. The first term of the right-hand-side of equation 1.37 corresponds to the oscillation of the electron velocity caused by the oscillating vector potential $\mathbf{A}(t)$ of the laser field. These oscillations are around the constant value given by the second part in the right side of 1.37, and they vanish once the laser pulse has passed: $\mathbf{A}(t) = 0$. This means that the final

Chapter 1. Theory

velocity of the electron stays constant after the laser field has vanished and it depends on the laser field at the moment of ionization t_i :

$$\mathbf{v}_f = \mathbf{v}_0 + \frac{e\mathbf{A}(t_i)}{m_e}. \quad (1.38)$$

Assuming a linearly polarized laser field, the vector potential can be written as $\mathbf{A}(t_i) = -\frac{E_{0L}}{\omega_L} \sin \varphi_i$, where φ_i is the phase of the electric field at the moment of ionization t_i . Taking this into account and using 1.38 for the final kinetic energy $W_f = m_e v_f^2/2$ of the electron, it is possible to derive the following expression ([30, 48]):

$$W_f = W_0 + 2U_p \cos(2\theta) \sin^2 \varphi_i \pm \sqrt{1 - \frac{2U_p}{W_0} \sin^2 \theta \cdot \sin^2 \varphi_i} \cdot \sqrt{8W_0 U_p} \cdot \cos \theta \cdot \sin \varphi_i. \quad (1.39)$$

This equation shows that the final kinetic energy of the photoelectron after interacting with the streaking laser depends on the phase of the laser field φ_i at the ionization time and the angle θ between the initial velocity of the electron and the electric field of the laser. Here $U_p = e^2 E_{0L}^2 / (4m_e \omega_L^2)$ is the ponderomotive potential of the electron in the laser field as defined previously in 1.28. As in the case of the quantum model, we can assume that in most of the practical cases $W_0 \gg U_p$. When this condition holds the final kinetic energy of the electrons traveling parallel to the streaking field ($\theta = 0$) has a simpler form:

$$W_f = W_0 \pm \sqrt{8W_0 U_p} \cdot \sin \varphi_i. \quad (1.40)$$

In order to compare this result to the quantum model, we recall equations 1.24 and 1.26, which give the relation $\Delta W = -\partial\phi(t)/\partial t$. Taking into account equation 1.28 for $\phi_2(t)$, we find that the energy change of the photoelectrons provided by the quantum model is equivalent to that of semiclassical model given by 1.40. In other words, semiclassical model shows that the final kinetic energy of the electron is defined by the time t_i it was ionized with respect to the phase of the laser field and the quantum model shows that the phase accumulated during this process is temporally modulated by the external laser field. The comparison of the two models is well presented in [30] and [48].

1.3.3 Photon pulse length calculation

When the ionization is done by a photon pulse with a certain temporal duration, the electrons ionized by different parts of the pulse will be created at different points in time. Each of these electrons will have a certain ionization time t_i and, therefore, will experience different phase φ_i of the streaking laser field. The final energy spectrum of the electrons in this case contains information about the temporal structure of the ionizing X-ray pulse. Moreover, it is the convolution of the energy spectrum without the external streaking field and the temporal profile of the X-ray pulse. In case of convolution the rms widths of the profiles should be

1.3. Photoionization in external streaking field

added in quadrature. Taking into account also the contribution from the linear energy chirp along the photon pulse, the rms spectral width of the streaked electrons has the form 1.35:

$$\sigma_{st}^2 = \sigma_0^2 + \tau_x^2 (s^2 \pm 4cs). \quad (1.41)$$

We note here that the contribution from the linear chirp depends on the direction of photoelectron velocity with respect to the streaking field: it may broaden or narrow the spectral width of the electrons as shown by the sign \pm in equation 1.41. On the other hand, as the spectral width σ_0 contains the effect of chirp implicitly (see equation 1.30), the right-hand-side of 1.41 always stays positive even for large value of chirp for "minus" sign.

An illustration of the streaking process is graphically shown in figure 1.1. The X-ray pulse creates an ensemble of photoelectrons which are streaked by the laser field. The opposite signs of the streaking field correspond to electrons traveling along the field direction or opposite to it. For the electrons with blue spectrum in the figure, the streaking strength s and the chirp c

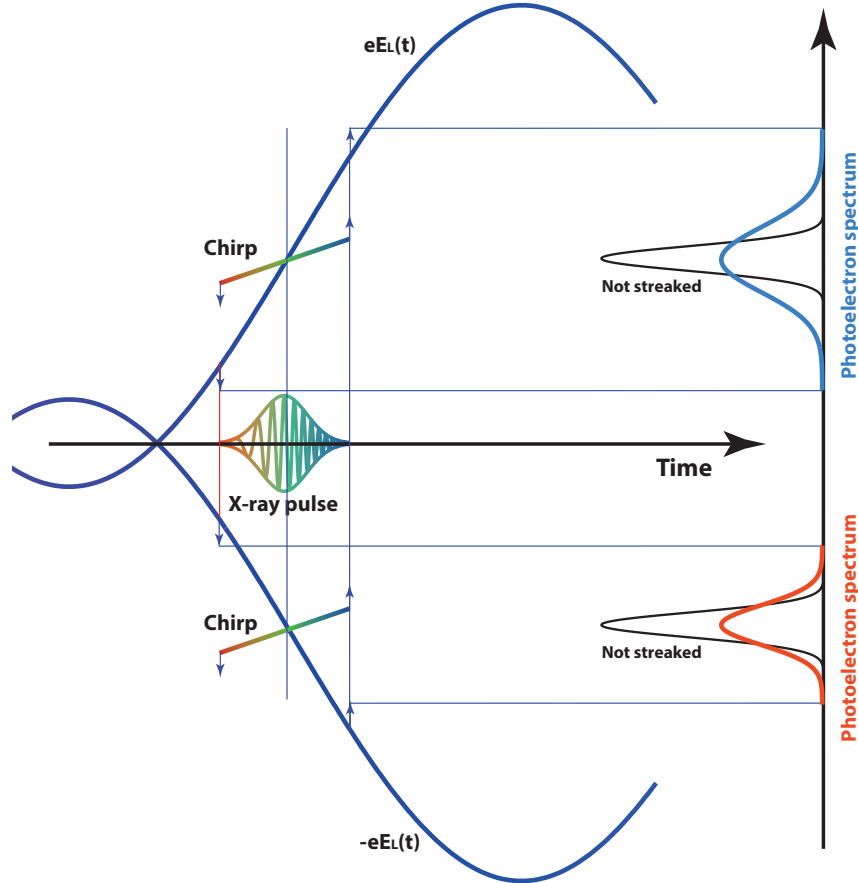


Figure 1.1: Demonstration of the streaking process. The photoelectron spectra become broader because of the streaking by the laser field.

have the same sign, which corresponds to the "plus" sign in 1.41. In this case the contribution of the chirp is an extra broadening of the spectrum. When the chirp and the streaking strength

have opposite signs (photoelectron spectrum given in red in the figure), the effect from the chirp makes the spectrum narrower corresponding to the "minus" sign. In order to eliminate the effect from the chirp, both spectra should be measured simultaneously (both blue and red in the figure). Having the quadratic difference of the widths of streaked and non-streaked spectra $\Delta\sigma_{\pm}^2 = \sigma_{st}^2 - \sigma_0^2 = \tau_x^2(s^2 \pm 4cs)$ for these two cases, the pulse length can be calculated:

$$\tau_x = \sqrt{\frac{\Delta\sigma_+^2 + \Delta\sigma_-^2}{2s^2}}. \quad (1.42)$$

This expressions is most commonly used in the experiments for the pulse length calculation. For normal operation mode of FEL facilities the linear energy chirp along the X-ray pulse is small compared to the streaking effect. The domination of the streaking effect causes overall broadening of the photoelectron spectra in both cases as shown in figure 1.1.

One can also see from the figure that a shift in the arrival time of the X-ray pulse will cause a shift of the spectrum in energy. This means that by measuring the central energy of the photoelectron spectrum, it is possible to obtain the arrival time of the FEL pulse relative to the streaking laser pulse.

It is clear from the figure that only the pulses arriving at the linear part of the streaking field can be measured with a high resolution. In case when the arrival times of the FEL pulses jitter from shot to shot, low-frequency streaking fields (with long linear part) should be used to be able to measure all the X-ray pulses. This requires the streaking laser field to be in the Terahertz (THz) region.

1.4 THz generation

The arrival time of the X-ray pulses delivered by FEL facilities may jitter from pulse to pulse by 100 fs rms or more. In order to measure these pulses by light-streaking method, the linear part of the streaking field has to be hundreds of femtoseconds long. This means that the frequency of the laser field should be in range of 0.2 THz-5 THz. On the other hand, the strength of the streaking field (given by the term s in 1.42) directly affects the resolution of the measurements and a high radiation power of the THz is needed. The generation of THz radiation in the mentioned frequency range is, however, challenging and only moderate power is achievable. Various methods of THz generation developed in the recent years are discussed in [50]. One of the methods most commonly used in the THz streak cameras is the optical rectification in a non-linear crystal discussed in [51] and [52]. It is shown that when an intense electromagnetic radiation propagates through a medium with no central symmetry, a second-order polarization with zero frequency is created in this medium. This electric field follows the phase envelope of the radiation pulse as a beating that propagates with the pulse. When the duration of the radiation envelope is in a picosecond range, the polarization beating has a frequency in a Terahertz range, which is traveling in the medium and is emitted as THz radiation.

As in other second-order nonlinear effects, in the optical rectification the phase matching

condition mentioned in [52, 53, 54], needs to be satisfied :

$$\Delta k = k(\omega_{opt} + \omega_{THz}) - k(\omega_{opt}) - k(\omega_{THz}) = 0, \quad (1.43)$$

where k is the wave vector with ω_{opt} and ω_{THz} being the frequencies of the optical and the THz radiations, respectively, and $\omega_{opt} + \omega_{THz}$ is within the bandwidth of the optical pulse. Solving 1.43 for $k(\omega_{THz})$ and dividing the equation by ω_{THz} results in

$$\frac{k(\omega_{THz})}{\omega_{THz}} = \frac{k(\omega_{opt} + \omega_{THz}) - k(\omega_{opt})}{\omega_{THz}} \approx \left(\frac{\partial k}{\partial \omega} \right)_{opt}. \quad (1.44)$$

The last part of this equation is written based on the fact that $\omega_{THz} \ll \omega_{opt}$. Equation 1.44 shows that the phase matching is possible when the phase of the THz pulse travels with the same velocity as the envelope of the optical pulse. This condition can be rewritten as

$$v_{THz}^{ph} = v_{opt}^{gr}, \quad (1.45)$$

meaning that the phase velocity of the THz wave should be equal to the group velocity of the optical wave. The refractive index of the medium is usually different for the optical wave and the THz, which makes the group velocity of the optical pulse bigger than the phase velocity of the THz pulse. In order to achieve the velocity matching, it has been proposed to use an optical laser with a tilted pulse front [55]. The idea is to tilt the optical pulse front with respect to its phase front, which is perpendicular to the propagation direction. As it is shown in figure 1.2, the direction of the THz wave in this case is perpendicular to the tilted pulse front and it propagates with an angle with respect to the direction of the optical wave. As now the two

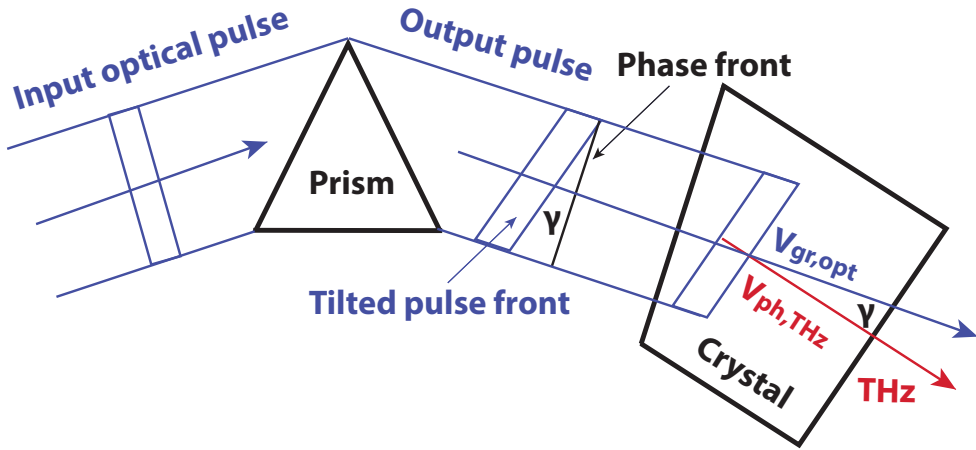


Figure 1.2: Schematic view of the velocity matching using the tilted pulse front method.

velocities in 1.45 have an angle of the tilt γ with respect to each other, the velocity matching condition can be written as

$$v_{THz}^{ph} = v_{opt}^{gr} \cos \gamma. \quad (1.46)$$

Chapter 1. Theory

This method allows to achieve the matching condition even in crystals with a big difference between the refractive indices for optical and THz waves. A tilted front can be achieved using a prism or a diffractive grating, which change the propagation direction of different frequency components in the optical pulse. This causes a continuously changing delay of the pulse front in the transverse plane resulting in a tilt of the pulse front (figure 1.2). This process is discussed in [56] where an expression for the tilt angle is derived:

$$\tan \gamma = \frac{n}{n_g} \bar{\lambda} \frac{d\epsilon}{d\lambda}. \quad (1.47)$$

Here $d\epsilon/d\lambda$ is the angular dispersion of the optical pulse bandwidth providing different angular distributions for different wavelengths, $\bar{\lambda}$ is the mean wavelength, while n and n_g are, respectively, the refractive index and the group refractive index of the medium. Using equation 1.47, it is possible to adjust the tilt angle γ for achieving the velocity matching condition 1.46.

The method with the tilted pulse front is used for the materials like LiNbO₃ and LiTaO₃ that have large difference between the refractive indices for the THz and optical waves.

The efficiency of the THz generation is defined as the ratio between the fluence of the generated THz radiation and that of the incident optical laser:

$$\eta_{THz} = \frac{F_{THz}}{F_{opt}}. \quad (1.48)$$

THz generation with lithium niobate crystal (LiNbO₃) is particularly efficient for the frequencies below 1 THz, even in room temperature. For higher frequencies the absorption in the crystal increases rapidly resulting in a decrease of the generation efficiency. A detailed analysis of the THz generation efficiency with LiNbO₃ crystal is covered by [57] and [58]. It is found that the generation efficiency increases with the power of the pumping laser up to a certain point, after which the efficiency starts decaying. This is caused by the fact that higher power of optical laser not only increases the power of the generated THz but also creates more free carriers in the crystal, which results in more absorption of the THz radiation. When the pumping laser power is higher than a certain value, the second process becomes dominant and the efficiency decreases. It is possible to obtain higher efficiency by cooling the crystal as the absorption of the THz is lower at low temperature. By optimizing different parameters of the THz generation setup, such as the wavelength and the duration of the optical laser, the temperature and the geometry of the crystal, it is possible to achieve a high generation efficiency. Different experiment of THz generation with optical rectification by a tilted front laser pulse using lithium niobate crystal report pump to THz conversion efficiency of up to 0.35% [59, 60, 61, 62, 63].

The THz generation for frequencies from 1 THz up to 10 THz is more efficient for organic crystals such as DAST or OH1 [64, 65]. To cover the frequency range from 10 THz to about 60 THz, a non-linear crystal GaSe is preferable [66]. The THz generation efficiencies and the frequency tunability for different crystals are presented in [67].

1.5 High harmonic generation

The first measurements [47, 68] performed for this thesis were carried out at a high harmonic generation (HHG) source. In order to better understand the properties of the HHG pulses used in the measurements, a brief overview of the high harmonic generation theory is provided in this section.

When a gas target is exposed to intense optical laser radiation, higher harmonics of the laser frequency are emitted by the gas. This phenomenon is called high harmonic generation and it was first experimentally observed by [69] and [70]. The simplest way to explain the process of HHG is to discuss three consecutive processes (the so-called 3 step model): 1) tunneling ionization of an electron caused by the intense laser field, 2) propagation of the free electron in the laser field, 3) recombination of the electron with the gas ion. When the electron is accelerated by the laser field during the free propagation and if its trajectory is such that it returns to its parent atom after a certain time, it emits a radiation of shorter wavelength compared to the pumping optical laser. The semiclassical approach to the problem [71] uses the quantum-mechanical theory of the tunnel ionization [72] and then treats the propagation of the free electron classically. The model assumes that the electron is ionized with a zero initial velocity before interacting with the laser field.

The probability of the tunnel ionization during the time period dt is written from the theory as

$$P(t) = R_{bc}(E_L(t))dt, \quad (1.49)$$

where R_{bc} is the rate of ionization or tunnel transition from bound (b) state to continuum (c). The term $E_L(t)$ is the laser field given as $\mathbf{E}_L(t) = \mathbf{E}_0 \cos \omega_L t$. The equation of motion of a single electron moving in this field can be solved classically. The derivations in [71] use a coordinate system connected with the atom and with XY plane being perpendicular to the direction of the optical laser propagation. Using initial conditions $x(t=0) = y(t=0) = 0$ and $v_x(t=0) = v_y(t=0) = 0$ for this coordinate system, the solution can be written as

$$\begin{aligned} x(t) &= \frac{eE_0}{m_e\omega_L^2} [1 - \cos(\omega_L t)], \\ y(t) &= a \frac{eE_0}{m_e\omega_L^2} [\omega_L t - \sin(\omega_L t)], \\ v_x(t) &= \frac{eE_0}{m_e\omega_L} \sin(\omega_L t), \\ v_y(t) &= a \frac{eE_0}{m_e\omega_L} [1 - \cos(\omega_L t)]. \end{aligned} \quad (1.50)$$

Here a represents the polarization of the laser field; it is 0 for the linear and ± 1 for the circular polarization. Equations 1.50 are very useful for understanding the process qualitatively. It shows that during the first period of the laser after the ionization, the x coordinate will go back to its initial 0 value, while the same is not possible for the y coordinate. Such a result means that the electron can return to its parent atom and the HHG process can take place

Chapter 1. Theory

only when the laser is linearly polarized, i.e. $a = 0$. When $a \neq 1$ the electron will go around after a cycle of the laser pulse but it will miss the atom due to the change of the y coordinate. As the electron recombination and the consecutive photomission takes place at every cycle of the optical laser, in the frequency domain the radiation consists of higher harmonics of the optical laser frequency. In monoatomic gases only odd harmonics are produced as the even harmonics vanish due to the central symmetry of the atomic potential.

The classical treatment of the high harmonic generation process allows to calculate the recombination probability distribution for different final kinetic energies of the electron. The calculations yield the maximum kinetic energy that the electron may acquire before the recombination, to be $3.17U_p$. Here, $U_p = e^2 E_{0L}^2 / (4m_e \omega_L^2)$ is the ponderomotive potential of the laser field defined earlier in this chapter (1.28 and 1.39). The maximum energy of the emitted photon, therefore, can be written as

$$\hbar\omega_{max} = I_p + 3.17U_p = N_{max}\hbar\omega_L, \quad (1.51)$$

where I_p is the binding energy of the recombined electron in the atom and N_{max} is, consequently, the highest possible harmonic number.

The generation of high harmonics is also modeled quantum-mechanically, which takes into account some phenomena that were neglected in the semiclassical model [73, 74, 75, 76]. For an electron being ionized in a laser field, the Schrödinger equation (in atomic units) is written as

$$i \frac{d}{dt} |\Psi(\mathbf{x}, t)\rangle = \left[-\frac{1}{2} \nabla^2 + \mathbf{V}(\mathbf{x}) - \mathbf{E}(t) \cdot \mathbf{x} \right] |\Psi(\mathbf{x}, t)\rangle, \quad (1.52)$$

where Ψ is the wave function of the electron, ∇ is the spatial derivative operator and $\mathbf{E}(t)$ is the laser field which is assumed linearly polarized: $E_x(t) = E_0 \cos \omega_L t$. For high intensities of the optical laser the potential $\mathbf{V}(\mathbf{x})$ of the parent atom mentioned in 1.52 is small compared to the kinetic energy of the electron when it is close to the atom. When the electron is close to the turning point, its kinetic energy is small but it is far from the atom and at this distance the potential of the atom is also negligible. Therefore, it can be assumed that the free electron is not influenced by the potential of the parent atom and it moves only in the field of the laser. Assuming also that the ground state $|0\rangle$ is not depleted, the wave function can be expressed by the bound state and the continuum state in the following form

$$|\Psi(t)\rangle = \exp[iI_p t] \left(a(t)|0\rangle + \int d^3\mathbf{v} b(\mathbf{v}, t)|\mathbf{v}\rangle \right), \quad (1.53)$$

where $a(t)$ and $b(\mathbf{v}, t)$ are the amplitudes of the bound state and the continuum state, respectively (with $a(t) \approx 1$). Using this wave function, it is possible to write the x component of the dipole momentum $x(t) = \langle \Psi(t) | x | \Psi(t) \rangle$ at any point in time in the following form:

$$x(t) = i \int_{-\infty}^t dt \int d^3\mathbf{p} \underbrace{\mathbf{E}(t-\tau) \cdot d(\mathbf{p} - \mathbf{A}(t-\tau))}_{\text{Ionization}} \cdot \underbrace{\exp[-iS(\mathbf{p}, t, \tau)]}_{\text{Free motion}} \cdot \underbrace{d^*(\mathbf{p} - \mathbf{A}(t))}_{\text{Recombination}}. \quad (1.54)$$

This expression helps to describe the process phenomenologically. The first part of 1.54 is the probability amplitude of the tunneling transition from the bound state to continuum caused by the field \mathbf{E} at the time $t - \tau$, d is the transition matrix element, and $\mathbf{p} = \mathbf{v} + \mathbf{A}$ is the canonical momentum at the continuum state. The second term corresponds to the free motion of the electron from the moment of ionization $t - \tau$ to the moment of recombination t , where it accumulates phase equal to $\exp[-iS(\mathbf{p}, t, \tau)]$ due to the interaction with the laser field, with S given as

$$S(\mathbf{p}, t, \tau) = \tau I_p + \int_{t-\tau}^t dt' \frac{(\mathbf{p} - \mathbf{A}(t'))^2}{2}. \quad (1.55)$$

It is worth noting here that $S(\mathbf{p}, t, \tau)$ does not depend on the potential of the ion and only the interaction with the laser field is taken into account. Finally, the third term of 1.54 is the probability amplitude of recombination, i.e. transition from the continuum state to the bound state.

The three components in equation 1.54 provided by the quantum-mechanical model correspond to the same three consecutive steps introduced in the semiclassical model. Furthermore, the quantum-mechanical model yields an expression for the highest possible photon energy similar to 1.51, showing a good agreement between the two models.

2 Simulation of the streaking process

To better understand the measurement process from the THz streak camera method, to improve the data analysis procedure used in the measurements, and to validate the theory used in THz streak cameras for photon pulse length retrieval, a Matlab code was developed to simulate the streaking effect and the pulse length calculation procedure. The code is provided in the appendix A. After obtaining the pulse lengths from the simulation, the accuracy and the precision of the measurement technique was estimated for various pulse lengths. Here the definition of accuracy is used as the absolute difference between the expected length of the photon pulse and the pulse length calculated by the simulation, whereas the precision is used as the standard deviation of the calculated values obtained by a set of simulations for the same pulse length. This chapter is based on [77] but it uses different figures and tables (corresponding to different runs). It describes the model of the simulation, explains the procedure and discusses some results characterizing the THz streaking method.

2.1 Simulation model

The main goal of this simulation is to reproduce the THz streaking effect and to obtain energy spectra of the photoelectrons for the experimental setup used for pulse length (arrival time) measurements [47, 68, 78]. The spectra delivered by the simulations allow the validation of the analysis procedure used in a THz streak camera and the estimation of the accuracy and the precision of the method. The simulation models the photoionization process and the energy streaking of the electrons in a simple way, concentrating only on the phenomena that are relevant for the photon pulse length measurement application.

As the average duration of the photoionization process is comparable with the coherence time of the FEL (of the order of 100 attoseconds for the pulses discussed here), the energy spectrum of the photoelectrons does not simply mirror the spectrum of the photon pulse; it also has a contribution from the ionization emission spectrum. The latter refers to a Gaussian energy spectrum, which is the Fourier transformation of the Gaussian profile of the mean ionization time of the photoelectrons [79]. Depending on this time, any of the two components can be dominant in the final spectrum of the electrons. When the mean ionization time is faster

Chapter 2. Simulation of the streaking process

than the coherence time of the photon pulse, the spectrum of the photoelectrons is broader than the original spectrum of the photons and it is dominated by the ionization emission spectrum. Most of the studies about the mean ionization time carried out so far [80, 81, 82, 83] refer to the outer shell electrons using photon energies of a few hundred electronvolts, and report values from a few tens up to hundreds of attoseconds (as). A recent study of mean emission time of the inner shell electrons with photon energies of up to 10000 eV, has obtained delays of about 10 as [84]. For such values of the time the photoelectrons' spectrum should be dominated by the photoionization emission spectrum. In case of 10 as emission time the corresponding energy spectrum is very broad and requires many sampling points in the simulation, which makes the procedure slow. For this reason, the simulation model takes the ionization mean time from the inner shells to be about 50 as, which still keeps the emission the dominant component of the observed spectra and does not make the simulation process too bulky as it would be for the value of 10 as. Choosing the mean emission time 50 as instead of 10 as changes only the width of the energy spectrum of the photoelectrons. This change does not affect the final result for the photon pulse length as during the simulation procedure the energy spectrum is first convoluted to the temporal profile of the photon pulse during the streaking and then deconvoluted back during the pulse length calculation process. Figure 2.1 shows the spectra of two photon pulses with different lengths and the spectrum corresponding to 50 as ionization time, as well as the temporal profiles of the pulses. One can

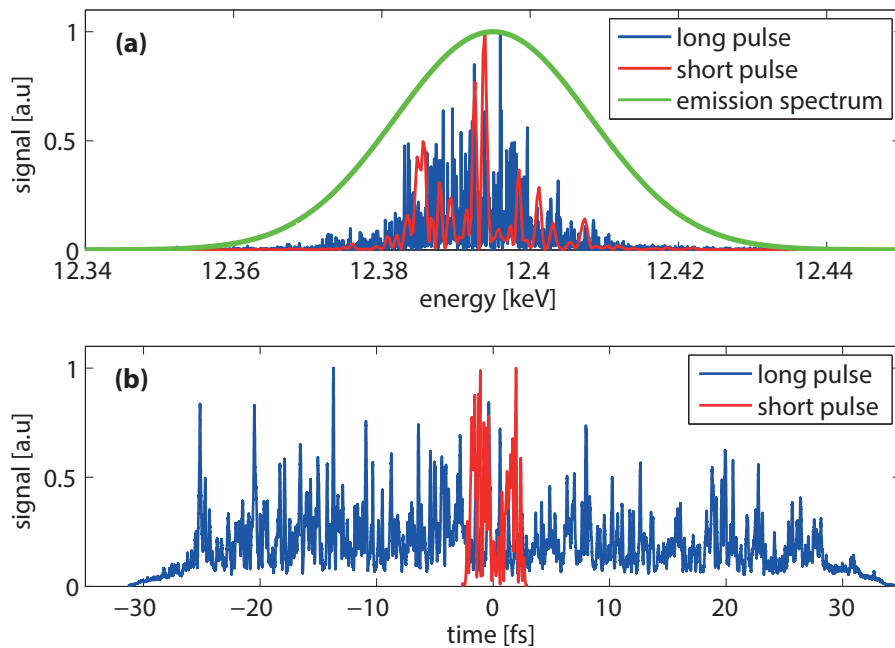


Figure 2.1: Energy spectra (a) and temporal profiles (b) of two photon pulses for SwissFEL long-pulse (blue) and short-pulse (red) operation modes and the Gaussian spectrum corresponding to a 50 as mean ionization time (green).

see from the subfigure (a) that the emission spectrum is broader than the spectra of the pulses.

The spectrum corresponding to 50 as ionization time is dominant for all the pulses used in the simulation and therefore, the energy spectra of the non-streaked photoelectrons are always considered to be the same Gaussian.

This simulation utilizes a THz pulse with a frequency of 0.5 THz and peak electric field strength of 6 MV/m corresponding to the THz pulse generated during the experimental setup described in [78]. For this setup the uncertainty in the pulse length measurement is mainly caused by the limited number of the detected photoelectrons and the energy resolution of the electron time-of-flight spectrometers (eTOFs) used in the measurements (about 1.2 eV). In the mentioned experiment the arrival time jitter of the photon pulses with respect to the THz pulse was about 100 fs rms, while the linear part of the THz pulse was more than 600 fs long. This means that the streaking strength (term s in the equation 1.42) could be considered equivalent for all the photon pulses, even for those arriving away from the zero-crossing of the THz. For this reason, the jitter of the arrival time of the photon pulses relative to the THz pulse is not considered in this simulation and all the pulses are assumed to arrive at the zero-crossing of the THz pulse. Based on the same measurements, the electric field jitter of the THz pulse is also neglected and the field strengths is assumed constant in the simulations.

The central energies of the photoelectrons without the streaking field are taken as half of the photon energies. This corresponds to 6200 eV and 620 eV of initial central energies of the electrons for hard (12400 eV) and soft (1240 eV) X-rays, respectively. The chosen values for binding energies used in the simulation are realistic and are comparable with the relevant binding energies of the noble gases used in the streaking experiments.

This simulation model assumes that the number of the photoelectrons registered by the eTOFs is in range from few thousands up to 10^5 , depending on the length of the photon pulse. These numbers were chosen based on the measurements performed earlier. A study carried out by [85] discusses the space-charge effect in the photoelectron spectra created by FEL pulses. For about 10^8 photoelectrons with energies of 15-68 eV the contribution of the space-charge effect in the electron energy spectra is only about 1 eV. For the case discussed here the maximum number of electrons registered by the eTOFs is 10^5 , corresponding to about 10^8 electrons created by the photon pulse at the interaction region. This amount of the electrons is the same as for [85], while the kinetic energies are much higher (620 eV or 6200 eV), making the space-charge effect significantly smaller than 1 eV. As the resolution of the eTOF detectors is about 1.2 eV, the space-charge effect can be neglected in the simulation.

2.2 Simulation procedure

The simulation procedure operates as follows: it takes as an input FEL pulses generated externally by the code Genesis [86], and simulates the energy streaking of the photoelectrons produced by these pulses. The code then calculates the photon pulse lengths following the procedure used in a THz streak camera. The simulation procedure is described in detail below.

2.2.1 Simulation of the FEL pulses

The FEL process was simulated with the code Genesis [86]. The electron beam properties and the lattice parameters have been chosen based on the SwissFEL specifications [10]. Overall, 178 photon pulses were produced with rms durations varying between about 1 fs and 15 fs for the radiation wavelength of 0.1 nm (photon energy of 12400 eV) and between 20 fs and 40 fs for 1 nm wavelengths (photon energy of 1240 eV). Some of the simulations were done with the standard SASE [87, 88] configuration, while some others include the option of self-seeding [89, 90, 91, 92] to reduce the bandwidth of the FEL pulse. Figure 2.1 shows the time profiles and the spectra of two of the simulated FEL pulses for 0.1 nm wavelength. The blue and red curves in the figure show the long-pulse and the short-pulse configurations of SwissFEL, respectively.

2.2.2 Simulation of the ionization and streaking

The simulation procedure commences once a photon pulse is generated with defined temporal profile and energy spectrum. Photoelectron spectra are generated and the streaking is simulated in two opposite directions corresponding to the electrons propagating along the streaking electric field and opposite to it. After obtaining the streaked spectra of the photoelectrons and using their non-streaked spectrum, the rms photon pulse length is calculated following the standard analysis procedure based on equation 1.42.

In the beginning of the simulation, a number of photoelectrons is generated depending on the length of the ionizing photon pulse. Here the number of photons per unit length of the pulse is considered the same for all the pulses and, therefore, the number of created photoelectrons is taken to be proportional to the pulse lengths. Each photoelectron is simulated by a Monte Carlo method called rejection sampling (acceptance–rejection) [93, 94]. The procedure of the simulation advances with the following steps: first, a random point t_i is taken along the temporal profile of the photon pulse, which corresponds to the position of the photon field that would ionize the electron. Another random number a is generated between 0 and 1 that defines if the photoionization at the selected point t_i should be considered or not. The number is compared to the value of the normalized temporal intensity profile $\hat{P}(t_i) = P(t_i)/P_{max}$ at the taken point. If the amplitude $\hat{P}(t_i)$ is bigger than the generated number a , the chosen point is accepted and a photoelectron is produced from the position t_i of the photon pulse. This procedure is repeated until the expected number of photoelectrons is created. The initial non-streaked energy of each electron is randomly generated from the Gaussian distribution of the emission spectrum, $W_0 = R_n(\mu, \sigma)$, where R_n represents a function generating random numbers with a normal distribution. The mean value μ in the function is the central energy equal to the mean energy of the photon pulse minus the binding energy: $\mu = \hbar\omega_{photon} - I_{bind}$, while the rms spectral width σ corresponds to the 50 as ionization time.

When the final spectrum of the electrons is registered by the eTOF spectrometer, its acceptance function should be convoluted with the spectrum. It is added in the expression for the energy

of a non-streaked electron detected by the spectrometer:

$$W(t_i) = W_0 + R_n(\sigma_{eTOF}) + ct_i, \quad (2.1)$$

where σ_{eTOF} is the resolution of the spectrometer, while the term ct_i is the contribution from a linear chirp along the photon pulse. As the photon pulses delivered by the FEL facilities may have a linear energy chirp along their temporal profile, it is included in the simulation to check the effect of the chirp in the pulse length calculations. The chirp c in equation 2.1 is defined as the change of the central energy of photons along the pulse per unit time. It is used in the calculations in [meV/fs] units. The effect of the non-linear chirp is not discussed in this simulation as this effect is typically negligible at FEL facilities.

Analogously, the final kinetic energy of an electron that is streaked in the THz field can be written as

$$W_{st}(t_i) = W_{ch}(t_i) + R_n(\sigma_{eTOF}) \pm \sqrt{8U_p W_{ch}(t_i)} \cdot \sin(\omega_{THz} t_i). \quad (2.2)$$

The term $W_{ch}(t_i)$ here is the kinetic energy of the electron before streaking, including also the effect from the linear chirp. The last term on the right hand side is the energy streaking in accordance to equation 1.40.

Based on the equations 2.1 and 2.2, energy values are generated and assigned to the number of photoelectrons produced by each photon pulse. As the non-streaked spectrum and the two streaked spectra are registered independently by different detectors during the measurements, the simulation procedure generates a new set of random numbers for each of these spectra. This ensures that the effect of statistical fluctuations of the spectra is included in the model for the pulse length calculation process. Figure 2.2 shows different photoelectron energy spectra simulated as eTOF spectrometer measurements. These energy values are generated by the procedure described above and correspond to photon pulses of 1.5 fs (top spectra in the figure) and 16 fs (bottom spectra in the figure) at a photon energy of 12400 eV. One can see from figure 2.2 that the spectra from the shorter pulse have larger statistical fluctuations due to the small number of created electrons, while the spectra from the longer pulse have more electrons and look smoother and closer to a Gaussian profile. On the other hand, figure 2.2 shows also that the streaked spectrum (d) from the long pulse is clearly broader than the non-streaked spectrum (c), while for the short pulse the broadening is not visible (about 0.2 eV).

2.2.3 Pulse length calculation

After recreating the electron spectra from the simulations, the rms pulse length can be calculated using the spectral width differences $\Delta\sigma_+$ and $\Delta\sigma_-$ from equation 1.42.

As the quantities $\Delta\sigma_+^2$ and $\Delta\sigma_-^2$ are defined as the quadratic difference of the streaked and the non-streaked spectra, they may have also negative values when the statistical fluctuations of the spectra are larger than the spectral broadening due to the streaking itself. This may result in a negative sign under the square root in equation 1.42 making the pulse length value imaginary. Such a result is an artifact of the evaluation process and does not have any phys-

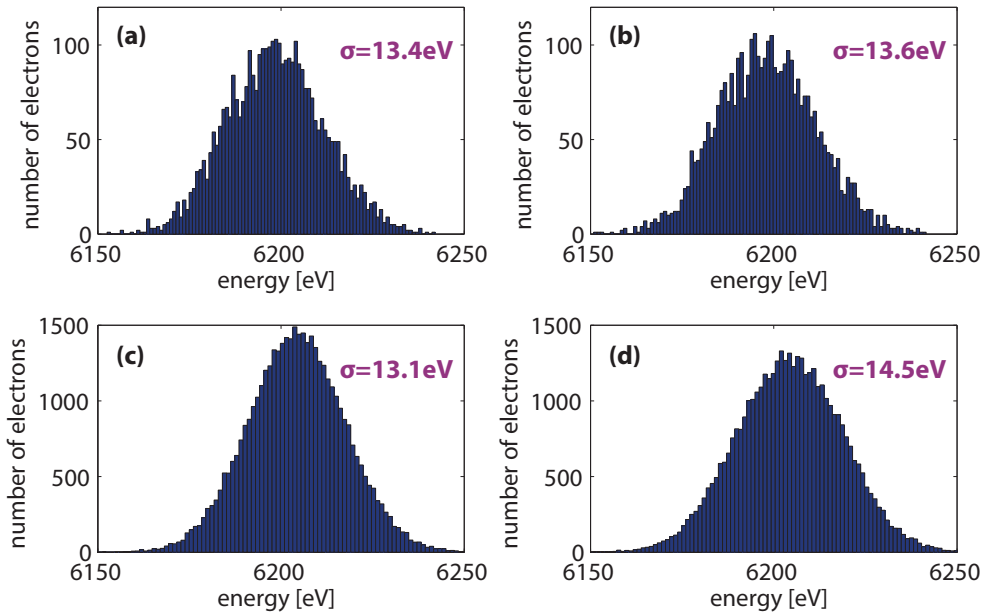


Figure 2.2: Energy distribution of the photoelectrons generated by the simulation. Distributions (a) and (b) correspond to the electrons created by a 1.5 fs-long pulse and show the non-streaked and streaked spectra, respectively. Analogously, (c) and (d) are the corresponding spectra of electrons from a 16 fs-long photon pulse.

ical meaning. For this reason the simulation code has to check and reject these imaginary values that appear especially in case of short photon pulses, where the difference between the streaked and non-streaked spectral widths is small, while the statistical fluctuations of the spectra are large (as shown in figure 2.2). When the non-physical values are filtered out, the distribution of the remaining values is no longer symmetric around the mean value and has a cut-off at the zero length. This skews the final value of the average pulse length, shifting it towards higher numbers. Such a result means that the acceptance rate of a calculation set can also affect the accuracy of the results. This effect is observed in the simulations for short pulses and is discussed in the next section. In order to have a better estimation of a pulse length in average after many shots, one can keep the square value of the pulse lengths including also the negative ones. In this case the distribution of the obtained values will be symmetric around the mean and the square root of this mean value will describe the average pulse length more accurately. The simulation procedure here concentrates only on single-shot measurements filtering out the imaginary values, and the calculated mean pulse lengths give more the upper limit for the short pulses rather than measuring the actual values.

The rms spectral widths used for the pulse length calculation were obtained in two different ways. The first way was to perform a Gaussian fit to the spectrum and take the standard deviation value of the fit as the rms width of the spectrum. This fitting procedure is the one most commonly used in the data analysis. In addition, the theory of the THz streak camera is developed for Gaussian pulses as discussed in the previous chapter. The second method

used for the pulse length calculation was to evaluate the standard deviation of the spectrum directly from the photoelectron energy distribution (shown in figure 2.2). This method does not depend on the shape of the electron spectra and can provide accurate results even for non-Gaussian spectra. However, it is less often used in the data analysis as the spectra registered during the measurements have also a background signal from other electrons (from other shells or Auger electrons), and defining the precise range for the spectrum of a particular line for each photon pulse is challenging.

After calculating the pulse lengths, the obtained results are compared to the lengths of the input pulses.

2.3 Results of simulation and discussion

The rms durations of all 178 FEL pulses were calculated by the procedure described in section 2.2. The spectral widths were obtained by either performing Gaussian fits to the spectra or calculating the standard deviation of the energy distribution of the electrons. The results obtained by fitting Gaussian profiles to the energy spectra are presented in table 2.1 for 11 different photon pulses with rms durations ranging from 1.5 fs up to about 40 fs. The rms lengths of the input pulses, the mean lengths delivered by the simulation and the accuracy of these mean values are shown in the table. For each of the presented pulse lengths, the standard deviation of the values delivered by 100 consecutive simulations are also shown in the table. The difference between the hard and soft X-ray pulses is that the energy of the

Table 2.1: Photon pulse lengths calculated by performing Gaussian fits. Mean values of the obtained lengths (Calc. mean) with their standard deviations (St. dev.) and accuracies (Acc.) are compared with the initial lengths (Initial).

Photon energy	Initial [fs]	Calc. mean [fs]	St. dev. [fs]	Acc. [fs]
12.4 keV	1.5	8.0	3.9	6.5
	1.6	7.3	3.2	5.7
	5.5	7.3	2.4	1.8
	11.3	11.1	1.6	0.2
	16.9	17.4	0.9	0.5
1.24 keV	19.4	20.7	6.2	1.3
	22.2	21.7	6.1	0.5
	26.3	26.1	5.1	0.2
	30.2	30.3	3.9	0.1
	35.8	36.6	3.2	0.8
	39.1	40.0	2.6	0.9

created electrons before streaking is different and therefore, they are streaked by different amounts according to equation 2.2. The higher the initial energy of the electrons, the greater is the absolute streak of the spectra. This means that if both types of electrons are detected by the eTOFs with the same resolution, then the more streaked spectra should give better accuracy and precision. Such an outcome can be observed in table 2.1, showing better results

Chapter 2. Simulation of the streaking process

for the more energetic 6200 eV electrons produced by the hard X-ray pulses at similar pulse lengths (e.g. pulses of 16.9 fs and 19.4 fs).

For short photon pulses the amount of imaginary values for the pulse length that occur due to statistical fluctuations of the spectra, is about 50%. As these non-physical results are rejected by the simulation, the average pulse length is shifted towards higher values which can be seen in table 2.1. For the pulses of about 5 fs rms the acceptance rate is about 75% and it reaches 100% for the longer pulses.

The second way to evaluate the widths of the electron spectra was to calculate the rms widths directly from the simulated data. The spectral widths obtained by this method describe the spectrum better and are not dependent on the shape of the peaks, so the calculated pulse lengths are more accurate. The mean values obtained this way are shown in table 2.2 with their standard deviations and accuracies for the same photon pulses as in table 2.1. As one can see from the table, the calculated mean lengths for the short pulses are shifted towards higher numbers. As in the previous case, such a result is caused by the high rejection rate of

Table 2.2: Photon pulse lengths calculated using the rms widths of the spectra. Mean values of the obtained lengths (Calc. mean) with their standard deviations (St. dev.) and accuracies (Acc.) are compared with the initial lengths (Initial).

Photon energy	Initial [fs]	Calc. mean [fs]	St. dev. [fs]	Acc. [fs]
12.4 keV	1.5	6.6	2.6	5.1
	1.6	7.0	2.5	5.4
	5.5	5.8	2.3	0.3
	11.3	11.2	1.0	0.1
	16.9	17.0	0.7	0.1
1.24 keV	19.4	20.0	4.5	0.6
	22.2	21.1	4.1	1.1
	26.3	26.1	3.0	0.2
	30.2	29.9	2.7	0.3
	35.8	35.9	1.9	0.1
	39.1	39.0	1.6	0.1

the non-physical pulse length values (about 50%). About 85% of the pulses with rms length of 5 fs are accepted in the simulation, and for the longer pulses the acceptance rate is 100%.

The comparison of the results delivered by the simulations and the initial pulse lengths for all 178 pulses is illustrated in figure 2.3. The subfigures 2.3a and 2.3b show the results from Gaussian fitting and rms width calculation methods, respectively. The vertical bars in the figure represent the precision of the calculation which is the standard deviation of a set of calculations for each photon pulse. In case of short photon pulses, when the statistical fluctuations of the spectra are large, the precision is about 6 fs for Gaussian fitting and about 4 fs for the rms width methods. Meanwhile, the precision improves for longer pulses going down to sub-femtosecond, as the number of created electrons in this case is bigger, reducing the statistical fluctuations in the calculation. Figure 2.3 also shows that the precision is better for hard X-ray photon pulses as they correspond to a stronger streaking.

The pulse length values obtained by the simulation for the photon pulses of about 1 fs provide only the upper limit of the pulse length and they are shifted towards higher numbers due to the high rejection rate of the non-physical values for pulse lengths. For this reason the

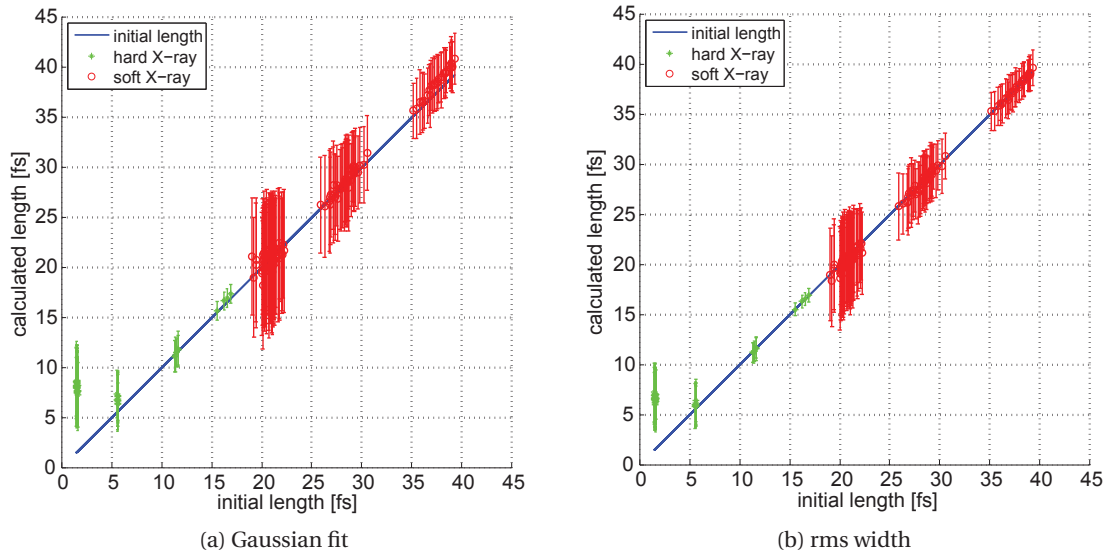


Figure 2.3: Simulation results for Gaussian fitting (a) and the rms widths (b). The blue diagonal line represents the initial rms pulse lengths, the green triangles and the red circles are the calculated average lengths for photon energies of 12400 eV and 1240 eV, respectively. The vertical bars correspond to the standard deviations from 100 shots.

accuracies of the calculated mean values in this case are about 6 fs and 5 fs for Gaussian fitting and the rms width methods, respectively. For the pulses of 5 fs and longer the accuracy is about 2 fs and down to sub-femtosecond.

The results from the two different ways of obtaining the spectral widths are compared in figure 2.4. It shows the accuracy of the obtained pulse lengths (subfigures (a) and (b)) and the precision of the calculations (subfigures (c) and (d)) provided by both methods. The plots on the left and right sides correspond to the results from the pulses with photon energies of 12400 eV and 1240 eV, respectively. As the subfigures (a) and (b) show, the accuracy for both methods is similar, and is better than 2 fs for most of the photon pulse lengths. A significant difference between the methods can be observed for the shortest and the longest pulses. In the case of short pulses, the number of the created electrons is not sufficient to recreate a smooth Gaussian profile of the energy spectrum (figure 2.2), and the Gaussian fit does not represent the spectrum well, whereas for the longer pulses the streaked spectra have a more flat-top shape than Gaussian. In such cases, directly calculating the rms widths of the spectra is preferable. The bottom part of figure 2.4 shows a clear improvement of precision with longer pulses. Such a result is consistent with the model as the longer pulses produce smaller statistical errors making the results more reproducible.

The figure also shows that the precision is better for hard X-ray photons corresponding to

Chapter 2. Simulation of the streaking process

more streaking of photoelectrons compared with the soft X-ray case, even though the latter corresponds to longer pulses. This shows that the lack of photoelectrons can be compensated

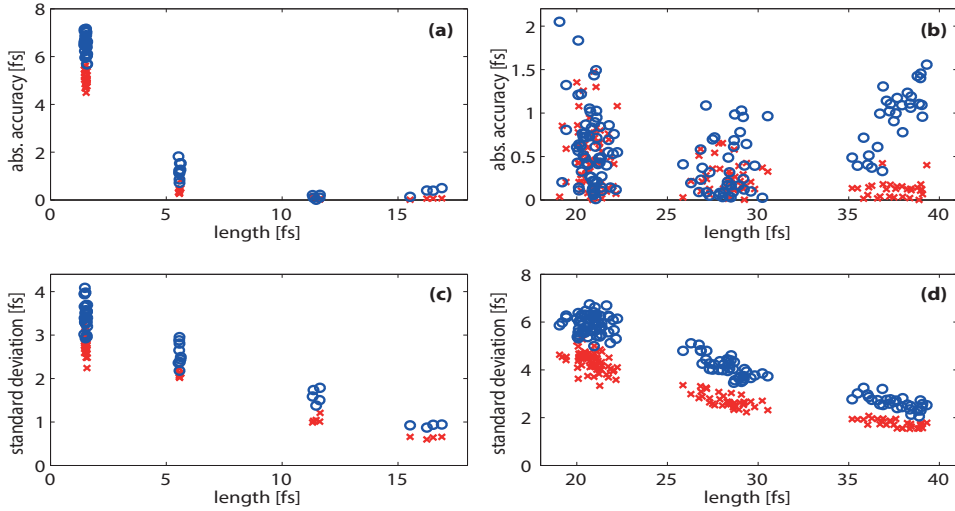


Figure 2.4: Subfigures (a) and (b) show the absolute accuracies, while (c) and (d) show the standard deviations from 100 simulations for each pulse length. The plots on the left correspond to photon energy of 12400 eV, and the ones on the right - to 1240 eV. The blue circles indicate the results from Gaussian fitting whereas the red crosses show the results from the method using the rms widths.

by stronger streaking fields, reducing the contribution of the statistical fluctuations in overall uncertainties of the calculations.

The precision of the calculations using Gaussian fitting is slightly worse than for the method with the rms widths. The reason for such a result is that the fitting process introduces an additional error in the calculations from shot to shot.

The simulation results show that Gaussian fitting can be applied in most of the cases when the electron spectra have Gaussian shape. This method is easier to implement during the data analysis of the measurements and does not induce a significant error in the case of the mentioned setup. On the other hand, when the electron spectra are not Gaussian, the method with the rms width should be utilized for more accurate results.

Figure 2.4 indicates a better accuracy and precision for more energetic electrons (created by the 12400 eV photons) as they correspond to more absolute streaking. Such a result was obtained assuming that the eTOFs measure both types of the electrons with the same resolution. However, when the energy of the photoelectrons is too high, they will not be detected by the eTOFs with sufficient resolution, which will affect the pulse length measurement accuracy. For this reason, to achieve a better accuracy and precision, it is preferable to increase the streaking field of the THz pulse instead of using more energetic electrons.

The simulation procedure concentrates only on the effects caused by the statistical fluctuations of the photoelectron spectra and by the limited resolution of the eTOF spectrometers used in the experiments. These effects were dominant for the experimental setups described

in [47, 68, 78]. It is possible to reduce the uncertainties and errors caused by these effects by increasing the streaking strength and the number of created photoelectrons. It is worth noting, however, that in this case other sources of uncertainties may become dominant: for strong streaking field, for instance, small fluctuations of the field strength may cause large errors in the measurements, which implies stricter stability requirements for the streaking THz pulse. In the case of using higher gas densities to produce more photoelectrons, the space-charge effect may become larger than an electronvolt, causing a detectable broadening of the spectrum which will affect the final results. Nevertheless, by choosing and carefully monitoring the mentioned parameters of the experimental setup, it is possible to achieve a measurement accuracy of a femtosecond and better at any given pulse length.

The simulations show that the THz streak camera method is capable of measuring photon pulses in a wide range of pulse lengths (from about 1 fs to 40 fs and possibly longer) in both hard and soft X-ray regions. The obtained results validate the theory of the THz camera not only for Gaussian photon pulses but also for pulses with more complex temporal profiles (SASE and self-seeding). Based on a realistic experimental setup, the simulation shows that an accuracy of about 1 fs can be achieved for the pulses of 5 fs and longer by choosing an optimal data analysis method. The results also show possible ways of improving the measurement accuracy for even shorter FEL pulses.

3 Experimental setup

This chapter describes the experimental setup used in the measurements performed for this thesis. A prototype THz streak camera called pulse arrival and length monitor (PALM) was built at PSI to test the concept of measuring hard X-ray FEL pulses with a light-field streak camera method. The prototype setup was used during the measurements with an HHG source at PSI and a hard X-ray FEL source at SACLA [6, 95]. After successful measurements with the prototype setup, the next generation PALM was designed and constructed with the aim of providing more flexibility and a better performance. The second generation setup was also tested at SACLA. This chapter also discusses some phenomena occurring at different parts of the system that may affect the accuracy of the measurements. It further defines the significance of these effects and shows ways of compensating for them.

3.1 Prototype setup

The prototype PALM setup was designed and built at PSI as a THz streak camera with a gas target. The system consists of a vacuum chamber and a THz generation setup positioned next to it. The vacuum chamber is made of μ -metal, which ensures the shielding of the processes inside the chamber from external magnetic fields. The schematic view of the measurement system is presented in figure 3.1. The X-ray (UV) photon pulses propagate along the chamber and ionize the gas atoms on their way. The THz beam is inserted into the chamber from a side through a Z-cut quartz window. A parabolic mirror with a focal length of 170 mm is positioned inside the chamber to focus the THz beam on the interaction region. The mirror has an aperture of 5 mm to let the X-ray pulses through. The gas atoms propagate vertically from the top of the chamber. When the gas pulse and the copropagating THz and X-ray beams are overlapped in time and space, the photoionization process and a consequent streaking of the produced photoelectrons take place.

When the atoms of noble gases are ionized by a linearly polarized photon beam, the angular distribution of the created photoelectrons is not uniform [96, 97], and it is expressed by the

Chapter 3. Experimental setup

following formula

$$\frac{d\sigma(\hbar\omega)}{d\Omega} = \frac{\sigma(\hbar\omega)}{4\pi} \left[1 + \frac{\beta(\hbar\omega)}{2} (3\cos^2\theta - 1) \right], \quad (3.1)$$

where σ is the photoionization cross-section, $\hbar\omega$ is the photon energy and θ is the angle between the electron propagation direction and the polarization of the ionizing electric field. The term β is the asymmetry parameter that defines the angular distribution of the electrons. It depends on the electron shell that is being ionized and the energy of the ionizing photon.

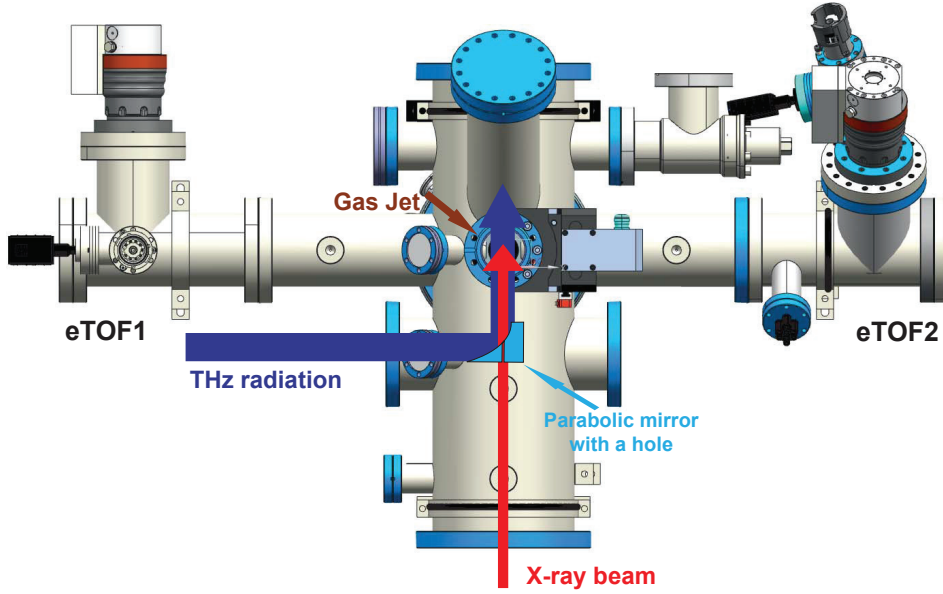


Figure 3.1: Schematic view of the prototype PALM setup. The red arrow represents the X-ray beam while the blue line corresponds to the streaking THz pulse that enters the chamber from the side. The gas jet shown by a brown arrow comes from the top.

It can be seen from equation 3.1 that for a non-zero value of the β parameter the angular distribution of the electrons has a maximum in the plane of polarization of the ionizing field, where $\cos\theta = \pm 1$. This asymmetry grows with higher photon energies, which means that for hard X-ray photon pulses with a linear polarization the majority of the electrons propagates in the polarization plane. For the p shells of xenon (Xe) gas, mostly used in the measurements, the β parameter is about 1.5 and higher, making the angular distribution of the electrons asymmetric. Taking this effect into account, the electron time-of-flight spectrometers are installed in the plane of the X-ray beam polarization to maximize the amount of the registered photoelectrons. As it is shown in figure 3.1, the two eTOFs are positioned on the opposite sides of the chamber and face towards the interaction region (center of the chamber). The polarization of the THz radiation is also linear and is in the same plane as the eTOFs. This geometry allows the eTOFs to detect those electron spectra that are streaked maximally along the THz field and opposite to it, in accordance to equation 1.40. The presence of the two eTOFs not only excludes the effect of the linear chirp in the pulse length calculation discussed

in section 1.3, but also compensates the photon energy jitter of the FEL pulses as both eTOFs measure the spectra from the same FEL pulse.

The gas jet is injected into the chamber from the top using an "Amsterdam" cantilever piezo-electric valve, which can deliver gas pulses of various durations with a frequency of up to 5 kHz. The description of the valve and the characterization of the gas pulse is given in [98, 99]. The opening time of the valve can be controlled to adjust the amount of gas injected into the chamber. By optimizing the opening time and the backing pressure of the valve, the highest particle density is achieved at the interaction point. Utilizing a pulsed gas jet increases the amount of ionization in the chamber. For the same vacuum level inside the chamber, the gas pulses provide particle densities at the interaction region that are orders of magnitude higher compared to the case, when the chamber is flooded by a continuous flow of a gas. A high particle density at the interaction point is crucial for the hard X-ray photon pulse measurements as the ionization cross-sections in this case are very low [38]. Xenon gas was used in the setup as it has a relatively high photoionization cross-section for hard X-ray photons. Moreover, for our experimental conditions a clustering of Xe atoms takes place that increases the ionization rate. The cluster formation occurs because of a rapid cooling of the gas jet due to its fast expansion from the gas nozzle into the vacuum [100]. This results in a higher density of the Xe atoms in the gas jet and increases the ionization rate. During the measurements some tests were performed also with helium (He) gas.

The gas nozzle has a diameter of 150 μm and an opening angle of 40° . It is positioned 25-30 mm away from the interaction point. This distance can be controlled and it is chosen in a way to avoid a collision of the nozzle with the eTOFs and to provide a high particle density of the gas pulse at the interaction region.

An electron time-of-flight spectrometer is a detector most commonly used in atomic, molecular and surface physics to study the electronic structure of materials. It consists of a tube, along which the electrons drift, and a microchannel plate (MCP) detector at the end of the tube, where the electrons are detected. The MCPs measure the time that takes for the electrons to travel from the ionization point to the detector through the drift tube. From the measured time of flight the energy spectrum of the electrons can be found. For this purpose the expression for the kinetic energy of a non-relativistic electron is used:

$$\frac{m_e}{2} \left(\frac{dx}{dt} \right)^2 = W_k. \quad (3.2)$$

Here W_k is the kinetic energy of the electron and dx/dt is its velocity. Integrating equation 3.2 over time t and solving it for W_k results in a simple expression:

$$W_k = a + \frac{b}{(T - c)^2}, \quad (3.3)$$

where T is the time of flight of the electron. The coefficients a , b and c are the calibration constants and their values are required for retrieval of the energy spectra. By measuring the energy spectrum of the electrons, the eTOF gives information about the electronic structure of the material emitting these electrons. An example of a setup utilizing eTOF detectors and a

Chapter 3. Experimental setup

description of the eTOF operation is given in [101].

The photoelectrons created by a hard X-ray FEL pulse from noble gas atoms have kinetic energies of several keVs. The resolution of a time-of-flight spectrometer is dependent on the flight time of the particles and it gets worse with higher kinetic energies caused by the inverse square root dependence of the flight time on the kinetic energy (as can be derived from equation 3.3). In order to measure the spectra of such energetic electrons, the setup uses modified Kaesdorf ETF20 electron TOFs. These detectors utilize electrostatic retardation and lensing system that allows to measure electrons with kinetic energies of up to 10000 eV with a resolution of few electronvolts. The retardation slows the high-energy electrons down to measure their time of flight with a better resolution, while the lensing system guides the electrons to the MCPs ensuring a high count rate and a good signal-to-noise ratio. The values for the retarding drift tube voltage and for the lens voltage need to be carefully chosen for electrons with different kinetic energies to achieve a high measurement resolution and to obtain a large temporal (energy) window of detection. Such a large dynamic range of detection is required to measure not only the non-streaked electron spectra but also the spectra that experience shift in energy in presence of the streaking THz field. For electrons with a kinetic energy of several keVs, a dynamic range of about 200 eV is required for the eTOFs. In order to optimize the retardation and lensing settings in the eTOF, the simulation code SIMION was used [102, 103]. The code mimics the structure of the eTOFs used in the measurements and it tracks the propagation of the electrons from the source to the MCPs. As a result, the simulation outputs the times of flight of all the electrons detected by the MCPs. The view of an eTOF and trajectories of different electrons tracked by SIMION are shown in figure 3.2. The simulation shown in the figure is done for 150 electrons. One can see from the simulation that not all

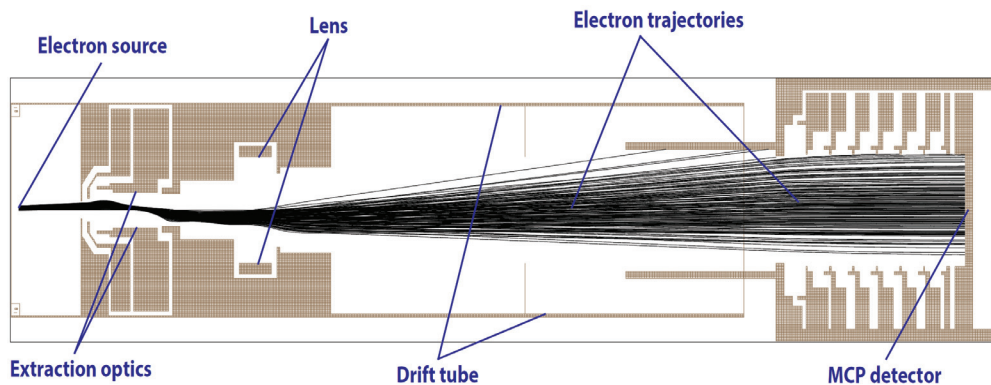


Figure 3.2: Graphical view of the eTOF and the trajectories of the electrons tracked by SIMON simulation tool.

the electrons reach the MCP detector and some of them are lost on the way. By changing the value of the lens voltage, it is possible to maximize the number of electrons arriving to the MCP detector and thereby optimize the signal.

The length of the eTOFs used in the setup is about 50 cm from the entrance to the MCP detector. The entrance aperture size is 7 mm in diameter with an acceptance angle of 7 degrees. The

tips of the two eTOFs are positioned 25 mm away from the interaction region on opposite sides. This distance is chosen to maximize the amount of the photoelectrons entering the eTOFs and also to avoid an interference of the eTOFs with the gas jet or the radiation beams. The MCPs can operate only at a pressure of 10^{-6} mbar or lower. Such pressure is obtained using a pumping system consisting of two rotary prepumps and 3 turbomolecular pumps of HiPace series from "Pfeiffer". Two HiPace pumps with a pumping speed of 300 L/s are attached to eTOFs, close to the MCPs, while the third HiPace pump with a speed of 1200 L/s is positioned under the chamber, below the interaction region, to collect the atoms and the ions of the gas jet.

The THz generation setup is positioned on an optical table next to the vacuum chamber. The setup uses a lithium niobate crystal for the THz generation with tilted optical pulse front method. Further details about the THz generation setup are given in [59]. The generated beam is a linearly polarized single-cycle THz pulse with an overall duration of about 2000 fs (about 0.52 THz) and a linear part of about 600 fs. The THz pulse enters the vacuum chamber from the side through a Z-cut quartz window that has a transmission of 60% at such frequencies. The electric field strength of the THz radiation was about 6 MV/m at the interaction point. Some of the optical components are positioned on a motorized linear stage that allows to change the position of these components causing a change in the arrival time of the THz pulse. This stage is used to scan the delay between the THz pulse and the ionizing photon pulse, which helps to find the temporal overlap between these two pulses and also to map the shape of the THz pulse during the measurements as discussed in chapter 4.

The prototype setup allows the measurement of the photoelectron spectra either with a THz beam or without it. This fact makes it impossible to compare the streaked and the non-streaked spectra created by the same photon pulse, and the photon pulse length can only be evaluated statistically, by comparing the two spectra from different photon pulses.

3.2 Second generation setup

The first measurements with the prototype setup revealed possible ways of improving the measurement system. These improvements were incorporated in the second generation PALM, which also was designed and built at PSI. The main difference of the new design compared to the prototype setup is the presence of the second interaction point. The schematic view of the new system is presented in figure 3.3. There are two piezoelectric valves on the top of the chamber that inject the gas pulses along the FEL beam. The X-ray beam propagates through the chamber and ionizes the two gas pulses along its path. The first interaction region does not have a THz beam and the created photoelectrons are not streaked, while the electrons at the second interaction point are exposed to THz radiation. The THz pulse is generated on the optical table positioned next to the vacuum chamber with a generation setup similar to the prototype. The generated THz pulse has a duration of about 1700 fs (frequency of 0.6 THz). After entering the vacuum chamber from the side, the THz pulse is focused onto the second interaction point by a parabolic mirror installed inside the chamber. In the new

Chapter 3. Experimental setup

design the mirror has a focal length of 150 mm to have a stronger focusing of the THz beam. As a consequence, the electric field at the second interaction zone is 8 MV/m. The photoelectrons created at the two interaction regions are registered by three eTOF spectrometers. One of the eTOFs is positioned at the first interaction region and measures the energy spectrum of the non-streaked electrons, while the other two eTOFs are installed at the second interaction zone, on both sides of the chamber, and they measure the electron spectra streaked in opposite directions. The geometry of the eTOFs and the gas valves as well

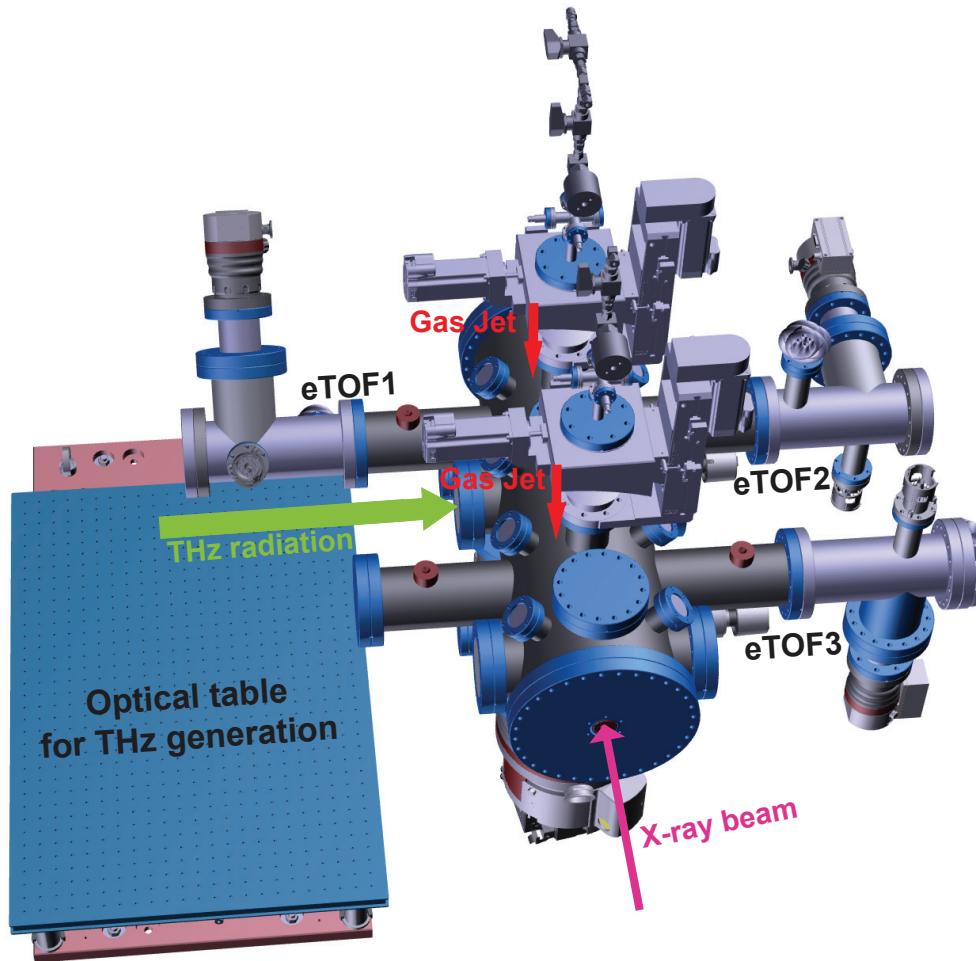


Figure 3.3: Outline of the second generation PALM setup with two interaction regions. The pink and green arrows show the FEL and THz beams, respectively. The two gas jets are shown by the red arrows. The THz radiation is generated on the optical table positioned next to the vacuum chamber.

as the positions of the gas nozzles with respect to the interaction points are the same as for the prototype setup. The distance of the eTOFs from the interaction regions is designed to be 25 mm for the new setup, as for the prototype, but it was increased to 45 mm during the measurements for technical reasons.

The configuration with two interaction points allows to measure the non-streaked spectrum of

3.3. Accuracy considerations for the experimental setup

the photoelectrons and the two spectra streaked in opposite directions (given in equations 1.41 and 1.42) created by the same photon pulse. This gives the opportunity of measuring the photon pulse length on a single-shot basis. The detection of the three spectra from the same FEL pulse allows also to eliminate the uncertainty caused by the spectral width jitter of the FEL pulses from shot to shot.

The vacuum chamber of the new design is built such that the two interaction regions are identical to each other. Such a design allows having a THz beam at the first interaction point as well. This makes it possible to obtain two identical streaking processes at both interaction regions. The presence of the two interaction zones makes the system more flexible, allowing different measurement configurations. It is possible, for example, to have a streaking at both interaction regions by two THz pulses with a 90° phase shift relative to each other. In this case the dynamic range of the measurements can be increased as the photon pulses can be measured arriving at the linear part of either of the THz pulses. For two streaking zones it is also possible to use streaking pulses with higher frequencies and stronger streaking fields. This will result in an improvement of the measurement resolution while maintaining the dynamic range the same [47]. More details are discussed in section 5.2.

The second design of the PALM setup has been tested at SACLA and will be utilized at SwissFEL for temporal photon diagnostics.

3.3 Accuracy considerations for the experimental setup

This section discusses various effects occurring at different parts of the experimental setup that may cause uncertainties in the pulse length and arrival time measurements. The overall accuracy of the measurements is addressed in chapter 4, while here only the contributions from separate effects are described.

Gouy phase shift: This effect was first showed in 1890 by Gouy [104, 105]. Gouy phase shift occurs in the focused laser beams causing a slight change in phase of the radiation along the propagation and a jump of π when passing through the focus. This phenomenon is well discussed in [106], and the observation of this effect in a single-cycle THz beam is described in [107]. In the simplest form, the Gouy phase shift in a Gaussian beam [108] can be written as

$$\psi = -\arctan\left(\frac{z}{z_R}\right), \quad (3.4)$$

where z is the longitudinal coordinate along the beam with $z = 0$ at the focus and z_R is the Rayleigh length. The latter denotes the distance from the focus over which the area of the transverse size of the beam is doubled and can be written as

$$z_R = \frac{\pi w_0^2}{\lambda}. \quad (3.5)$$

Here w_0 is the beam waist defined as the transverse size of the beam at the focus, while λ is the wavelength of the radiation. In the experimental setup described in this chapter a focused THz beam is used. Therefore, the streaking beam experiences a Gouy phase shift

Chapter 3. Experimental setup

along the interaction area. Figure 3.4 shows the range where the Gouy phase shift affects the measurements. Even though both the FEL and the THz beams propagate with the same velocity along the gas jet, the phase of the THz changes with respect to the FEL pulse, and the electrons ionized by the FEL pulse at different parts of the gas jet experience slightly different phases of the streaking field. The overall phase shift $\Delta\psi$ is defined solely by the focusing

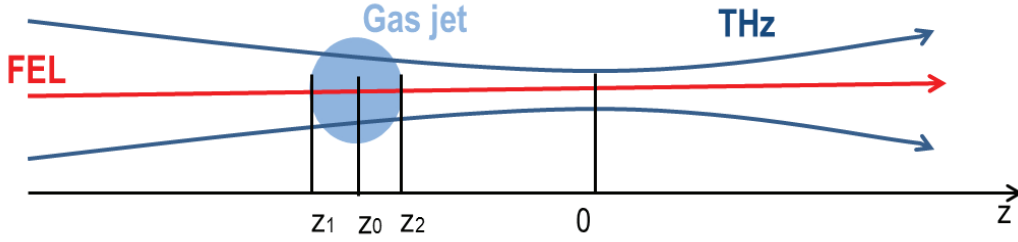


Figure 3.4: Illustration of the Gouy phase shift effect. The THz beam shown in blue is focused at the position $z = 0$ and it experiences a phase shift along the interaction region.

strength of the beam (z_R in equation 3.4) and the size of the gas jet along the beam that can be written as $\Delta z = z_2 - z_1$ from figure 3.4.

The effect of the Gouy phase shift on the photoelectron spectra and the pulse length calculation is addressed in [35]. It is shown there that the overall effect of the Gouy phase shift on the calculated pulse length can be written in the following form

$$\tau_{x,gouy}^2 = \tau_x^2 + \sigma_{g,t}^2. \quad (3.6)$$

Here $\tau_{x,gouy}$ is the rms duration of the FEL pulse with the effect of the Gouy phase shift, τ_x is the FEL pulse length without the Gouy phase shift taken into account and $\sigma_{g,t}$ is the temporal delay along the interaction region (gas jet) due to the phase shift. This delay can be expressed by the phase shift along the gas jet and the frequency of the THz pulse: $\sigma_{g,t} = \sigma_{g,\psi} / \omega_{THz}$. In order to find the phase shift $\sigma_{g,\psi}$, the size of the gas jet is required.

For purpose of the gas jet size measurement, an experimental setup was assembled and used at the OPTICS beam line [109] at the Swiss Light Source (SLS) at PSI. The OPTICS beam of 10000 eV photon energy and a transverse size of 140 μm was scanned along the gas jet transverse size, and the number of created ions was measured by an ion time-of-flight detector at each step. The results from these measurements showed that the transverse size of the gas jet (the size along the ionizing beam) is about 0.5 mm rms.

For the prototype setup the interaction region is 20 mm before the focus of the THz beam. Therefore, by using equation 3.4 for the positions $z_1 = -20.25$ mm and $z_2 = -19.75$ mm (gas pulse size of 0.5 mm), the phase shift is calculated to be $\sigma_{g,\psi} = 12.5$ mrad for a Rayleigh length of $z_R = 20$ mm. For such a phase shift and a THz frequency of 0.52 THz the contribution of the Gouy phase shift in overall pulse duration, given by the term $\sigma_{g,t}$ in equation 3.6, is about 3.8 fs. This value quadratically adds up with the actual rms pulse duration and, for example, for a pulse length of 10 fs the measured value will be about 10.7 fs.

As for the second generation setup, the interaction region is at the focus of the THz beam, and

3.3. Accuracy considerations for the experimental setup

the phase shift is calculated between the positions $z_1 = -0.25$ mm and $z_2 = 0.25$ mm providing a result of $\sigma_{g,\psi} = 28.4$ mrad for a Rayleigh length of $z_R = 17.6$ mm. Using these numbers, the term $\sigma_{g,t}$ is calculated to be about 7.5 fs for a THz frequency of 0.6 THz. For the same 10 fs photon pulse, considered above, the measured value of the pulse length will be about 14.1 fs with the new design.

The effect of the Gouy phase shift depends largely on the wavelength (frequency) of the streaking field. The dependence of $\sigma_{g,t}$ on the wavelength is quadratic:

$$\sigma_{g,t} \propto \frac{\sigma_{g,z}}{z_R} \cdot \frac{1}{\omega_{THz}} = \lambda_{THz}^2 \cdot \frac{\sigma_{g,z}}{2\pi^2 w_0 c}, \quad (3.7)$$

where $\sigma_{g,z}$ is the rms size of the gas along the THz beam, c is the speed of light and λ_{THz} is the THz wavelength. By utilizing higher THz frequencies (shorter wavelengths) it is possible to reduce the effect of the Gouy phase shift.

The contribution from the Gouy phase shift effect in the pulse length calculation depends also on the length of the photon pulse that is being measured; it can be less than a femtosecond for long pulses and up to several femtoseconds for shorter ones. The effect of the Gouy phase shift is taken into account in the data analysis of the measurements and the contribution from this effect is excluded in accordance to equation 3.6.

Space charge effect: This is a collective effect that occurs due to the Coulomb interaction between a large number of charged particles. When the electrons are released from the gas atoms during the ionization, a number of positively charged ions is created in the gas jet. The photoelectrons, therefore, experience a Coulomb attraction force from the ionic cloud left behind, and this force may affect the kinetic energy of the electrons causing an overall shift or broadening of their energy spectrum. As already mentioned in chapter 2, the space-charge effect from the ionization of a gas pulse was experimentally studied by [85]. It shows that the overall effect on the kinetic energy spectrum of the electrons from the space-charge is about 1 eV when the number of created electron-ion pairs is about 10^8 . Such a result was found for an incident photon energy of 38 eV and the corresponding photoelectron energies in range of 15-25 eV. During the measurements with FEL pulses the number of the ionized electrons was also in order of 10^8 but the kinetic energies of the photoelectrons were thousands of electronvolts. At such kinetic energies the space-charge effect is significantly smaller than 1 eV and cannot be resolved by the eTOF spectrometers. When measuring the photon pulses from the HHG source, on the other hand, the energy of the photoelectrons was in range of tens of electronvolts. However, the number of the photoelectrons created by the HHG pulses was in order of 10^6 , which, according to [85], corresponds to a space-charge effect of about 0.1 eV, which is also negligible.

The space-charge effect can occur also in the electron cloud itself when it propagates along the drift tube of the eTOF. The electrons collectively interact with each other by Coulomb repulsion which may result in a change of their spectral distribution. In order to estimate this effect quantitatively, simulations were done by the SIMION code. The results from the simulations show that the broadening of the energy spectrum of the electrons due to the Coulomb repulsion is less than 0.1 eV and, therefore, is negligible compared to the eTOF

resolution of few electronvolts.

It should also be noted that both the streaked and the non-streaked electron spectra are affected by the space-charge effect in a similar way and as these two spectra are deconvoluted from each other during the pulse length calculation, the effect of the space-charge in the final pulse length value is negligible.

Based on the arguments discussed here, the space-charge effect was neglected during the data analysis.

Angular distribution of the streaked electrons: When the photoelectron propagates at a certain angle with respect to the streaking electric field, the change of its kinetic energy due to the streaking depends on the cosine of this angle as given in equations 1.32 and 1.39. The aperture size of eTOFs is 7 mm in diameter, meaning that electrons with non-zero angular distribution can also enter the eTOFs. For the distance of the interaction region from the eTOF aperture of 25 mm the maximum angle that the photoelectrons may have to enter the eTOF is ± 0.14 rad with respect to the polarization of the THz field. During the measurements with the prototype setup the maximum amount of the energy gain of the electrons due to the streaking was about 70 eV. For the angular distribution of ± 0.14 rad of the electrons, the rms energy spread is then about 0.3 eV. This broadening is negligible compared to the broadening of few electronvolts due to the streaking effect.

For the second generation setup the distance between the interaction point and the eTOF entrance was 45 mm and the maximal energy transfer due to the streaking was about 100 eV. The overall broadening of the spectrum because of the angular distribution of the electrons was about 0.15 eV rms in this case, which is also negligible compared to the broadening from the streaking.

The obtained values show that the broadening of the spectrum caused by the non-zero angular distribution of the electrons entering the eTOFs does not affect the calculated pulse length significantly. Therefore, this effect can be neglected in the analysis procedure of the pulse length calculation.

Focusing lens in eTOF: As it was mentioned earlier in this chapter, the eTOFs utilize electrostatic lensing to focus the photoelectrons onto the MCPs. The focusing strength in this case depends on the kinetic energy of the electrons being focused. Photoelectrons that are focused differently will travel different distances inside the eTOFs and arrive to MCPs at different times. For the photon pulse length calculation the spectral widths of the streaked and non-streaked electrons are compared. When the photon pulse arrives away from the zero-crossing of the THz pulse (but still at the linear part), the streaked spectra experience not only a broadening but also an overall shift. Because of this shift the streaked electrons enter the eTOFs with a bigger or smaller kinetic energies compared to the non-streaked electrons and, therefore, the streaked and non-streaked electrons are focused differently in the eTOFs. This may result in a change of the width of the spectra measured by the eTOFs because of the energy shift of the electrons, which, in turn, will induce an error in the pulse length calculation.

In order to account for this effect, the spectral widths should be measured for different kinetic energies of the electrons without the streaking field. In this case one can observe the change of the spectral width when the central energy of the spectrum is changed. This allows to

3.3. Accuracy considerations for the experimental setup

estimate the effect of the energy shift due to the streaking on the measured spectral width and compensate for it during the data analysis procedure.

4 Measurements

This chapter describes three different measurements that have been performed to prove the concept of this thesis. The first measurements were done with a high harmonic generation source at PSI to test the light-field streaking method. The second series of measurements were carried out at SACLA [6, 95] to test the method with hard X-ray FEL pulses. After successful tests, the third measurements were performed to cross-correlate the THz streak camera method with other measurement techniques on a single-shot basis.

4.1 Measurements with an HHG source

In order to test the prototype experimental setup and to experimentally observe the light-field streaking effect, measurements were performed with a HHG source at PSI. These measurements allowed to test the performance of various components of the system and demonstrated the ability of the prototype PALM setup to measure the durations of the HHG pulses. Some of the measurement results are reported in [47, 68].

4.1.1 Measurement procedure with the HHG pulses and data processing

The measurements were performed using the HHG beamline available at PSI. The prototype PALM setup was connected to the beamline, and the ionizing HHG radiation was directed to the interaction point through the 5 mm hole of the parabolic mirror that focuses the THz pulse inside the PALM. A trigger synchronized with the HHG pulse was sent to the piezoelectric gas valve to inject the gas pulses to the interaction region. The backing pressure of the gas was about 2.5 bar above the atmospheric pressure. By scanning the delay of the trigger with respect to the HHG pulse, a temporal overlap was found between the gas jet and the ionizing HHG pulse.

Both the THz pulse and the HHG pulse were generated using a Ti:sapphire infrared (IR) laser of 800 nm wavelength. The rms duration of the IR pulses was about 39 fs with a pulse energy of 20 mJ. Utilizing the same infrared laser for both the HHG and the THz setups ensures

that the ionizing HHG pulse and the streaking THz pulse are intrinsically synchronized, and there is no temporal jitter between them. About 40% of the infrared laser power was used for the high harmonic generation setup. The harmonics were generated in a process described in section 1.5 by irradiating argon (Ar) pulses with the infrared laser. The spectrum of the created HHG pulses contains 9 odd harmonics of the pumping laser wavelength of 800 nm. The obtained spectrum is shown in figure 4.1. One can see from the figure that the photon

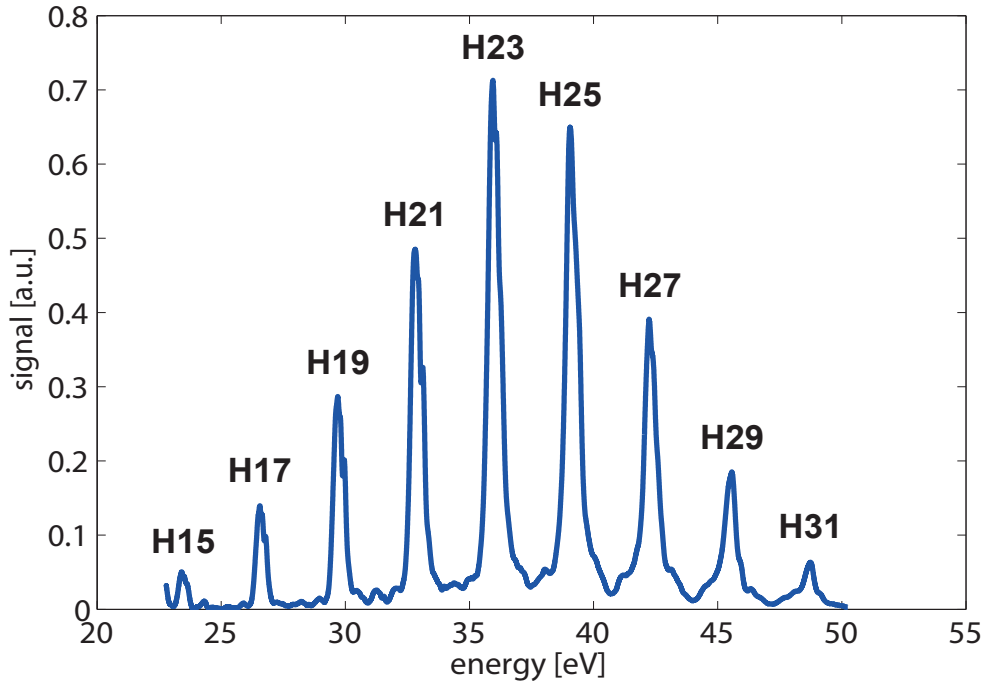


Figure 4.1: Spectrum of the HHG pulse containing the harmonics from 15th to 31st, measured by a grating spectrometer.

energies of the harmonics range from about 23.4 eV up to 48.7 eV, corresponding to the odd harmonics from 15th to 31st. The energy separation between the harmonics is about 3.17 eV. The spectrum shown in figure 4.1 was imprinted in the spectra of the photoelectrons ionized by the HHG pulses.

About 60% of the IR laser power was used to pump the LiNbO₃ crystal for the THz generation. As the THz and the HHG pulses were already synchronized, the temporal overlap between them was found by scanning the arrival time of the THz pulse relative to the HHG pulse. This is done by moving one of the optical components of the THz generation setup using a motorized linear stage and causing a change in the optical path of the THz pulse. The overlap is found when the eTOFs detect a shift in the energy spectra of the photoelectrons, which is caused by their interaction with the electric field of the THz pulse.

Two different types of gases were used in the setup during the streaking measurements. First tests were performed using xenon, ionizing two electron shells of $5p_{1/2}$ and $5p_{3/2}$ with binding energies of 13.4 eV and 12.1 eV, respectively. For this configuration two photoelectron spectra were detected for each harmonic resulting in 18 spikes in the overall spectrum for 9 harmonics.

In addition to xenon, helium (He) gas was also tested during the measurements. The HHG pulse ionized the electrons from the 1s shell of He with a binding energy of 24.6 eV. In this case only the electrons created by the last 6 harmonics were detected. The reason is that the harmonics with lower photon energies were either below the ionization threshold or the created photoelectrons did not have sufficient kinetic energy to reach the MCP detectors in the eTOFs. As a result, only the harmonics starting from the 21st were measured from the overall HHG spectrum.

Figure 4.2 shows the photoelectron spectra measured by the eTOFs in nanoseconds corresponding to the time-of-flights of the electrons. One can see the double spikes from Xe for each harmonic shown in figure 4.2a, while in case of He a single spike is measured per harmonic (figure 4.2b). It is visible from subfigure (a) that for an individual harmonic, the spike

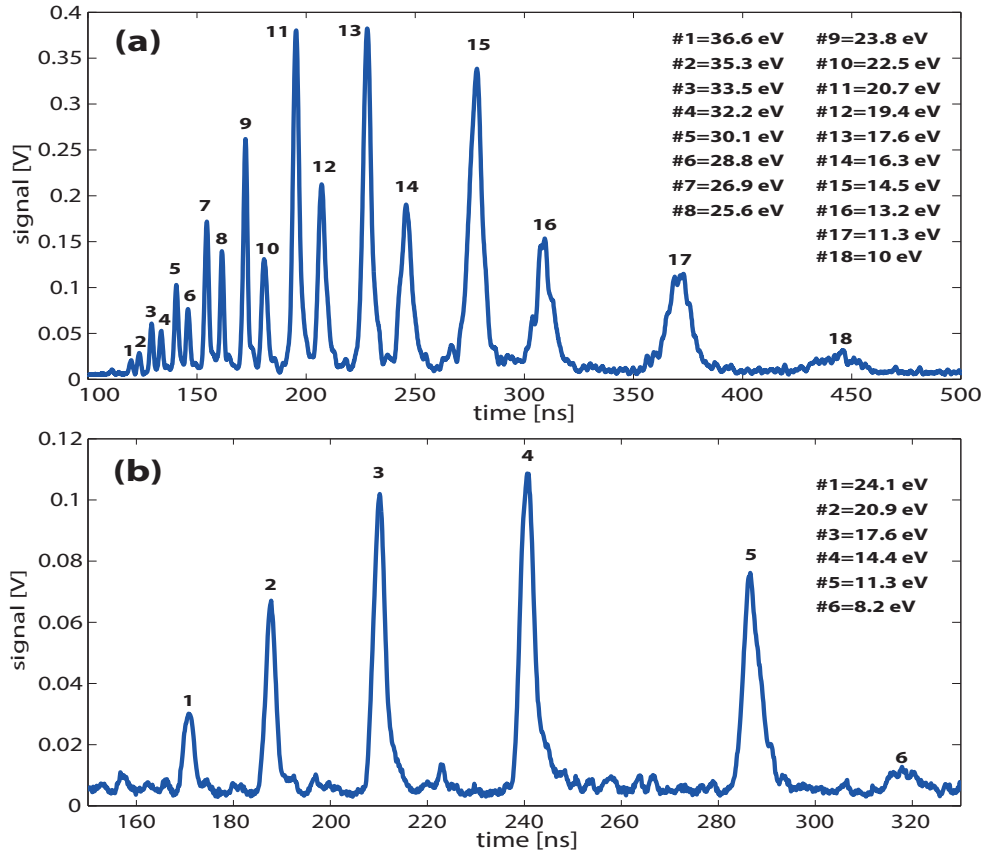


Figure 4.2: Photoelectron spectra from xenon gas (a) and helium gas (b) measured by eTOF spectrometers and averaged for 100 consecutive spectra. The spectra are shown in terms of flight time and each spike corresponds to a certain kinetic energy of the electrons shown in the figure.

corresponding to the electron shell $5p_{3/2}$ (labeled by an odd number in the figure) is higher compared to the spike from the $5p_{1/2}$ shell (even number in the figure). This is caused by the fact that the electrons from $5p_{3/2}$ shell have higher kinetic energies and, therefore, higher

probability to reach the MCP detectors in the eTOFs. Comparison of the spectra from the two gases in figure 4.2 also shows that the signal from xenon atoms is about 4 times higher compared to helium. Such a result is due to the fact that there are more electrons in the $5p$ shells of Xe than in the $1s$ shell of He. Furthermore, the number of atoms is higher in the Xe pulses because of the clustering effect [100], which increases the ionization rate as already mentioned in section 3.1.

The eTOF spectrometers measure the time it takes for the electrons to travel from the interaction region to the MCP detector. This is the reason why the spikes of the spectra shown in figure 4.2 are not equally spaced. To obtain the energy spectra of the electrons, the eTOFs need to be calibrated in accordance with equation 3.3 as already mentioned in section 3.1. In order to calculate the calibration coefficients, the spikes in the measured spectra need to be identified. Each spike should be related to the corresponding harmonic and the binding energy of the electron shell. The spikes are numbered in figure 4.2 and the corresponding central energies of the photoelectrons are indicated. These values are obtained by subtracting the binding energies of the relevant electron shells from the photon energies of each harmonic. The calibration curves with the corresponding coefficients obtained for Xe spectra are shown in figure 4.3. Using these constants, one can obtain the energy spectra of the electrons from their flight times.

After obtaining the calibration constants for both eTOFs, a delay scan was performed between the HHG pulse and the streaking THz pulse. For this purpose the optical path of the THz pulse

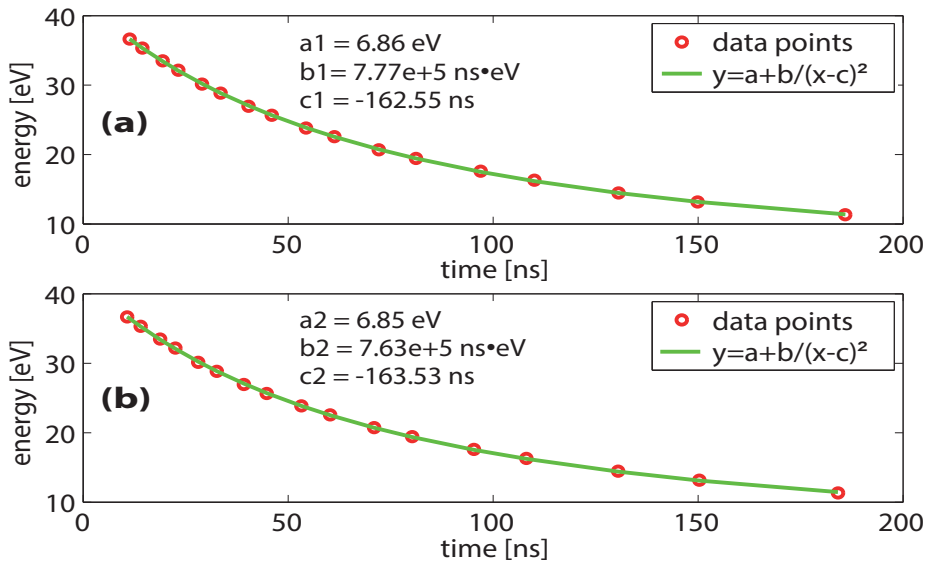


Figure 4.3: Calibration curves for eTOF1 (a) and eTOF2 (b). The red circles correspond to the data points and the green lines show the fitted curves.

was changed by moving one of the optical components in the THz generation setup using a linear stage. For each position of the delay stage, a different phase of the THz was observed at the interaction point and, therefore, the energy spectra of the photoelectrons were shifted by different amounts. During the scan with He gas the delay stage position was changed in

steps of $100\ \mu\text{m}$ causing about 670 fs change in the arrival time of the THz pulse. Meanwhile, in case of Xe a finer scan was performed with steps of $6\ \mu\text{m}$ corresponding to a delay of about 42 fs. For each position of the delay stage, 100 spectra were measured by the eTOFs. Figure 4.4 shows the evolution of the energy spectra during the delay scan with xenon (a) and helium (b). Unlike figure 4.2 that shows the flight times of the electrons, figure 4.4 shows the energy spectra after the calibration of the eTOFs. In this case the spikes in the spectra are equally spaced corresponding to the spacing of the harmonics. During the measurements with He the THz beam was not optimized, and the electric field strength at the interaction point was only about 0.25 MV/m, while for Xe the field strength was about 4.5 MV/m. This is clearly visible in figure 4.4, where the spectra in (a) are shifted in energy much more than the spectra in (b), corresponding to the scans with Xe and He, respectively. One can also see from the figure

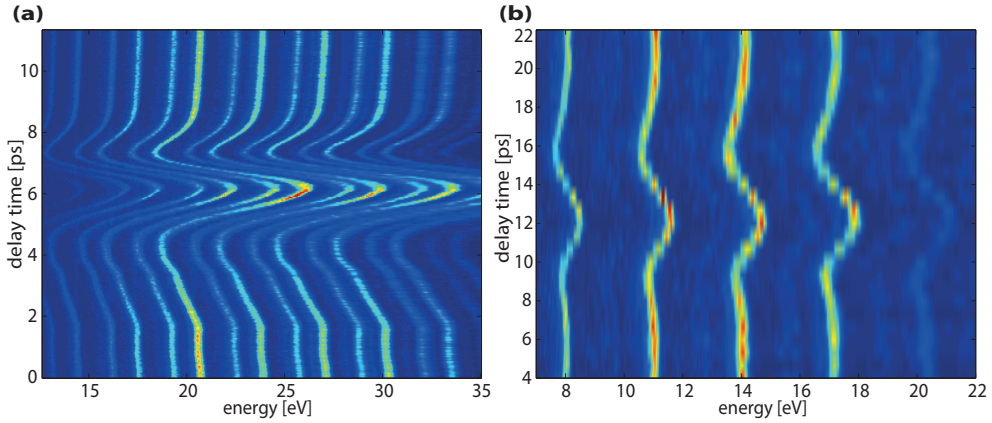


Figure 4.4: The change of the photoelectron spectra during the delay scan between the THz pulse and the HHG pulse. Subfigure (a) corresponds to the scan with Xe, while (b) shows the results for He gas.

that the kinetic energy shifts more for the more energetic electrons during the scan. This is caused by the fact that the absolute energy shift is dependent on the initial kinetic energy of the electron before the interaction with the THz field as shown in equation 1.40.

Performing a delay scan maps the shape of the THz vector potential and identifies the two linear parts on the rising and falling edges, where the measurements with the PALM are most accurate. By calculating the steepness of these linear slopes, the streaking strengths of the THz field was obtained in [eV/fs] units. After the shape of the THz pulse was defined, the delay stage was first positioned at two different points, where the HHG pulse arrives at the middle of the rising and falling edges of the THz, and where the electron spectra are streaked the most. At each of these positions 5000 consecutive streaked spectra were measured by the two eTOFs. Finally, the delay stage was moved to a third position that ensures that the THz and the HHG pulses completely miss each other temporally. At this position another 5000 non-streaked spectra were measured. The spectra from each position of the delay stage were averaged and compared to each other for the HHG pulse duration calculation. This procedure was repeated four times and the obtained pulse lengths from all four measurements were compared to

estimate the calculation precision.

As the signal with the Xe pulses is stronger compared to He, the pulse lengths were calculated using the measurements with xenon gas. The data analysis procedure performs a pulse length calculation for each individual spike of the photoelectron spectra. As already mentioned before, the spectrum from the Xe atoms contains 18 separate spikes corresponding to the 9 harmonics and two electron shells. During the streaking the electron spectra shift in energy, and some of the spikes leave the energy range over which the eTOFs are sensitive. It can be seen from figure 4.4 that, for instance, the spikes of energy 32.2 eV and 33.5 eV created by the 29th harmonic of HHG, are not in the measurement window during the whole scan, and the pulse length calculation using these spikes is not possible for the current setup of eTOFs. The data analysis procedure used 10 spikes for the pulse length calculations corresponding to the 5 harmonics from 19th to 27th. Following these 10 energy lines during the THz scan, the streaking strengths were calculated on both slopes for each eTOF.

The next step of the data processing is finding the rms widths of the spikes in the spectra. To evaluate the spectral widths of the non-streaked photoelectrons, the range of each individual spike was defined manually, and a Gaussian profile with a linear background was fitted to it. The fitting curve can be expressed in the following form:

$$y = a \exp \left[-\frac{(x - \mu)^2}{2\sigma^2} \right] + bx + c, \tag{4.1}$$

where the parameters μ and σ indicate the position and the rms width of the peak, respectively. Figure 4.5 shows 15 non-streaked spikes fitted to the profiles described by equation 4.1. The

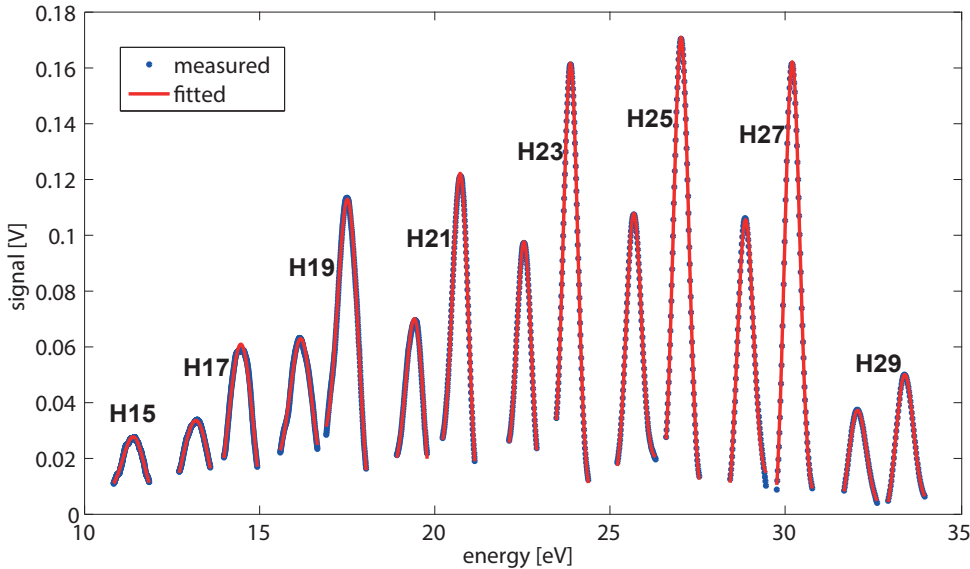


Figure 4.5: Gaussian profiles with linear background fitted to each spike of the measured spectra. The blue dots correspond to the measured points while the red lines show the fitted curves.

goodness of a fit is checked by comparing the standard deviation of the fit residuals to the rms

noise of the signal. When the ratio of these two quantities is below a certain threshold, the fit is considered good and it can correctly represent the shape of the spike. In case of the fits presented in figure 4.5 the ratio between the standard deviation of the residuals and the rms noise is about 5, which corresponds to a good fit as can be seen from the figure. The described fitting procedure was applied to all the spikes in the non-streaked spectra measured by the two eTOFs.

When the photoelectrons are streaked, the spectra experience broadening. This causes an overlap between the two neighboring spikes from the same harmonic separated only by 1.3 eV (difference between the binding energies of $5p_{1/2}$ and $5p_{3/2}$ shells). In this case it is preferable to choose a range containing the pair of the spikes and fit a double Gaussian profile to them. The fitted profile can be written as

$$y = a_1 \exp \left[-\frac{(x - \mu_1)^2}{2\sigma_1^2} \right] + a_2 \exp \left[-\frac{(x - \mu_2)^2}{2\sigma_2^2} \right] + b. \quad (4.2)$$

Using this expression, one can find the peak position and the rms width of both spikes from μ and σ variables, respectively. An example of a streaked double-peak spectrum is shown in figure 4.6. One can observe that unlike the non-streaked spectra shown in figure 4.5, the spikes in the streaked spectrum overlap, and the corresponding fits have larger uncertainties. The

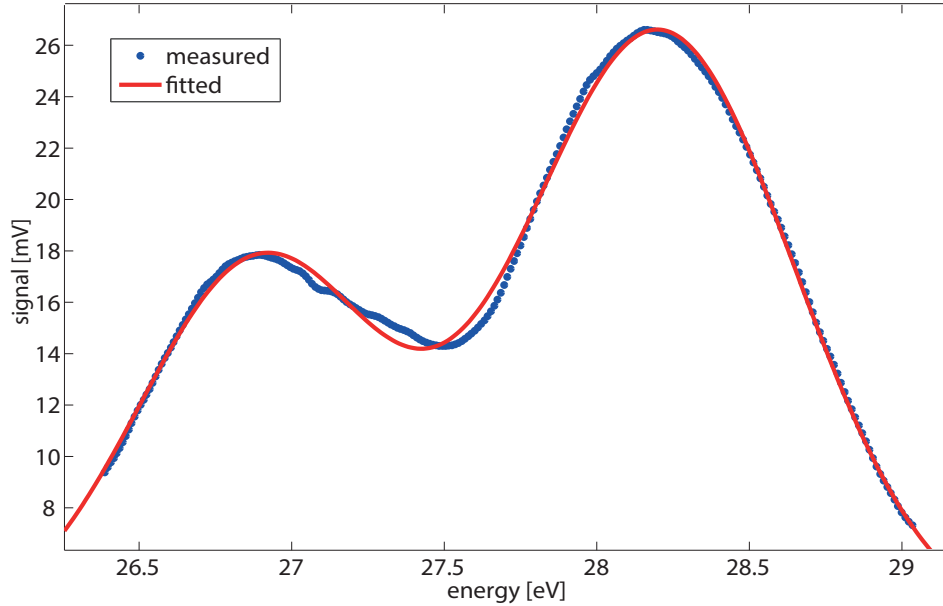


Figure 4.6: Spectrum from the two electron shells of Xe corresponding to the 27th harmonic of HHG, and a double Gaussian profile fitted to it. The blue dots correspond to the measured points while the red line shows the fitted curve.

analysis shows that the ratio between the standard deviation of the residuals and the rms noise of the signal is about 8 for the streaked spikes. Such a value indicates that the fits are still good enough to represent the shape of the spectra. However, using the spectral widths

obtained from the fits of streaked spectra induces larger uncertainties in the overall pulse length calculations compared to the non-streaked spectra.

The double Gaussian profiles were fitted to all spike pairs of the spectra streaked on the two slopes of the THz pulse. The comparison of the rms widths of the streaked and the non-streaked spectra allows to retrieve the length of the HHG pulses.

4.1.2 Results of the HHG measurements

The rms durations of the HHG pulses were calculated for 10 different energy peaks corresponding to 5 harmonics of the HHG spectrum. The calculation procedure was carried out for both slopes of the THz vector potential during each of the four different measurements. The obtained pulse lengths from separate measurements were averaged and the standard deviation of the values was calculated to estimate the measurement precision.

The results obtained from the measurements with the HHG beam are presented in table 4.1. Each row in the table corresponds to a single energy spike from the measured spectra defined by the harmonic number and the binding energy of the electron. The streaking strengths (slope

Table 4.1: The rms durations of the HHG pulses calculated using Xe for different harmonics with their standard deviations from 4 different calculations and the obtained linear chirps. The results are presented for the streaking at the two slopes of the THz pulse including also the corresponding streaking strengths.

Harmonic	e ⁻ shell	Slope 1			Slope 2		
		Slope [meV/fs]	Length [fs]	Chirp [meV/fs]	Slope [meV/fs]	Length [fs]	Chirp [meV/fs]
H27	5p _{3/2}	8.1	59±8	-0.2	13.0	37±3	-0.59
	5p _{1/2}	7.9	56±15	-0.24	12.4	46±12	-0.89
H25	5p _{3/2}	7.8	54±6	-0.53	12.2	39±2	-0.57
	5p _{1/2}	7.6	51±7	-0.1	11.8	51±3	0.05
H23	5p _{3/2}	7.1	49±4	-0.34	11.5	39±4	-0.79
	5p _{1/2}	6.6	45±7	-0.33	10.4	43±6	-2.0
H21	5p _{3/2}	6.5	49±10	-0.08	10.0	42±4	-0.33
	5p _{1/2}	6.0	48±13	-0.16	9.5	48±11	-2.0
H19	5p _{3/2}	5.4	50±11	-0.04	8.9	56±13	0.55
	5p _{1/2}	5.1	42±18	0.14	7.8	46±16	-0.54

steepness), the pulse lengths with the standard deviations and the chirps are presented for each slope of the THz. The pulse length values shown in the table are slightly larger compared

to the results reported in [68], owing to the fact that the measurements were performed at different days with different configurations of the HHG beam. The calculated chirp values are mostly negative as discussed also in [68] and are consistent with results reported in [110, 111]. Comparing the two columns corresponding to Slope 1 and Slope 2, one can immediately see that the second slope is steeper and the electrons on that slope are streaked more. This is the reason why the pulse lengths measured at different slopes have slightly different values. During the streaking, the effect of broadening of a peak was smaller than its overall shift in energy. This means that the separation of the two peaks corresponding to the same harmonic is bigger for a stronger streaking, and the individual peaks can be characterized better.

The comparison of the standard deviations of the pulse lengths for the two slopes shows that the spread is smaller in case of the stronger streaking. This is consistent with the fact that by applying a stronger electric field, it is possible to achieve a higher precision for the measurements. Table 4.1 shows that the smallest standard deviations for the pulse lengths are obtained from the harmonics H23 and H25, which have higher intensities compared to the other harmonics (figure 4.1), resulting in more ionized photoelectrons. The spectra comprising of more electrons experience less statistical fluctuations and their measurement is more reproducible. This effect is reflected also in the standard deviations from the two peaks of the same harmonic: the precision from the shell $5p_{3/2}$ is always higher than that from the shell $5p_{1/2}$ for every harmonic, as the measured signal is higher for the former compared to the latter (figure 4.5). Observing the slopes presented in the table shows that both slopes indicate a decrease in the streaking strength with decreasing order of harmonics, which correspond to lower initial energies of the photoelectrons. Such a result is predicted by the theory according to equation 1.40 stating that the energy shift of the photoelectrons depends on their initial energy before streaking.

It is also worth noting that the four different values obtained for each harmonic (two energy peaks at both slopes) are consistent and have an rms spread of sub-10 fs (about 6 fs on average). However, as mentioned above, the measurements performed at the second slope are more accurate as the energy peaks can be better characterized in this case. For this reason the final durations of the harmonics are calculated using the values obtained from the second slope. The results with the corresponding uncertainties are shown in figure 4.7. The length of each harmonic is obtained from averaging the two pulse lengths calculated for that harmonic from the electrons of the shells $5p_{3/2}$ and $5p_{1/2}$ streaked at the second slope. The averaging is performed using the weight of each value, calculated from its uncertainty shown in table 4.1. The resulting average lengths are in a range from about 38 fs to 52 fs. The vertical bars in figure 4.7 show the uncertainties of the average durations and are obtained from the individual uncertainties of the two averaged values. The largest uncertainty is about 10 fs obtained for the 19th harmonic corresponding to the smallest streaking strength. The uncertainties from the rest of the harmonics are less than 4 fs.

During the high harmonics generation process the creation of the higher harmonics requires higher intensities of the pumping IR laser, and they are generated only by the central part of the laser envelope. For this reason, the generation of the higher harmonics starts later than the lower harmonics and finishes earlier, resulting in shorter durations of the higher harmonics in

the temporal structure of the HHG pulse. The described trend is observable in figure 4.7 that shows shorter lengths for the higher harmonics. Meanwhile, one can see from table 4.1 that the results obtained for the first slope of the vector potential do not indicate this behavior. One can conclude from the results presented in table 4.1 and shown in figure 4.7 that the measurements performed with a stronger streaking field and with a larger amount of photoelectrons correspond to a better accuracy and precision. Such a conclusion is in accordance

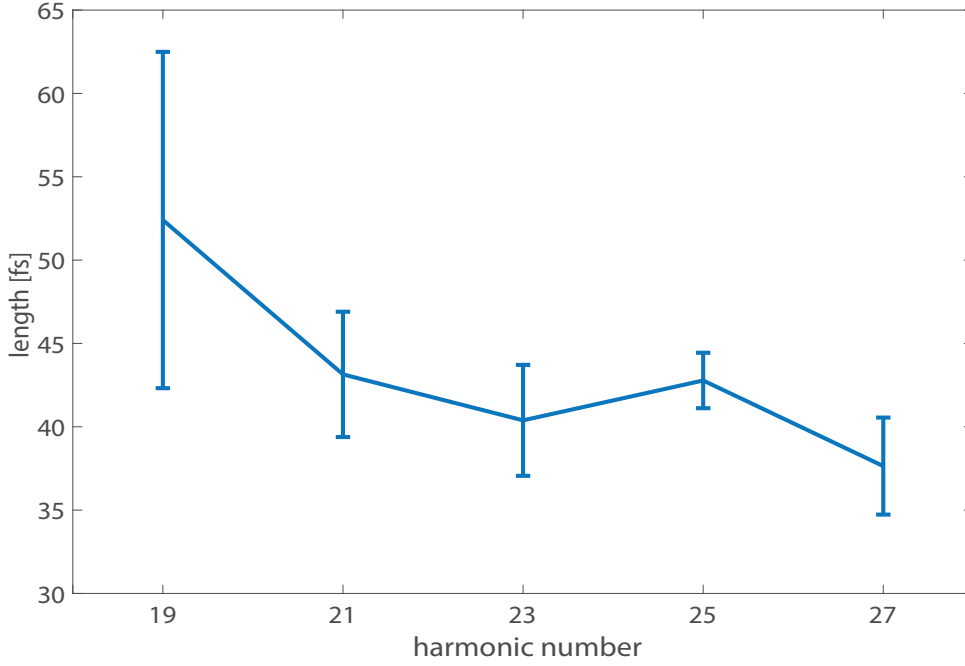


Figure 4.7: The durations of the five different harmonics calculated from the measurements at the second slope of the vector potential.

with the results obtained by the simulations in chapter 2.

The data measured during the delay scan between the THz pulse and the HHG pulse allow to reconstruct the shape and the strength of the electric field of the THz pulse. The reconstruction procedure is based on the derivations presented in section 1.3. It starts by writing the final kinetic energy of the electron in terms of the vector potential based on equation 1.38.

$$W_f = \frac{m_e v_f^2}{2} = \frac{m_e}{2} \left(v_0 + \frac{eA(t_i)}{m_e} \right)^2 = \frac{m_e v_0^2}{2} + v_0 eA(t_i) + \frac{e^2 A(t_i)^2}{2m_e}. \quad (4.3)$$

Here $A(t_i)$ is the vector potential of the THz pulse at the moment of ionization t_i . Assuming that the electron velocity change due to the interaction with the THz field is smaller than its initial velocity $eA/m_e \ll v_0$, which is the case for the HHG measurements, the third term on the right side of 4.3 can be neglected. In this case the expression can be rewritten in terms of

the initial kinetic energy and the vector potential:

$$W_f = W_0 + A(t_i) \sqrt{\frac{2W_0 e^2}{m_e}}. \quad (4.4)$$

During the THz scan the final kinetic energy W_f was measured by the eTOFs for each delay position corresponding to different values of t_i . From the measured data the vector potential along the whole THz pulse can be calculated as

$$A(t_i) = (W_f - W_0) \sqrt{\frac{m_e}{2W_0 e^2}}. \quad (4.5)$$

After obtaining the vector potential of the THz pulse, its temporal derivative should be calculated $E(t) = -\partial A(t)/\partial t$, to get the electric field strength. Figure 4.8 shows the electric field reconstructed by the described procedure from the measurements of the two eTOFs. One can see from the figure that the field reconstructed from eTOF1 (blue curve in the figure) is mainly negative meaning that the electrons measured by eTOF1 were propagating in the direction of the field. Meanwhile, eTOF2 was registering the electrons drifting opposite to the

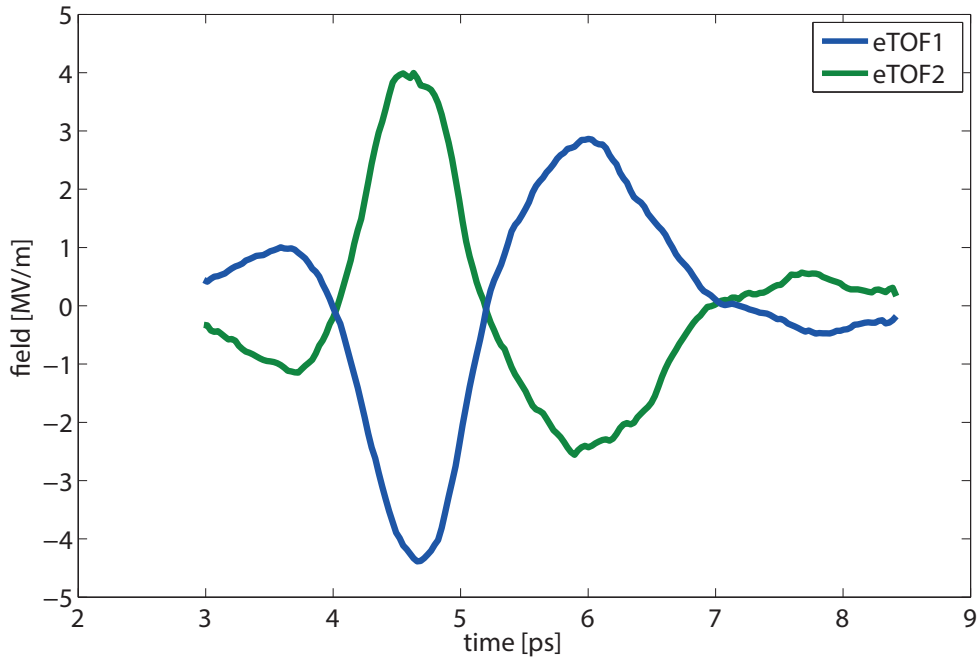


Figure 4.8: Electric field of the THz pulse calculated from the measurements. The blue line corresponds to the measurements from eTOF1, while the green line shows the field obtained from eTOF2.

streaking field. The peak electric field strength reconstructed from the PALM measurements was about 4.5 MV/m. This value is consistent with the values obtained by the field strength measurements using the electro-optical sampling method [54, 112].

Apart from the measurements discussed above, a separate set of measurements was performed

to estimate the accuracy of the peak width measurements for the two eTOFs from the non-streaked spectra. For this purpose 5000 consecutive spectra were measured by both eTOFs while the THz beam was blocked and the HHG beam was unchanged. From the measured 5000 spectra 5 sets of 1000 spectra were chosen and averaged. The rms widths of all peaks in the spectrum were calculated for all 5 average spectra. Standard deviation from the obtained 5 spectral widths for each peak was calculated. The residuals of the Gaussian fits in this case were small and the contribution of the fitting errors in overall uncertainties were minimized. This resulted in the uncertainties mainly dominated by the statistical fluctuations of the spectra measured by the eTOFs. In order to estimate the uncertainties in the spectrum obtained from averaging of 5000 consecutive measured spectra, the standard deviations obtained from averaging 1000 spectra were divided by $\sqrt{5}$ due to $1/\sqrt{N}$ dependence of the standard deviation on the size of the population. This results in relative uncertainties for the spectral width calculations of about 1.5%. This value was used for the uncertainty estimation for all the spectral widths calculated during the measurements of the streaked and non-streaked spectra. To estimate the resulting uncertainty of the pulse duration, the uncertainties of all spectral widths were propagated through the following expression for the pulse length:

$$\tau_X = \sqrt{\frac{\sigma_{st,1}^2 - \sigma_{0,1}^2 + \sigma_{st,2}^2 - \sigma_{0,2}^2}{2s^2}} \quad (4.6)$$

The results showed that the contribution of the uncertainties from the eTOF measurements and statistical fluctuations of the spectra were about a femtosecond or less for all the peaks. This means that the standard deviations presented in table 4.1 are caused mainly by the fits of the streaked spectra and possible variations of the HHG or THz beams between different measurements. As already mentioned, during the streaking the two peaks from a single harmonic are broadened and merge together making the fitting process more challenging. The first measurements performed by the prototype PALM setup at the HHG source proved the capability of the device to measure the temporal duration of the photon pulses using the streaking concept. The obtained values for the pulse duration and the linear energy chirp were consistent with the expected values and showed a good agreement with the simulation results discussed in chapter 2. From 4 different measurements the standard deviation of pulse lengths calculated for all energy peaks at both slopes was about 7 fs on average, ranging from 18 fs down to 2 fs. The electric field strength of the THz pulse was reconstructed from the delay scan measurements, and the obtained value was consistent with the measurements using electro-optical sampling. During the first measurements with the prototype setup the functionality of all the components in the system was tested. After the successful measurements with the HHG source, the setup was tested at SACLA - a hard X-ray FEL source in Japan.

4.2 First measurements of hard X-ray FEL pulses at SACLA

The measurements with hard X-ray FEL pulses were performed at SACLA during 7 consecutive shifts of 12 hours. The beam time was in February of 2014 with the proposal num-

ber 2013B8002. During the measurements the durations and the relative arrival times of FEL pulses were measured for the first time in the hard X-ray region using the THz streaking method. Some results from the relative arrival time measurements of the FEL pulses are presented in [78].

4.2.1 Procedure of FEL pulse measurement and data processing

The measurements were performed in the experimental hutch 3 (EH3) of the beamline 3 (BL3) at SACLA [95]. The prototype PALM setup was attached to the BL3, and the FEL beam was directed to the interaction point. The description of the experimental setup used during the measurements is provided in section 3.1. The FEL beam transverse diameter was in range from 100 μm to 200 μm , while the FEL pulse energy was between 150 μJ and 250 μJ during the measurements. The repetition rate of the FEL pulses was 30 Hz. The experimental laser of SACLA was used for the THz generation setup of PALM. It is a Ti:sapphire laser of 800 nm wavelength, with a pulse energy of about 7 mJ and rms duration of 25 fs. The generated THz pulse was intrinsically synchronized with the experimental laser of SACLA, meaning that measuring the FEL temporal jitter relative to the THz beam gives the jitter relative to the IR beam as well.

A trigger synchronized both with the FEL beam and the experimental laser was sent to the gas valve controller. The backing pressure behind the valve was about 3.5 bar above the atmospheric. The temporal overlap between the FEL pulses and the gas jet was found by scanning the delay of the trigger relative to the FEL arrival. After the overlap was found and the photoelectron spectra were registered by the eTOFs, the signal was optimized by changing the position of the gas jet in the horizontal plane, along the transverse direction of the FEL beam. The temporal overlap between the THz and the FEL pulses was found in several steps. First, a coarse overlap was found between the two pulses using an intermediate IR laser beam. The IR beam was first synchronized with the FEL beam using a GaAs photodiode and then synchronized with the THz beam using an electro-optical ZnTe crystal. After the overlap region of several picoseconds was found, a finer delay scan was performed by changing the arrival time of the THz pulse with respect to the FEL pulse using a linear delay stage. The overlap of the two pulses is found when the eTOFs register an energy shift in the spectra of the photoelectrons.

During the measurements the photon energy of the FEL pulses was changed from 5000 eV to 10000 eV with steps of 1000 eV. The energy bandwidth of the photon beam was in range of 0.1-0.3% rms. After the measurements at the mentioned photon energies were completed, a double-crystal monochromator (DCM) with Si (111), available at SACLA beamline [113], was used to carry out measurements with photon energies from 6000 eV up to 9000 eV with 1000 eV steps. The function of the DCM is to reduce the energy spread of the FEL spectrum down to 0.01%. The DCM, however, also reduces the intensity of the FEL beam by a factor of about 50 as it cuts out all the photons with energies outside of the specified bandwidth. During the measurements the atoms of Xe gas were ionized. In case of 5000 eV photon energy the electrons from $3d_{5/2}$ shell with a binding energy of 676.4 eV were measured, while for all

the other photon energies the electrons from $2p_{3/2}$ shell with a binding energy of 4786 eV were used.

A sequence of measurements was performed for each photon energy of the FEL beam, for both monochromatic and non-monochromatic (pink) beams. The first measurements were performed to calibrate the eTOF spectrometers, which were followed by a delay scan between the THz and the FEL pulses. After the scan was finished, the arrival of the FEL pulses was set to the linear part of the THz vector potential and about 10000 streaked spectra were measured. In addition to these spectra, another 10000 non-streaked spectra were measured while the THz beam was blocked.

The photoelectrons ionized by the hard X-ray photons had kinetic energies of thousands of electronvolts. In order to measure these electrons with a high accuracy, an electrostatic retardation and lensing was applied in the eTOFs. By applying a retarding voltage in the drift tube of the eTOFs, the kinetic energies of the photoelectrons of interest were reduced down to few hundreds of electronvolts. The drift tube voltages were set to such values that the chosen energy peak was in the center of the energy window measured by the eTOFs and it was well separated from the neighboring peaks. In addition to the retardation, electrostatic lensing was also applied in the eTOFs to maximize the number of electrons reaching the MCPs.

For the energy range where the eTOFs were most sensitive for the selected peak, there were no other peaks that could be measured accurately. For this reason it was not possible to calibrate the eTOFs by measuring the temporal positions of several peaks in the signal and referring them to certain photoelectron energies, as it was done in case of the measurements with the HHG beam. Instead, the calibration procedure was carried out by scanning the retarding drift tube voltage of the eTOFs and measuring the peak position in time for each value of the voltage. For each photon energy the drift tube voltage was changed around the nominal value by about 500 V in both directions in steps of 50 V. At each step about 250 waveforms were measured by the eTOFs. Figure 4.9 shows the evolution of the energy spectra measured by eTOF1 during the drift tube voltage scan for 9000 eV photon energy. Each waveform shown in the figure is an average of about 250 spectra. The first peaks in the spectra labeled as #0 correspond to the valence electrons from the outer shells that have kinetic energies of several thousands of electronvolts, which is outside the energy range where the eTOFs are sensitive. For this reason the signals from all these electrons are stacked together in a single peak by the eTOFs, and separate energy lines cannot be resolved. The peaks labeled as #1 in the figure correspond to the electrons from the shell $2p_{3/2}$ that were used during the measurements with a photon energy of 9000 eV. The peaks #2 and #3 correspond to the electrons from the shells $2p_{1/2}$ and $2s$, respectively. The electrons from these shells have smaller kinetic energies, and the corresponding peaks disappear after the drift tube voltages are higher than certain values. Another small peak is observed in the eTOF signal that corresponds to the photons scattered from the interaction region and registered by the MCPs. This peak shows the time of flight of the photons through the eTOF and it does not change its position when the eTOF settings are modified. For this reason each of the measured waveforms is shifted in time such that the photon peak is in the origin of the time axis, and the time coordinate of the peak of interest is obtained relative to the photon peak. This procedure ensures that the flight times of the

4.2. First measurements of hard X-ray FEL pulses at SACLA

electrons with different retardations are always calculated with respect to the same point in time that remains constant throughout the scan.

One can see from figure 4.9 that the peak #1 moves towards longer flight times when stronger retardations are applied. It is following the inverse quadratic dependence that defines the calibration constants in accordance with equation 3.3. For each position of the peak in time,

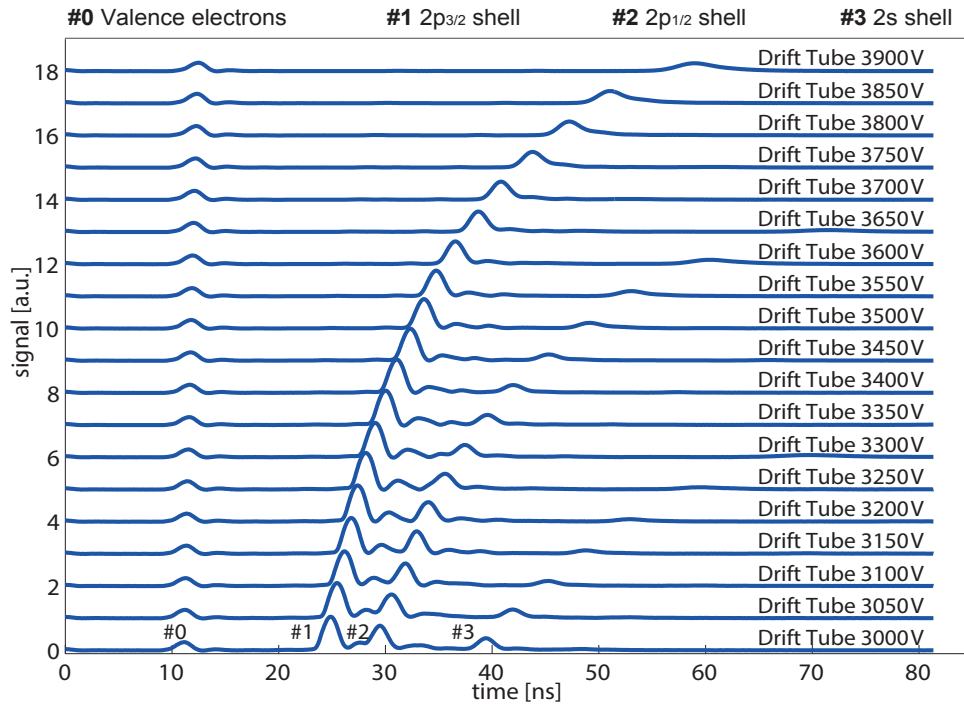


Figure 4.9: The change of the flight time of the electrons measured by eTOF1 during the calibration scan for the photon energy of 9000 eV. Each waveform in the figure corresponds to the value of the retarding voltage indicated on the right part of the figure.

the corresponding electron energy is calculated by subtracting the values of the binding energy of the $2p_{3/2}$ shell and the drift tube voltage from the photon energy of the FEL pulse. The resulting value corresponds to the kinetic energy of the electron at the end of the drift tube when it is registered by the MCP. By combining the energy values corresponding to different drift tube voltages with the peak positions in time, the calibration constants can be found.

The calibration procedure was carried out for each photon energy with a pink beam and a monochromatic beam. Whenever certain settings of the eTOFs were changed, the spectrometers were recalibrated. The calibration curves and the corresponding constants for the two eTOFs are shown in figure 4.10 for the photon energy of 5000 eV. The results shown in figure 4.10 are similar to those presented in figure 4.3 obtained for the HHG beam.

After the calibration coefficients were obtained, the arrival time of the THz pulse relative to the FEL pulse was scanned to retrieve the shape of the vector potential of the THz pulse. The arrival time of the THz pulse was changed by changing the position of an optical component in the THz generation setup by a linear stage. Unlike the measurements with the HHG beam, during the measurements at SACLA the external experimental laser (therefore also the THz

Chapter 4. Measurements

beam) and the FEL beam had an intrinsic temporal jitter. This means that even when the position of the delay stage was unchanged, the FEL pulses were still arriving at different parts of the THz pulse, and the relative arrival time of the two pulses was constant only on average. The position of the delay stage was changed in steps of $3 \mu\text{m}$ corresponding to 20 fs delay. For

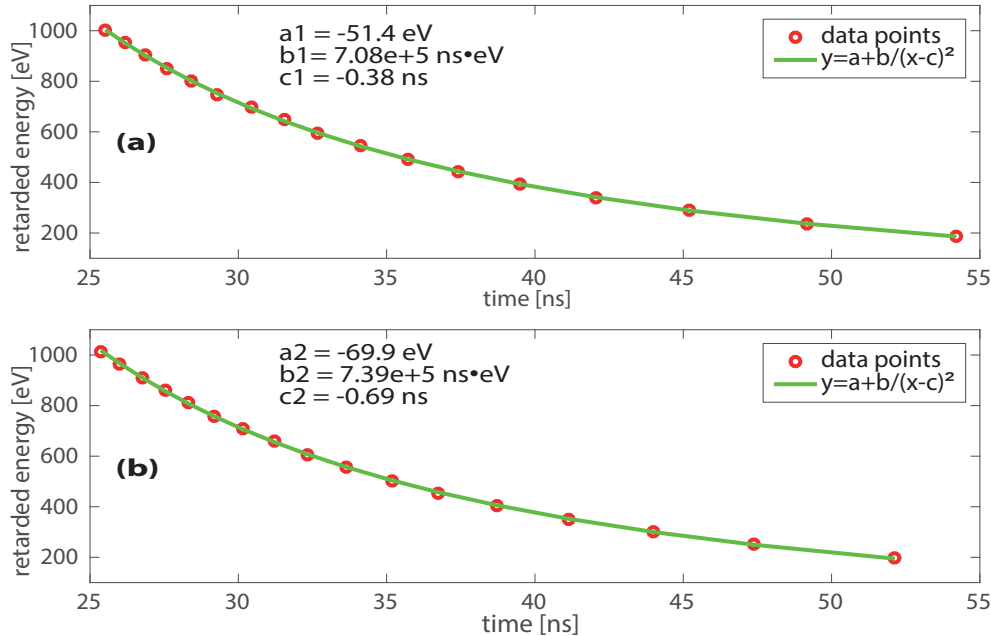


Figure 4.10: Calibration curves of eTOF1 (a) and eTOF2 (b) from the measurements with a photon energy of 5000 eV. The red circles correspond to the data points and the green lines show the fitted curves.

each position of the delay stage, 100 consecutive spectra were measured. Figure 4.11 shows the results from the delay scans with and without the monochromator at 9000 eV photon energy. For each delay time value an average of 100 spectra is plotted. The figure shows the shift of the energy spectra due to the interaction of the electrons with the THz field. The shifts are in opposite directions for the two eTOFs as they measure the electrons moving along the streaking field and opposite to it. The photoelectron spectra are shifted by about 100 eV, which is much higher compared to the shift of several electronvolts in case of the measurements with the HHG beam (figure 4.4). This is caused by the fact that the energy shift due to the interaction is dependent on the initial kinetic energies of the electrons, and in case of the hard X-ray FEL pulses the ionized electrons have energies of thousands of electronvolts. Comparing the two parts of the figure corresponding to the pink beam (left in the figure) and the monochromatized beam (right in the figure), one can see that, as expected, there is no photon energy jitter in case of the beam with the DCM, and the spectra are narrower and more stable compared to the spectra from the pink beam. At the same time, the signal in case of the pink beam is much higher and the uncertainties caused by the statistical fluctuations of the spectra are smaller in this case. Figure 4.11 also shows that the spectra of the electrons jitter more on the slopes of the THz pulse as their energy in this case is affected also by the

4.2. First measurements of hard X-ray FEL pulses at SACLA

temporal jitter between the FEL and the THz pulses.

The amount of energy shift caused by the streaking effect is somewhat underestimated due to the arrival time jitter. Even when the delay stage is positioned such that the average arrival time of the FEL pulses is at the peak of the vector potential, not all of the photon pulses arrive exactly at the peak because of the temporal jitter. This means that some of the photoelectrons

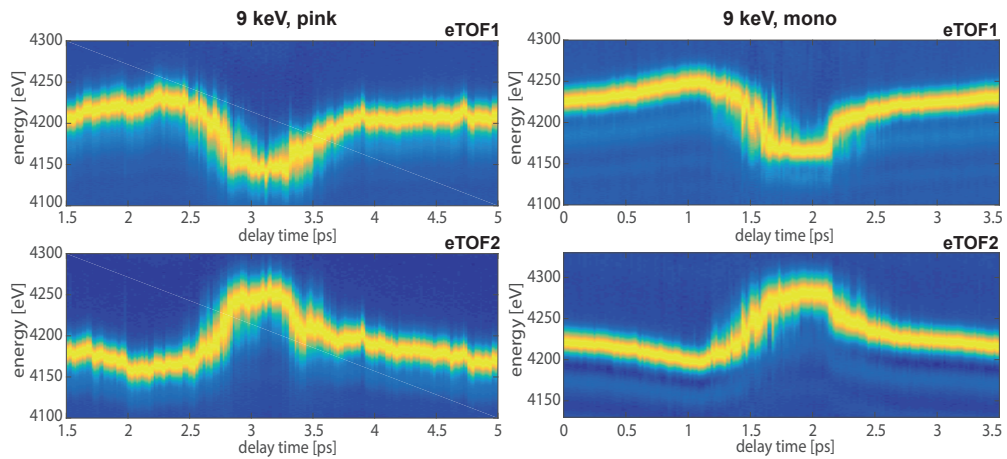


Figure 4.11: Normalized spectra of the photoelectrons from the two eTOFs during the delay scan at 9000 eV photon energy. The subfigures on the left correspond to the pink beam, while the ones on the right correspond to the beam with the monochromator.

are ionized away from the peak of the THz pulse, and their kinetic energies are shifted less. Even though the distribution of the FEL arrival times is symmetric and is centered at the peak of the THz pulse, the distribution of the corresponding energy shifts of the photoelectrons is not symmetric and is not centered around the value corresponding to the peak vector potential of the THz. Figure 4.12 shows the distribution of the electron kinetic energy shifts at different parts of the THz pulse. The subfigure on the left (a) shows the distribution of the energy shifts at the minimum of the THz pulse. One can see that the distribution is not symmetric, and only the smallest values (showing the largest absolute shift) correspond to the arrival of the FEL pulses at the minimum of the THz, while the rest of the energy shift values correspond to the FEL pulses arriving before or after the minimum. The same effect can be seen in the third histogram (c) corresponding to the average arrival of the FEL at the maximum of the THz pulse. The values corresponding to the largest energy shift represent the maximum vector potential better than the average value of the distribution. At the same time, the subfigure in the middle (b) corresponds to the arrival of the FEL pulses at the linear part of the THz pulse and shows a symmetric distribution of the energy shifts. In this case the FEL pulses arriving later (earlier) than the average point correspond to a larger (smaller) energy shift of the photoelectrons, and the average energy shift corresponds to the average arrival time. The effect of the underestimation of the energy shift can be observed also in figure 4.11, where the mapped vector potential has a flat-top shape. The reconstruction of the vector potential is done by taking the average energy shift from the 100 measurements at each delay position between the FEL and the THz pulses. However, when the FEL pulses

arrive around the extrema of the THz vector potential, the distribution of the energy shifts due to the streaking is no longer symmetric as already shown in figure 4.12, and a correction needs to be applied to find the true values of the extrema. For this purpose the distribution of all energy shift values was studied around the peaks of the THz pulse. The small values of

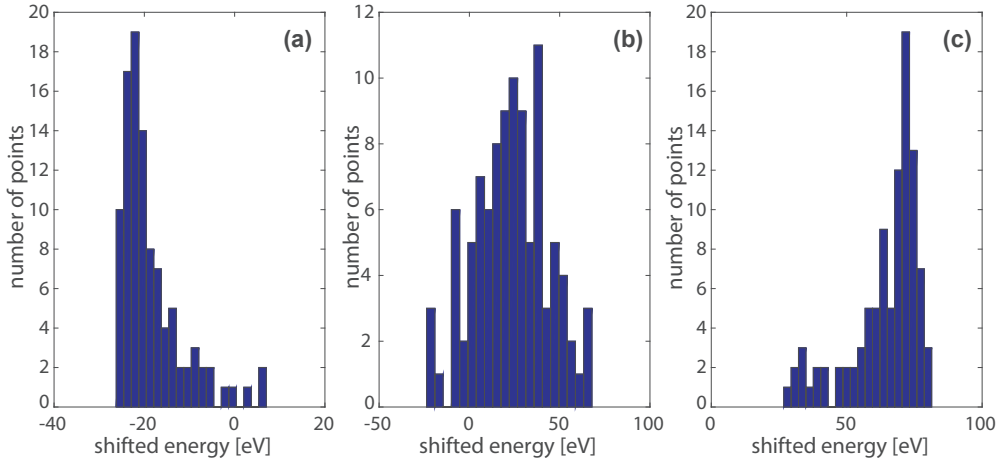


Figure 4.12: Distributions of the shifted energy peak positions at the minimum (a), linear part (b) and the maximum (c) of the vector potential. The histograms correspond to the measurements with a photon energy of 10000 eV.

the absolute shift in energy that correspond to the FEL pulses arriving away from the THz peaks were omitted in the calculation, and only the average of the largest 10 values was used to estimate the true values of the vector potential extrema.

The asymmetry of the shifted energy values is present not only at the exact extrema of the vector potential but also in their proximity, and it decreases towards the central part of the linear area. For this reason the corrections were applied only at the delay positions close to the peaks of the THz pulse. The amount of the correction becomes smaller when moving away from the extrema and it disappears at the central area of the slope. Figure 4.13 shows the effect of the correction applied on the linear part of the vector potential. One can see from the figure that the corrected slope follows closely the values of the biggest absolute energy shifts in the vicinity of the extrema of the vector potential, while at the linear part it is only defined by the average values of the whole distribution of the energy shifts.

Applying the described correction to the vector potential is important not only for the reconstruction of the THz field but also for the calculation of the streaking strength of the THz pulse. As one can see from figure 4.13 the linear area of the corrected slope is steeper around the center, where the pulse lengths are calculated, and estimating correctly the streaking strength at the linear part of the THz pulse directly affects the FEL pulse length calculation accuracy. Apart from the temporal jitter between the FEL and the THz pulses, the average relative arrival time of the two pulses was also drifting in the process of the delay scans. Because of this effect the average values of the energy shifts experience small jumps at certain points of the delay. These jumps can be observed in the measured slope presented in figure 4.13. During the measurements it was not possible to monitor these temporal drifts between the two pulses,

and the analysis procedure could not correct for this effect.

After the delay scan was performed, another set of measurements was taken to obtain the rms lengths and the relative arrival times of the FEL pulses. The delay stage was moved to a position corresponding to the average arrival of the FEL pulse at the center of the linear part of the THz vector potential, and photoelectron spectra were measured for about 10000 consecutive FEL pulses. After these spectra were recorded by the eTOFs, the laser shutter was

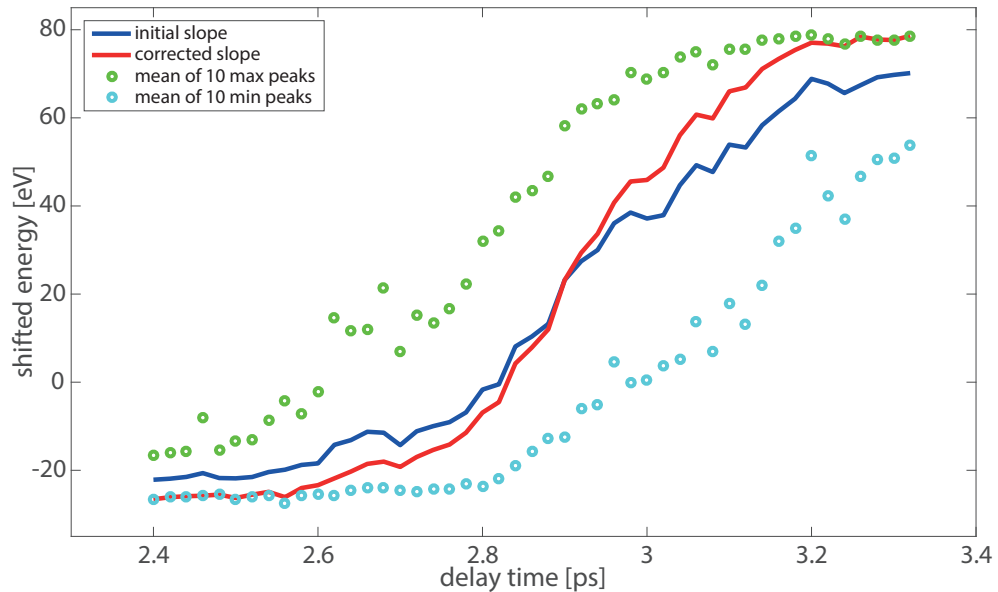


Figure 4.13: Linear area of the THz vector potential before the correction shown in blue and after the correction shown in red. The green and the cyan circles show the average values of the 10 largest absolute energy shifts, respectively, in direction of the THz field and opposite to it.

closed to block the IR laser beam feeding the THz generation setup. This ensures that no THz beam is generated and the photoelectrons ionized by the FEL pulses are not streaked. While the shutter was closed, about 10000 non-streaked spectra were measured by the eTOFs.

During the streaking measurements the power of the experimental laser used for the THz generation was monitored on a single shot basis. The relative fluctuations of the laser power were about 5-6%. Assuming that in the small range of the laser power jitter the generated THz beam power is linearly dependent on the pumping laser power, the relative jitter of the streaking THz field was calculated. This was used to apply a correction to the energy values of the streaked photoelectrons for each FEL pulse.

The calculation of the pulse durations and relative arrival times commences with the analysis of the spectra measured by the eTOFs. After the calibration is done and the photoelectron energy spectra are obtained, the spectral widths and the central energies of the spectra are found by fitting Gaussian profiles to the energy peaks. Apart from the peaks corresponding to the photoelectrons from the shell being studied, the spectra provided by the eTOFs include also other peaks (corresponding to the valence electrons, Auger electrons, scattered photons

etc.). Therefore, the first thing to be done in the analysis is to manually define an approximate range where the peak should be searched. When the range of interest is defined, the position of the maximum in this range is found. Depending on the width of the peak, a more precise area is chosen around the maximum position, where the fitting should be performed. The fitting range is defined such that it includes the whole peak but also excludes all the features that are not related to the peak and have different origin. Figure 4.14 shows two different peaks corresponding to the streaked and the non-streaked spectra of the photoelectrons and the Gaussian fits applied to them. One can see from the figure that the streaked spectrum is

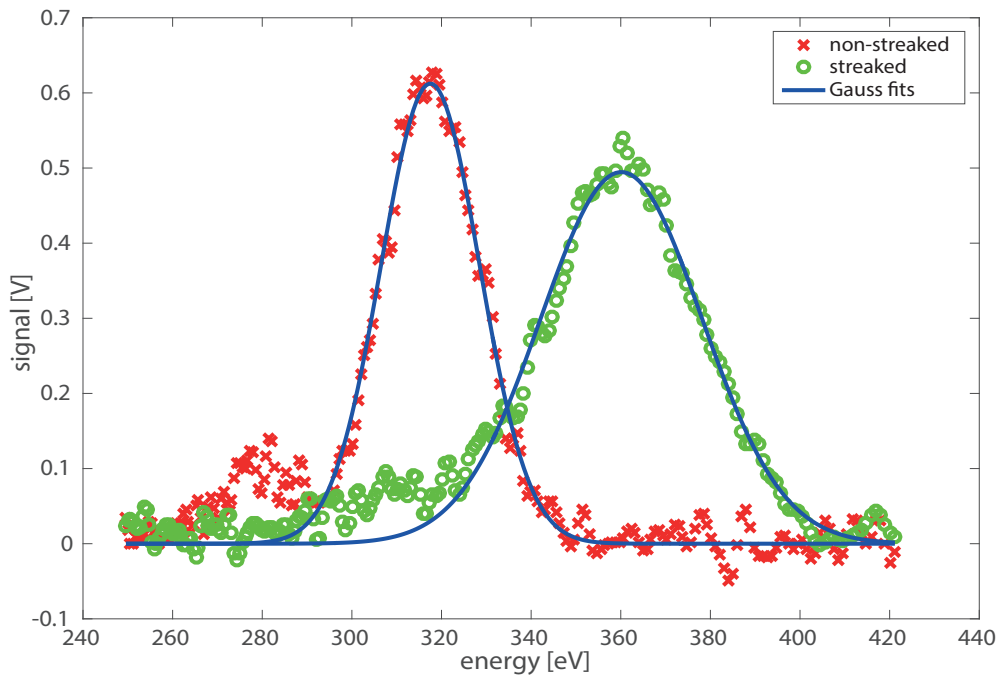


Figure 4.14: Gaussian fits (blue curves) applied to a streaked (green circles) and a non-streaked (red crosses) photoelectron spectra.

broader as should be expected. The fitting procedure is performed using the non-linear least square algorithm [114]. After a Gaussian profile is fitted to the peak, the goodness of the fit is checked in order to decide if the particular peak should be included in the statistics of the analysis. The main criteria of the goodness of a fit is the comparison of the fit residuals to the rms noise of the signal. Similar to the analysis of the HHG measurements, the fit is considered good if the standard deviation of the residuals is up to 10 times larger than the rms noise of the signal from the eTOFs. Using this criteria filters out about 5-20% of the measured data. From the remaining spectra only those that correspond to the FEL arrival at the linear part of the THz vector potential were used for the pulse length and the arrival time retrieval.

The relative arrival time of the FEL pulses was obtained by calculating the energy shift of the photoelectrons due to the interaction with the THz field and mapping these values on the linear area of the vector potential similar to the red curve shown in figure 4.13. The area of the vector potential was chosen such that it can be described by a monotonic function, and a

4.2. First measurements of hard X-ray FEL pulses at SACLA

one-to-one conversion is possible from the shifted energy values to the arrival time values. The two eTOFs measure the electrons that experience energy shifts in the opposite directions. Therefore, to find the absolute energy shift with respect to the initial kinetic energy, the shifted energies measured by the two eTOFs are subtracted from each other, and this difference is divided by 2. As both spectrometers measure the spectra from the same FEL pulse, using the difference of their signals allows to eliminate the shot-by-shot photon energy jitter of the FEL pulses.

The calculation of rms length of the FEL pulse requires the streaked and non-streaked photoelectron spectra created by the same pulse. For the prototype PALM setup the simultaneous measurement of these two spectra was not possible, and the streaked and non-streaked spectra were measured separately corresponding to different FEL pulses. Unlike the HHG pulses, the FEL pulses fluctuate significantly from shot to shot, and estimating the pulse length by comparing the streaked and non-streaked spectra from different photon pulses (as it was done for the HHG beam) would be inaccurate.

To estimate the width of a non-streaked spectrum corresponding to the measured streaked spectrum, the analysis procedure uses the dependence of the spectral width on the central energy of the spectrum observed during the calibration process. This dependence is caused by the fact that the electrons with different energies are focused differently by the electrostatic lensing applied in the eTOFs. Because of the different focusing, the corresponding spectral widths measured by the eTOFs are different. After carefully studying the change of the spectral widths for different retarded energies, it was found that the dependence is best described by a 3rd order polynomial. The measured widths for different retarded energies of the photoelectrons and the corresponding polynomial fits are shown in figure 4.15 for both eTOFs. With help of these calibration curves shown in the figure, the rms spectral width can be estimated by knowing the central energy of the retarded electrons for each eTOF. The parameters of the 3rd order polynomial curves fitted to the measured data were calculated for all the measurements with different photon beams and were used for the pulse length calculations. After measuring about 10000 spectra of the photoelectrons streaked at the linear part of the vector potential, their central energies were found. These values were mapped on the 3rd order polynomial curves shown in figure 4.15, and the corresponding non-streaked spectral widths were reconstructed.

To validate this method of retrieving the rms widths of the non-streaked spectra, the same procedure was applied to the 10000 spectra measured without the THz beam. In this case the rms widths reconstructed from the 3rd order polynomial curves should be the same as the widths calculated directly from the measured spectra, as no broadening of the spectra takes place due to the streaking. The rms difference between these two quantities for about 10000 spectra was less than an electronvolt and was within the average uncertainty of the spectral width measurements by the eTOFs. After the method was validated, the FEL pulse lengths were calculated using the measured streaked spectral widths and the reconstructed non-streaked spectral widths. This reconstruction process was absent in the analysis of the measurements with the second generation PALM, as in this case both the streaked and the non-streaked spectra were simultaneously measured for the same FEL pulse.

Chapter 4. Measurements

The analysis procedure used only those photoelectron spectra that correspond to the FEL arrival at the steepest part of the THz linear slope, where the spectra are streaked the most, and the pulse lengths can be calculated with the highest accuracy.

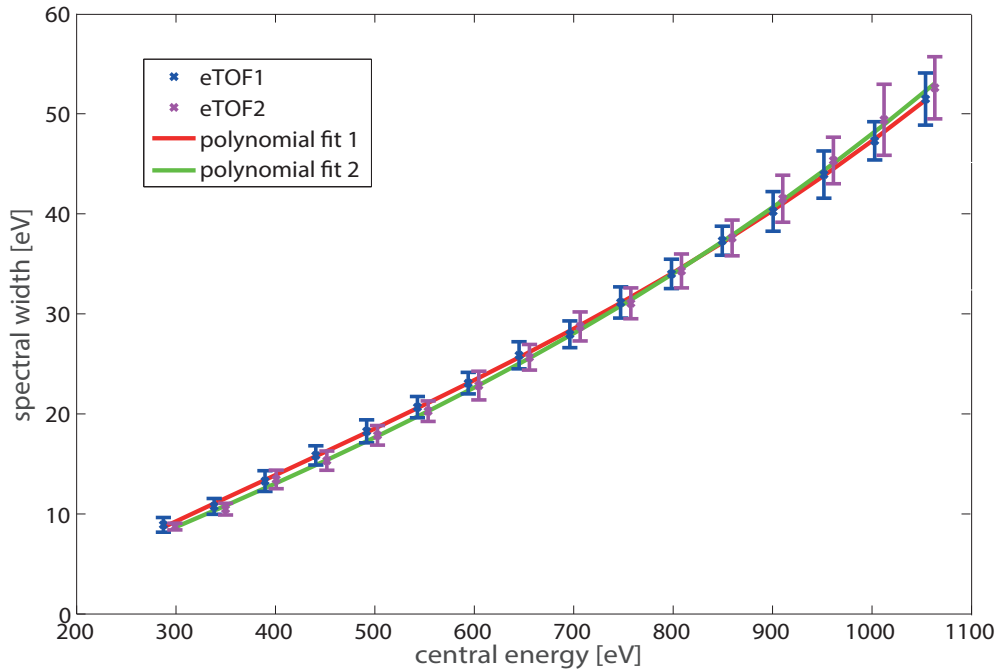


Figure 4.15: The dependence of the rms widths of the spectra on the central energies for the two eTOFs and the corresponding 3rd order polynomial fits. The plots correspond to the calibration measurements with the 9000 eV photon beam with the monochromator. The vertical bars correspond to the standard deviation from 100 measurements.

4.2.2 Results from the first FEL measurements

The rms durations and the relative arrival times of the hard X-ray FEL pulses were calculated using the analysis procedure described above for all 10 different configurations of the photon beam.

The results obtained from the arrival time measurements for different FEL beams are presented in table 4.2. The table shows the rms jitter of the arrival time measured for different photon beams, as well as the corresponding streaking strengths and the estimated measurement accuracies. The rms jitter was calculated from the measurements of about 6600 pulses on average, arriving at the linear part of the THz vector potential and being measured with the highest accuracy. The obtained values for the rms jitter vary from 84 fs up to 153 fs and have an average value of about 115 fs. These values are consistent with the specifications of SACLA and show a good agreement with the expected rms jitter. The average streaking strengths presented in table 4.2 for different photon energies vary from about 0.12 eV/fs up to 0.32 eV/fs, with stronger streaking values corresponding to the electrons with higher initial

4.2. First measurements of hard X-ray FEL pulses at SACLA

kinetic energies as expected from theory.

The accuracies of the measurements were calculated by evaluating the energy measurement accuracies of the two eTOFs. This was done by measuring the central energies from several thousands of spectra without the THz beam with both eTOFs. When the THz beam is blocked,

Table 4.2: The rms jitter of the FEL pulses relative to the THz pulses for different photon beams. The terms ‘pink’ and ‘mono’ correspond to the beam without the monochromator and with it, respectively.

Photon beam	Streaking strength [eV/fs]	Arr. time jitter [fs]	Accuracy [fs]
10 keV, pink	0.32	84	4.3
9 keV, pink	0.27	153	4.2
8 keV, pink	0.21	146	5.0
7 keV, pink	0.13	123	5.4
6 keV, pink	0.12	92	7.2
5 keV, pink	0.2	109	7.1
9 keV, mono	0.2	103	14.1
8 keV, mono	0.25	86	7.7
7 keV, mono	0.14	119	11.0
6 keV, mono	0.13	125	9.0

both eTOFs measure the same electron spectra, and the central energies of the measured spectra should be the same within the accuracies of the eTOFs. Therefore, the average accuracy of a single eTOF was found by calculating the rms difference of the energy values measured by the two eTOFs and dividing it by square root of two: $\sigma_{eTOF} = \sigma_{(eTOF1-eTOF2)}/\sqrt{2}$. This results in an average accuracy of about 1 eV for each eTOF. The accuracy of the arrival time measurement was calculated using the corresponding streaking strength for each photon energy.

As already mentioned in this section, the presence of the DCM monochromator reduces the FEL beam intensity by a factor of about 50. This results in a smaller amount of the photoelectrons detected by the eTOFs and, therefore, larger statistical fluctuations. This explains the results in table 4.2 showing that the accuracies from the monochromatic beam are worse than for the pink beam.

Four different distributions of the single-shot arrival time measurements with different photon beams are shown in figure 4.16. The rms jitter of the arrival times presented in table 4.2 are calculated from these distributions. One can see from figure 4.16 that the distributions of the arrival times are symmetric. As it was previously shown in figure 4.12b, this corresponds to the measurements at the central part of the linear slope of the vector potential. Therefore, one can

Chapter 4. Measurements

conclude that the arrival times are measured with the highest possible accuracies presented in table 4.2.

The results obtained from the arrival time measurements show that the PALM setup is capable of measuring the arrival time of hard X-ray FEL pulses with a sub-10 fs accuracy.

The results from the FEL pulse length calculations are shown in table 4.3. The streaking strengths shown in the table are the same as previously shown in table 4.2 for the arrival time measurements. Average values of the pulse lengths are presented in the 'FEL length' column

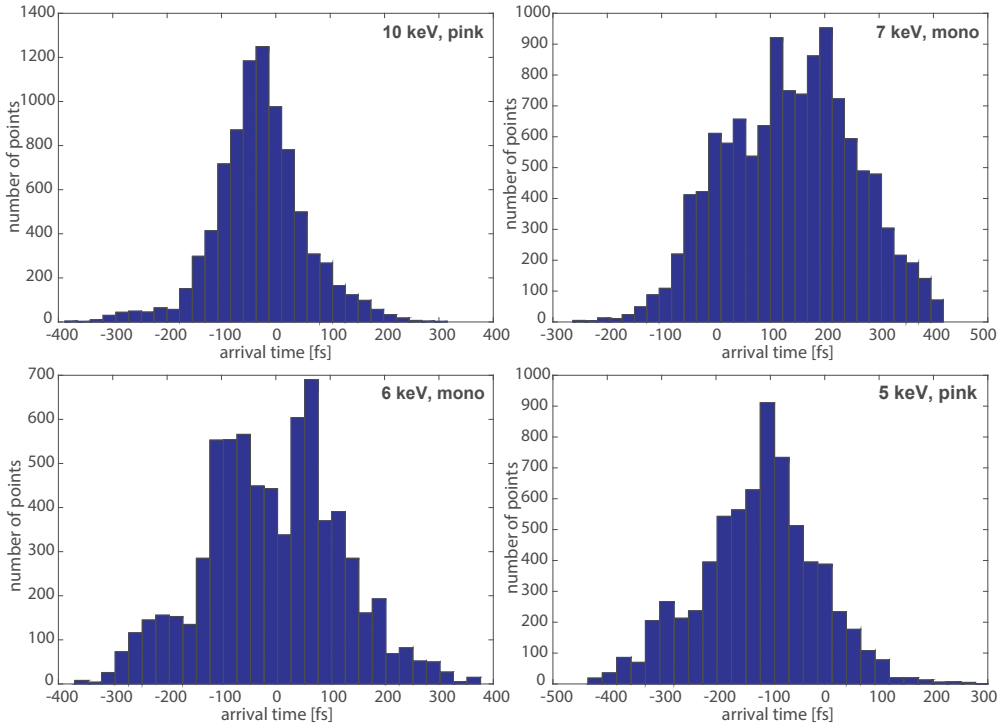


Figure 4.16: Distributions of the FEL arrival times relative to the experimental laser for different photon beams.

of the table along with the spread of the measured values for each photon beam configuration. The average values and the standard deviations are calculated from about 2000 FEL pulses on average, arriving at the central area of the linear slope of the vector potential. The spread of the calculated pulse length values originate from two main effects: the pulse-to-pulse jitter of the FEL durations and the measurement uncertainty of the eTOFs, which are both presented in table 4.3. The uncertainty of the pulse length caused by the eTOF measurements was found by estimating the spectral width measurement uncertainty and propagating it through the equation of the pulse length calculation.

The spectral width measurement accuracy was estimated using measurements with the THz beam blocked, similar to the procedure used in the arrival time analysis to determine the central energy measurement accuracy. During the measurements without the THz beam, the spectra of the photoelectrons are not broadened, and the spectral widths measured by both eTOFs are the same within the measurement accuracy. The difference of the spectral widths

4.2. First measurements of hard X-ray FEL pulses at SACLA

obtained from the two eTOFs gives the overall uncertainty from both of the spectrometers. Assuming that the two eTOFs are identical, the contribution of each eTOF in the overall uncertainty is found by dividing this uncertainty by square root of two. The resulting average accuracy of each eTOF for the spectral width measurement was obtained to be about 0.7 eV corresponding to a relative accuracy of about 5-10%.

The uncertainty propagation was done statistically. For each spectral width, 5000 points with a normal distribution were generated with the rms spread of the eTOF accuracy and the central value of the measured width. Using the two streaked and the two non-streaked

Table 4.3: The average FEL pulse lengths and their standard deviations for different photon beams, uncertainties from the eTOF measurements and the average chirps.

Photon beam	Streaking strength [eV/fs]	FEL length [fs]	eTOF accuracy [fs]	Length jitter [fs]	Chirp [meV/fs]
10 keV, pink	0.32	32±7	4.4	6.1	-6.3
9 keV, pink	0.27	33±6	4.8	4.3	17.5
8 keV, pink	0.21	37±18	6.5	16.3	26.8
7 keV, pink	0.13	40±20	8.0	18.0	22.8
6 keV, pink	0.12	26±14	11.3	8.0	-54.8
5 keV, pink	0.2	45±13	7.1	11.1	0.7
9 keV, mono	0.2	33±14	8.0	11.2	8.6
8 keV, mono	0.25	30±13	5.5	12.0	-1.1
7 keV, mono	0.14	63±16	9.3	12.7	-0.7
6 keV, mono	0.13	53±18	6.9	17.0	6.9

spectral widths with their distributions, the pulse lengths were calculated for all 5000 cases. The standard deviation of the obtained pulse length values is the uncertainty of the pulse length measurement from the eTOFs shown in the 4th column of table 4.3. The values from the 5th column of the table corresponding to FEL pulse length jitter from shot to shot, are obtained by quadratically subtracting the eTOF accuracy values from the overall rms spread of the calculated pulse lengths. One can see from the table that the uncertainties from the eTOF measurements are smaller in case of the stronger streaking as already found previously.

The average pulse lengths obtained for different photon beam configurations vary from 26 fs up to 63 fs rms. The discussion about the different pulse duration values obtained from the measurements, is given in the next chapter. The distributions of the pulse length measurement results for four different photon beams are shown in figure 4.17. The standard deviations of the distributions shown in the figure correspond to the values presented in the 3rd column of table 4.3 and are composed of the eTOF measurement uncertainties and the pulse-to-pulse jitter (columns 4 and 5, respectively in table 4.3).

Chapter 4. Measurements

The obtained results for the FEL pulse duration provide larger values than anticipated from the SACLA beam specifications, predicting about 4-5 fs pulse lengths in rms. During the measurements at SACLA there was no other pulse length measurement setup available that could be operated in parallel with PALM, and the cross-comparison of the measured values with another measurement method was not possible.

The linear energy chirp values obtained from the measurements are shown in the last column of table 4.3. The results indicate mainly positive linear chirp corresponding a higher photon

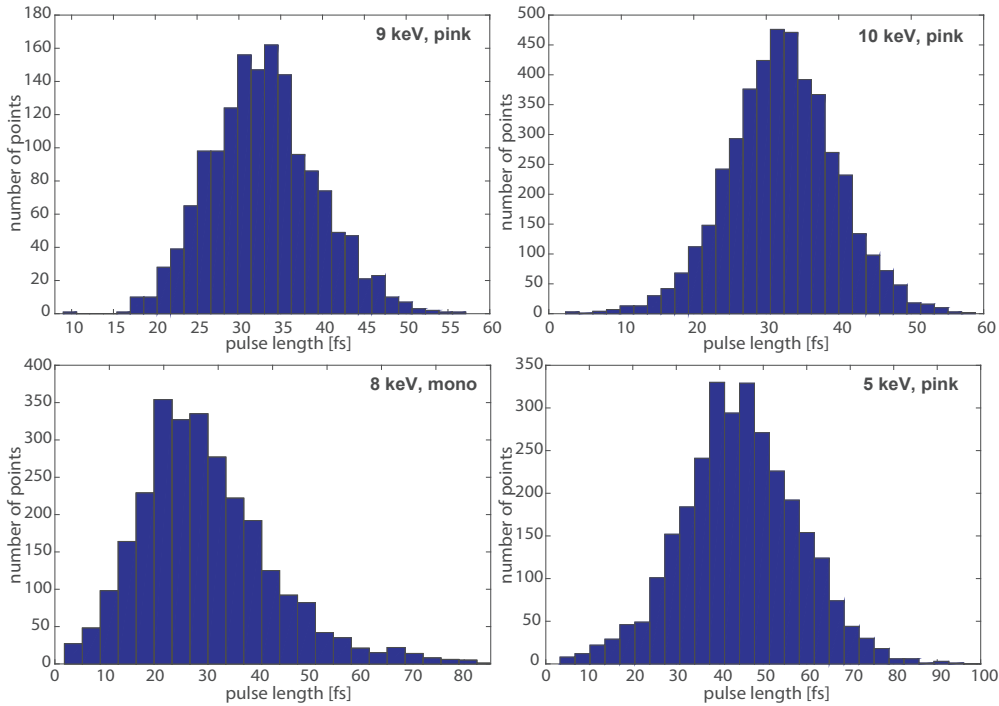


Figure 4.17: Distributions of the rms FEL pulse durations measured for different photon beam configurations.

energy at the head of the pulse. One can also see from the table that the measurements with monochromatic beam reveal much smaller chirps compared to the pink beam. Such a result is expected as the monochromator reduces the bandwidth of the FEL pulse.

As mentioned before, the pulse length retrieval procedure reconstructed the non-streaked spectra using the fitting curves shown in figure 4.15. The fits were performed to the spectral widths obtained from averaging of 100 measured spectra. Using these fits for the reconstruction of the widths of the non-streaked spectra does not take into account the spectral width jitter. This induces an additional uncertainty in the pulse length calculation. For the pink beam this uncertainty varies from 4 fs up to 9.6 fs and it is smaller for a stronger streaking. For the monochromatic beam the spectral jitter is smaller than the eTOF accuracies, and the effect is negligible.

In addition to the results provided in table 4.3, the peak strength of the electric field was also calculated from the streaking measurements. This was done following the same procedure

4.3. FEL measurements with the second generation setup

as described in the section 4.1. The vector potential was calculated from the kinetic energy shift of the photoelectrons due to the interaction with the THz field during the delay scan, in accordance with equation 4.5. The electric field strength was then obtained by calculating the time derivative of the vector potential: $E(t) = -\partial A(t)/\partial t$. The obtained result for the THz field is shown in figure 4.18. One can see from the figure that the peak electric field strength is about 6 MV/m with overall duration of about 2 ps (0.52 THz). In order to validate this result, the THz field was measured also by an electro-optical sampling method [54, 112] before and after the FEL measurements. The obtained results were consistent with the ones reconstructed from the THz delay scan measurements. Furthermore, the analysis of the measurements with

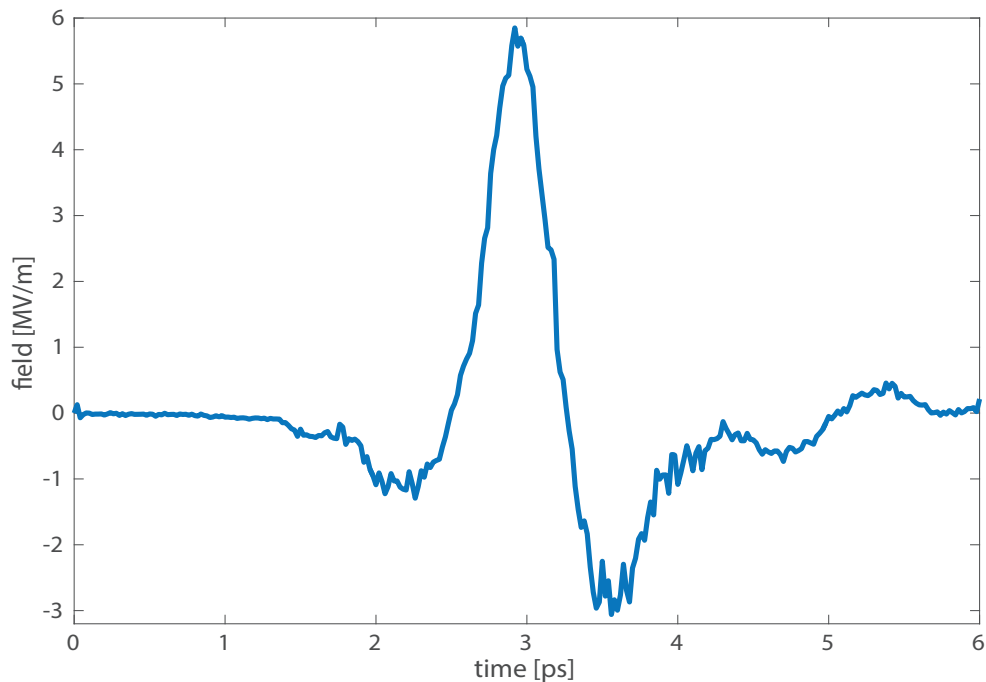


Figure 4.18: Electric field strength of the THz pulse reconstructed from the delay scan measurements.

different photon beam configurations revealed the same electric field strength and shape for all cases. These results confirm that the generated THz beam used during the measurements was stable.

The measurements performed with the PALM prototype setup at SACLA were the first of their kind, and they proved the applicability of the THz streak camera method for the measurement of hard X-ray photon pulses.

4.3 FEL measurements with the second generation setup

The second generation PALM setup is able to simultaneously measure the spectra of both streaked and non-streaked photoelectrons from the same FEL pulse. This allows to unambigu-

ously reconstruct the rms duration of the photon pulse. The purpose of the third measurements of this thesis was to test the new PALM setup with a hard X-ray FEL beam, compare our measurement results with other diagnostics tools at SACLA that were not operational during the first beam time, and perform measurements with the 2-color mode of SACLA. The measurements were performed during 5 consecutive shifts of 12 hours. They took place in January of 2016 with the proposal number 2015B8002.

4.3.1 Single-shot measurement procedure and the data processing

The measurements with the PALM setup took place at the beamline 3 (BL3) of SACLA in the experimental hutch 2 (EH2). The photon diagnostics system of SACLA was positioned in the experimental hutch 1 (EH1) upstream to the THz streak camera setup. The description of the diagnostics system in the EH1 is given in [95, 115]. The overview of the experimental setup in the hutches is shown in figure 4.19. Before reaching the EH1 and EH2, the FEL beam propagates through a transmission grating that separates two small fractions of the beam as ± 1 st order branches. The -1st order branch is directed to a GaAs crystal inducing a change in

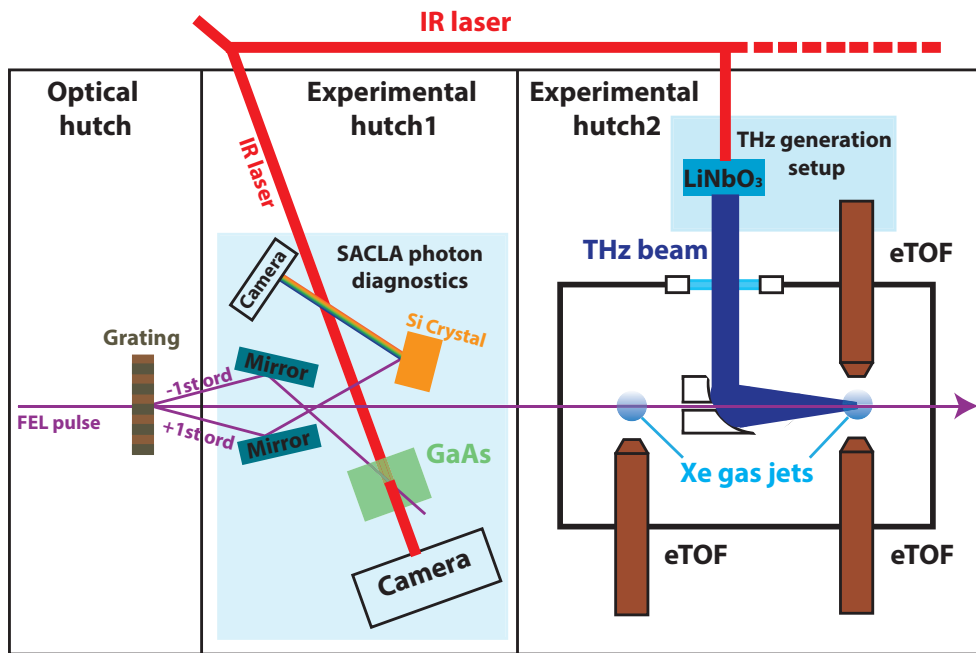


Figure 4.19: The schematic view of the SACLA photon diagnostics system and the experimental setup in the experimental hutches.

its reflectivity/transmission, which is encoded in the IR experimental laser of SACLA to obtain the relative arrival time of the FEL pulses [116]. The IR laser was split in two parts during the measurements, and the second part was used for the THz generation. Such configuration ensured that both the transient reflectivity setup and the PALM setup measured the arrival time of the same FEL pulse relative to the same IR pulse. The branch of +1st order of the FEL

4.3. FEL measurements with the second generation setup

beam is used to measure the spectrum of the FEL pulse. It is directed to a silicon crystal to disperse the beam, which is then detected by a CCD camera. Using a Si (111) or a Si (444) crystal allows to measure the spectrum in a large bandwidth or a narrow bandwidth with a high-resolution, respectively [117]. Using the Si (444) crystal allows resolving the widths of individual spikes in the spectrum, making it possible to obtain information about the temporal profile of the FEL pulse [20] as discussed in section 1.2. Operating both the PALM setup and the high-resolution spectrometer allowed to compare the results of the two methods on a single-shot basis.

The experimental setup used during the measurements is described in section 3.2. The PALM was connected to the FEL beamline and the overlap of the gas jet, the FEL pulse and the THz pulse was found in time and space using the same procedure as described previously.

The measurements were performed with an FEL beam of 9000 eV photon energy. The spectral bandwidth of the FEL pulses was about 25 eV in rms, which was significantly larger compared to about 14 eV bandwidth observed during the first beam time at SACLA. The photon pulse energy was about 250 μJ on average during the experiment. In addition to the measurements with the 9000 eV photon beam, more measurements were carried out using the 2-color operation mode of SACLA. This mode delivers two FEL pulses of different photon energies (colors) with a tunable temporal separation between them [118]. The energies of the two FEL pulses were 8800 eV and 9000 eV, while the temporal delay between them was changed from 0 fs to 50 fs during the measurements. The total energy of the two pulses was about 150 μJ during the 2-color mode. For both operation modes the repetition rate of the machine was 30 Hz.

The electrons ionized from the $2p_{3/2}$ shell of Xe with a binding energy of 4786 eV were measured by three eTOF spectrometers. One of the eTOFs was measuring the non-streaked electron spectra from the first interaction point without a THz beam. The other two eTOFs were measuring the photoelectron spectra streaked in opposite directions by the THz pulse. All three eTOFs measured the energy spectra of the electrons created by the same FEL pulse, allowing the calculation of the photon pulse duration on a single-shot basis.

As in case of the previous experiments, the first step in the measurements was to calibrate the eTOF spectrometers. This was done following a different procedure compared to the other two measurements. It was possible to change the photon energy of the FEL beam within a small range around the nominal value of 9000 eV. The FEL radiation wavelength depends on the K parameter of the undulator as shown in equation 1.10 of section 1.1. At the same time, the undulator parameter depends on the gap of the undulator. This means that by changing the gap of the undulator, it is possible to control the central energy of the FEL beam within a small range, where the lasing conditions inside the undulator remain unchanged. Using this method, the FEL photon energy was scanned from 8700 eV up to 9200 eV with 50 eV steps. For each value of the photon beam energy, about 2000 spectra were measured. The drift tube voltages applied in the eTOFs were not changed during the photon energy scan. This means that the final kinetic energy of the electrons before being registered by the MCP detectors was changed by the same amount as the photon energy, causing a corresponding change in their flight times measured by the eTOFs.

During the photon energy scan an online spectrometer of SACLA was used to measure the

Chapter 4. Measurements

central energy of each FEL pulse. The central kinetic energy of the retarded electrons was calculated by subtracting the drift tube voltage of the eTOF and the binding energy of the $2p_{3/2}$ shell from the photon energy of each FEL pulse. The obtained energy value was then linked to the temporal position of the electron peak in the signal of the eTOF. Combining all the energy values and the measured temporal positions, the calibration of all three eTOFs was done. The results of the calibrations are presented in figure 4.20. Each red circle shown in the

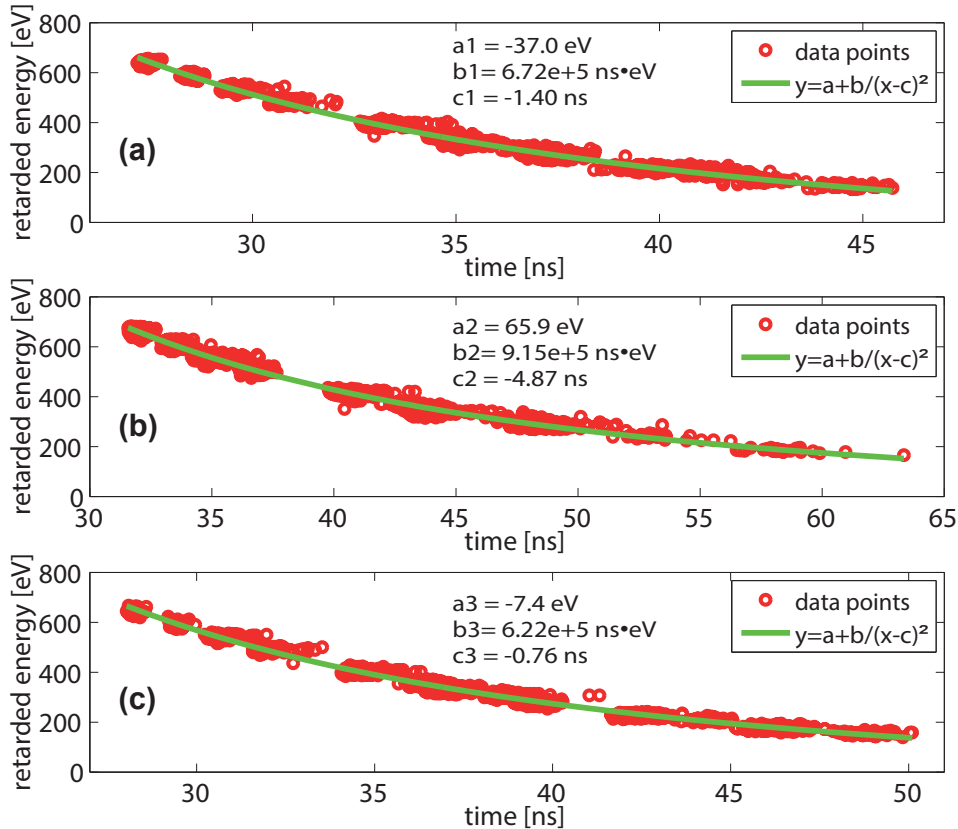


Figure 4.20: Calibration curves and the corresponding coefficients obtained for all three eTOFs. Subfigures (a), (b) and (c) show the results for eTOF1, eTOF2 and eTOF3, respectively.

figure represents a single FEL pulse, and it is given by the electron energy value and the corresponding eTOF peak position in time. Using the calibration coefficients shown in figure 4.20, the energy spectra of the photoelectrons measured by the eTOFs were reconstructed.

After the calibration process was completed, a delay scan was performed between the ionizing FEL pulses and the streaking THz pulses. The THz scans were performed by moving the linear delay stage with steps of about $6 \mu\text{m}$ corresponding to a temporal delay between the FEL and the THz pulses of about 20 fs. At each position of the delay stage, 100 consecutive spectra were measured by all three eTOFs. In this case, however, only two eTOFs were detecting the energy shift of the electrons due to the interaction with the THz field, while the third eTOF was measuring the electrons from the first interaction zone, where the electrons were not streaked. This allows to compare the streaked energy spectra to the reference non-streaked spectra on

4.3. FEL measurements with the second generation setup

a single-shot basis during the whole scan and better understand the changes in the spectra caused by the presence of the THz field. The normalized spectra of the photoelectrons measured during the delay scan are shown in figure 4.21. In case of the standard operation mode (left subfigure) one can clearly see the shape of the THz vector potential. The arrival time jitter between the FEL and the THz pulses was about 250 fs rms during this measurements. This is larger than the jitter observed during the first beam time at SACLA (reported in table 4.2). The consequence of the larger arrival time jitter is the larger effect of the flattening of the THz vector potential peak. The comparison of the scans shown in the left parts of figures 4.11 and 4.21 indicates that the reconstructed vector potential corresponding to 250 fs jitter has a larger flat part at the peak (figure 4.21) than the vector potential corresponding to about 115 fs jitter (figure 4.11). The right side of figure 4.21 shows the scan with the 2-color beam.

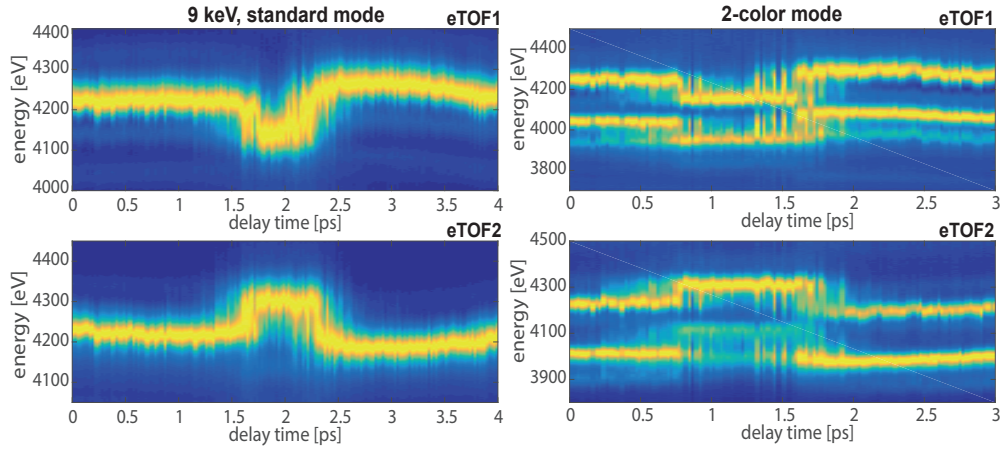


Figure 4.21: Evolution of the normalized spectra during the delay scan between the FEL and the THz beams. The plots on the left side show the scan during the standard operation mode with 9000 eV photon beam, while the ones on the right side correspond to the operation in 2-color mode.

One can clearly distinguish the two lines corresponding to the FEL beams of 8800 eV and 9000 eV. The two lines show the photoelectrons ionized from the same shell $2p_{3/2}$ of Xe by the two FEL pulses, and one can see from the figure that they are separated by 200 eV. The spectra in case of the 2-color beam are noisier compared to the single-color mode because of a smaller number of the ionized photoelectrons per FEL pulse and a less stable photon beam. The arrival time jitter of the two FEL pulses relative to the THz pulse was in range of 270-300 fs rms, which is larger than in case of the standard operation mode. This explains why the peak of the THz vector potential is flattened even more for the 2-color mode than for the single-color (figure 4.21). One can also see from the figure that the energy range of the eTOFs in case of the 2-color mode is larger than for the single-color mode to be able to accommodate both energy peaks separated by 200 eV during the delay scan. For this reason the resolution of the eTOFs for the measurement of each energy peak is worse compared to the measurement of a single energy peak.

Unlike the first measurements carried out at SACLA, during the second measurements the

arrival time monitor of SACLA was available and was operated in parallel to the PALM setup. During the delay scan measurements the relative arrival time of each FEL pulse was also measured with the SACLA monitor, using the X-ray induced transient reflectivity method. Having the data from the SACLA arrival time monitor allowed correcting the shape of the vector potential measured by PALM. For each central energy value measured by the eTOFs, a relative arrival time was found based on the reading of the timing tool of SACLA and the position of the delay stage during the scan. The results of the delay scan after the correction was applied are shown in figure 4.22. The shifted energy values were obtained by taking the central energies of the streaked spectra measured by eTOF1 and eTOF2 and subtracting the reference energy values of the non-streaked spectra measured by eTOF3. One can see from figure 4.22 that without the correction the maximum energy shift of the electrons corresponding to the peak of the vector potential is underestimated by about 20 eV. Only after compensating

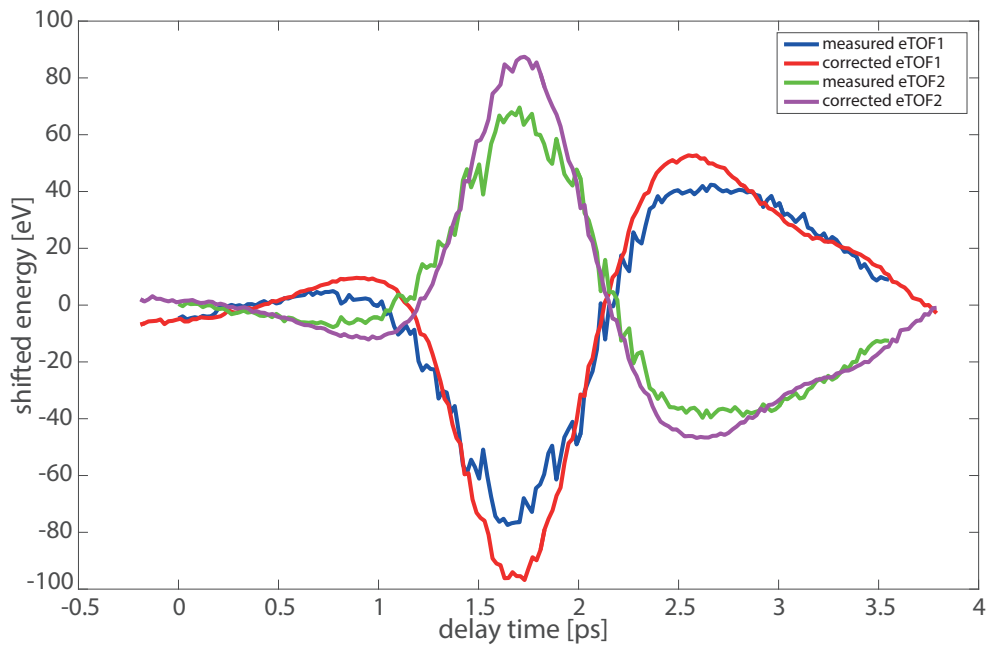


Figure 4.22: The energy shifts of the photoelectron spectra during the delay scan. The curves in blue and red show the energy shifts of the spectra measured by eTOF1 with respect to eTOF3 before and after correction, respectively. The curves in green and magenta correspond to the energy shifts relative to eTOF3, respectively, before and after correction measured by eTOF2.

for the arrival time jitter of the FEL pulses it is possible to reconstruct the true shape of the vector potential. Using the arrival time measurements from the timing tool of SACLA allows to account not only for the temporal jitter between the THz and the FEL pulses but also for possible average temporal drifts between these two beams. This can be seen in figure 4.22, where the curves without the correction (blue and green in the figure) are noisier than the ones with the correction (red and magenta in the figure) as the former ones contain the errors caused by the temporal drifts between the FEL and the THz beams during the delay scan. After reconstructing the shape of the THz pulse, three different points were chosen along the

4.3. FEL measurements with the second generation setup

linear slope of the THz vector potential. The delay stage was positioned corresponding to these points, and about 10000 consecutive spectra were measured by all three eTOFs at each position. Measuring the photoelectron spectra at the linear part of the THz pulse allowed the calculation of the relative arrival times and the rms durations of the FEL pulses, which were later compared to the measurements from, respectively, the arrival time monitor and the high resolution spectrometer of SACLA.

During the 2-color operation mode the durations and the arrival times of both pulses were measured for different temporal separation between the two FEL pulses. The production of the two FEL pulses is achieved by propagating the electron bunch through two undulator sections with different parameters, where it emits FEL radiation with different photon energies. A magnetic chicane is positioned between these two undulator sections. The function of the chicane is to bend the electron beam from its initial linear trajectory and to force it to travel a longer path compared to a straight line. After emitting the first FEL pulse in the first undulator section, the electron bunch passes through the magnetic chicane, following a longer trajectory than the FEL pulse that propagates straight. For this reason the electron bunch arrives to the second undulator section with a delay compared to the first FEL pulse and, therefore, the second FEL pulse generated in the second undulator section arrives later than the first one. By changing the trajectory of the electron bunch inside the magnetic chicane, it is possible to control its delay relative to the first FEL pulse and, therefore, the temporal separation between the two FEL pulses.

During the measurements with the 2-color operation mode the delay between the two pulses was changed from 0 fs to 50 fs in steps of 10 fs. For each value of the temporal separation a delay scan between the THz pulse and the two FEL pulses was performed as already shown in figure 4.21. After the scan about 10000 spectra were measured at the linear part of the vector potential, similar to the case with the single-color operation. From these measurements it was possible to reconstruct the lengths of both FEL pulses, as well as their arrival times with respect to the THz pulse. Furthermore, the temporal separation between the two photon pulses was also measured and was compared to the value applied by the magnetic chicane.

The data processing starts by defining a procedure of calculating the rms width and the position of the energy peaks from the eTOF signals. An example of the energy spectra measured by the eTOFs is shown in figure 4.23 for both standard operation and 2-color operation modes. One can see from the figure that the non-streak spectra measured by eTOF3 (green curve in the figure) are narrower compared to the other two spectra that are measured by eTOF1 and eTOF2 (blue and red curves, respectively). The spectra measured during the 2-color operation mode exhibit larger noise compared to the ones from the standard mode. This is caused by the fact that the FEL beam was less stable during the 2-color operation, which resulted in larger uncertainties in the pulse length and arrival time calculations.

One can see from figure 4.23 that the energy peaks measured by the eTOFs are not symmetric and sometimes contain a double peak structure. Unlike the other two measurements performed earlier, the energy spectra obtained during the third measurements do not have Gaussian shapes, and fitting Gaussian profiles to the peaks do not represent the peak parameters accurately. For this reason during the data analysis it was chosen to calculate the center

of mass and the standard deviation of an energy peak distribution to find the peak position and its width, respectively. The main complication with this method is to define correctly the range of the peak, where the center of mass and the standard deviation should be calculated. The first step in characterizing the energy peak is to manually define an energy window that includes only the peak of interest. In this energy range only the part of the signal that is higher

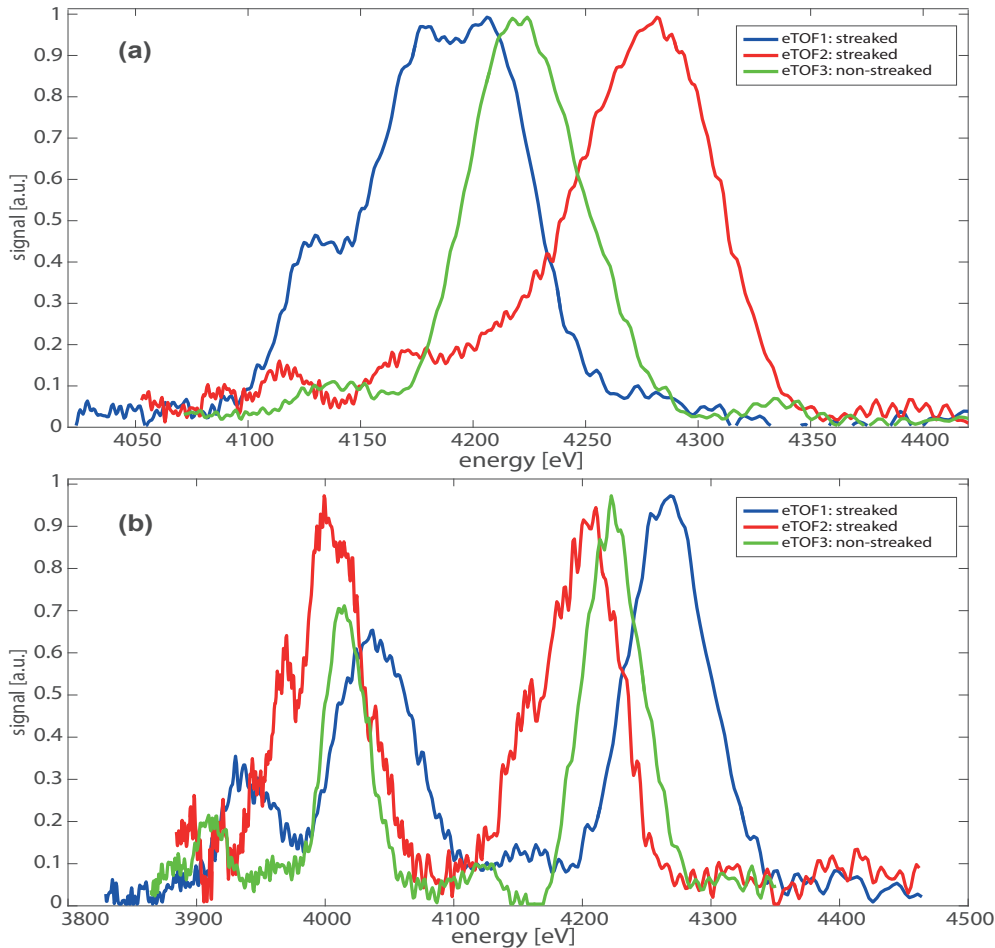


Figure 4.23: Normalized photoelectron spectra measured by all three eTOFs for the single-color 9000 eV photon energy mode (a) and the 2-color mode (b). The spectra correspond to the arrival of the FEL pulses at the linear part of the THz vector potential.

than a certain threshold is considered as a part of the peak. The threshold is taken as a fraction of the maximum peak value. After studying carefully the signals of the three eTOFs from different measurements, the threshold values were chosen from 10th to 5th fraction of the maximal signal of the peak, depending on the signal-to-noise ratio of the eTOF signals. Once the area of the peak is defined, the center of mass and the standard deviation of the distribution is calculated. Obtaining the peak positions and the spectral widths of the non-streaked and the two streaked photoelectron spectra from the same FEL pulse, the relative arrival time and the rms duration of that pulse were calculated.

4.3. FEL measurements with the second generation setup

In case of the measurement data from the 2-color operation, each of the peaks was characterized as described above. The initial approximate ranges of the two peaks were found using the fact that the separation between them is about 200 eV.

The calculations were performed for the photon pulses that arrived at about 450 fs-long linear area of the vector potential, where PALM can measure with the highest accuracy.

4.3.2 Results from the single-shot measurements

The rms durations and the relative arrival times of the FEL pulses were calculated both for the 9000 eV operation mode and for the 2-color operation mode. During the standard operation mode of SACLA, measurements were performed for 5 different runs. The arrival time values obtained from PALM were compared to the results from the SACLA arrival time monitor on a pulse-to-pulse basis. The results from the arrival time measurements are shown in table 4.4. The relative jitter in the table shows the rms difference between the two measurement methods, while total uncertainty is the quadratic sum of the individual accuracies of the two monitors. The temporal accuracy of the SACLA arrival time monitor is 7 fs rms as reported

Table 4.4: Comparison of the relative arrival time measurements from PALM and the SACLA timing tool for 5 different runs. The rms jitter between the two measurements and the total uncertainty from both of the monitors are presented as well as the correlation coefficients.

Run number	Streaking strength [eV/fs]	Relative jitter [fs]	Total uncertainty [fs]	Correlation coeff.
#392001	0.23	16.8	16.5	0.987
#392002	0.23	17.0	16.5	0.986
#392037	0.23	16.5	16.3	0.990
#392039	0.23	16.4	16.3	0.989
#392044	0.23	16.7	16.4	0.990

in [115]. The accuracy of PALM is estimated from measurements without the THz beam. In this case all three eTOFs measure the same non-streaked spectra from the same FEL pulse and the energy peak position jitter between the eTOFs indicate their average measurement accuracies. The average accuracy of a single eTOF was found to be about $\sigma_{eTOF} = 2.4$ eV. The uncertainty of the energy shift obtained by subtracting the measurements from two eTOFs is then $\sqrt{2}\sigma_{eTOF} = 3.4$ eV. Multiplying this value by the streaking strength gives the arrival time measurement accuracy of the PALM setup $\sigma_{PALM} = 14.8$ fs. One can see from table 4.4 that the streaking strength is the same for all the runs indicating the stability of the THz beam. The total uncertainties obtained from the individual accuracies of the two detectors are very close to the values of the relative jitter between the two measurements. The small difference between the expected and the measured jitter can be explained by the relative temporal jitter

Chapter 4. Measurements

between the two optical laser pulses used in EH1 and EH2 for the SACLA spatial encoding and THz generation, respectively. Even though these laser pulses are two parts of the same laser pulse, they propagate through different optical components before being used for the arrival time measurements, and this can cause a relative temporal jitter between them.

One can also see from the table that the arrival time measurements from the two setups are highly correlated with a correlation coefficient of about 0.99. Table 4.4 also shows that even though the measurements from different runs were performed at different times, the results obtained from these runs are very consistent. This means that during the measurements both the FEL beam and the two measurement setups were stable and reproducible.

Figure 4.24 shows some results from the comparison of the two measurement methods from different runs. In the first subfigure (a) the distribution of the difference of the arrival times

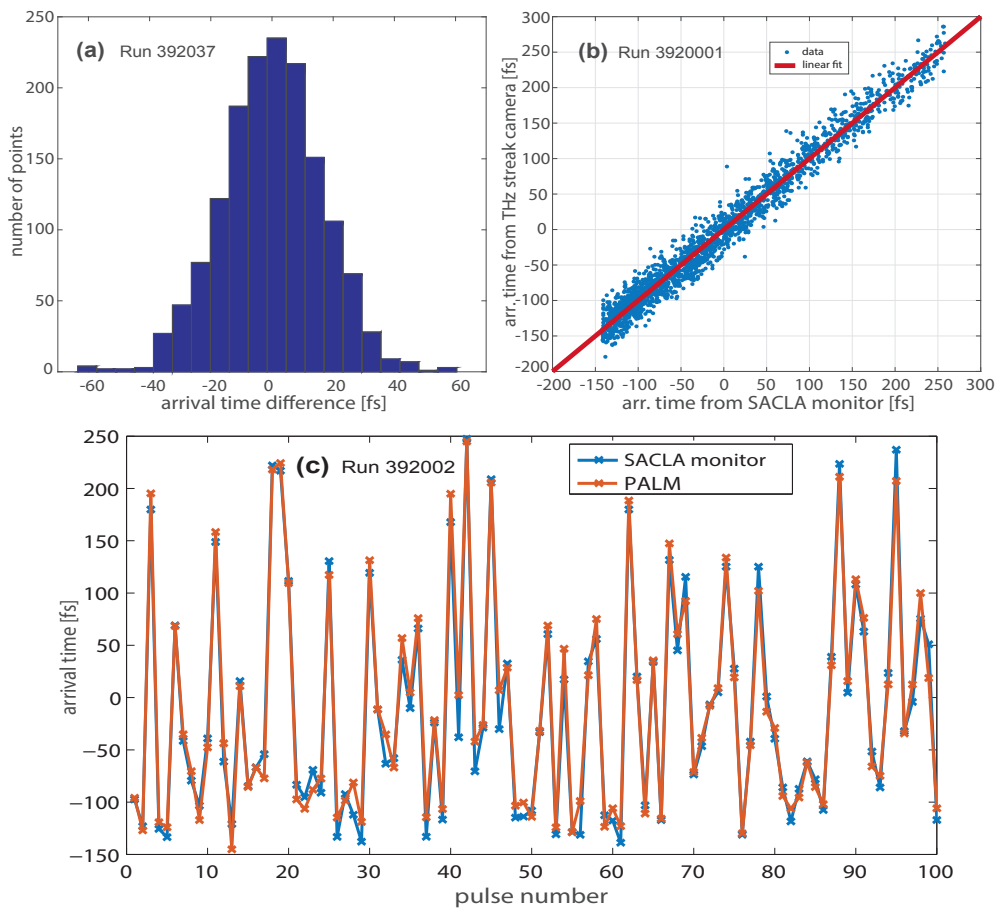


Figure 4.24: Comparison of the arrival time measurements from PALM and SACLA time monitor. Subfigure (a) shows the distribution of the difference between the two methods, (b) shows the correlation between the two measurement values and (c) shows the arrival time values measured by the two methods.

measured from the two monitors is shown. The standard deviation from this distribution gives the overall rms jitter between the two measurement methods and is shown in table 4.4.

4.3. FEL measurements with the second generation setup

The second subfigure (b) demonstrates the correlation between the two measurement data. The spread of the blue dots around the diagonal red line in subfigure (b) indicates the relative jitter between the two detectors. The arrival times of 100 consecutive FEL pulses measured by both methods are shown in subfigure (c). One can see that the measurements from the two monitors are consistent and follow the same pattern.

The arrival time of the FEL pulses were measured also during the 2-color operation mode. In this case the arrival times of both FEL pulses were measured simultaneously by the PALM setup, and calculating the difference between the two arrival times provided the delay of the two photon pulses set by the magnetic chicane. The comparison of the measured delay values and the set values is shown in figure 4.25. One can see from the figure that the measured delay values show a high correlation of about 0.99 with the values set by the magnetic chicane. The offset of about 4 fs can be caused by the fact that the two FEL pulses were emitted from

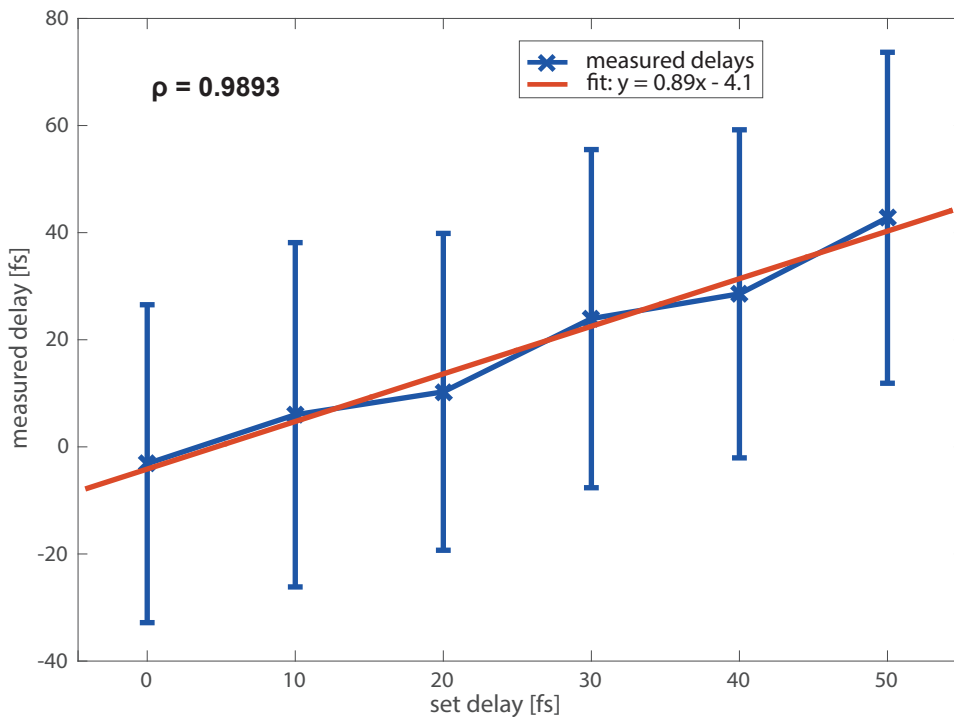


Figure 4.25: The delay values between the two FEL pulses set by the magnetic chicane and measured by the THz streak camera.

different parts along the electron bunch. The vertical bars in figure 4.25 correspond to the standard deviations of the measured delay values for each step of the delay scan and have an average value of about 31 fs. The main contribution in this jitter is from the accuracies of the eTOF spectrometers. For the 2-color operation the energy accuracies of the eTOFs were calculated to be about 3.0 eV and 3.2 eV for the high-energy and low-energy peaks, respectively. Following the same uncertainty propagation as was done for the single-color operation measurements, the arrival time measurement accuracies for the two FEL pulses were found to be 17.0 fs and 17.3 fs. It is worth noting that these accuracies are worse compared to the value

Chapter 4. Measurements

obtained for the single-color operation mode. This is caused by the fact that the photon beam stability was worse in case of the 2-color operation mode, as one can see from figures 4.21 and 4.23. The uncertainty of the delay measurement caused by the eTOFs is the quadratic sum of the arrival time measurement accuracies of the two FEL pulses and is equal to 24.3 fs. The remaining part of the total jitter is about 19 fs. This value can serve as an estimate of the upper limit of the temporal jitter between the two FEL pulses. The simultaneous measurement of the arrival times of the two FEL pulses was the first measurement of its kind.

The rms duration of each FEL pulse was calculated using the three photoelectron spectra measured by the three eTOFs. The spectral width of the non-streaked spectrum was quadratically subtracted from the spectral widths of the two streaked spectra, and the pulse length was calculated according to equation 1.42. The results from the pulse length measurements are presented in table 4.5. The rms pulse durations measured by the PALM setup are in range from 91 fs to 96 fs with an overall rms jitter of about 15 fs. The measurement uncertainty

Table 4.5: The average FEL pulse lengths and their standard deviations for different runs, uncertainties from the eTOF measurements and the average chirps.

Run number	FEL length [fs]	eTOF accuracy [fs]	Length jitter [fs]	Chirp [meV/fs]
#392001	91±15	13.4	7.1	3.6
#392002	91±16	13.7	8.5	4.9
#392037	93±15	13.1	6.2	5.6
#392039	96±14	13.1	5.0	3.2
#392044	92±16	13.8	7.6	6.5

caused by the eTOF accuracies was calculated as in the previous measurements. About 10000 non-streaked spectra were measured while the THz beam was blocked, and the rms jitter between the spectral widths from the three eTOFs provided an estimate of the spectral width measurement accuracy. The average absolute accuracy of a single eTOF was found to be about 1.7 eV corresponding to a relative accuracy of 7.4%. The uncertainty of the eTOF measurements was propagated statistically as already described in section 4.2. The resulting pulse length measurement uncertainty caused by the eTOFs is about 13.4 fs on average. The rest of the jitter is mostly caused by the FEL pulse duration jitter, which is in range of 5-8.5 fs. One can see from table 4.5 that the calculated average chirps are all positive and vary from 3.2 meV/fs to 6.5 meV/fs. The streaking strengths used for the pulse length calculations are the same as shown in table 4.4 for the arrival time measurements.

The values obtained for the FEL pulse lengths are in range of 90 fs in rms, while the linear area of the THz vector potential was chosen to be about 450 fs. This means that even though the centers of the calculated FEL pulses arrive at the linear part of the THz pulse, not all of these pulses are entirely inside this 450 fs window. Some parts of the photon pulses away from the center may be outside of the predefined linear area of the THz vector potential, and these parts

4.3. FEL measurements with the second generation setup

will, consequently, be streaked slightly less compared to the central parts of the photon pulses that are at the steepest slope of the vector potential. For this reason the overall broadening of the photoelectron spectra produced by these FEL pulses will be less compared to those photon pulses that arrive entirely inside the linear part of 450 fs. Because of less broadening of the spectra the calculated rms lengths of some FEL pulses are underestimated. This effect can be observed in figure 4.26 that shows the distribution of the measured pulse lengths obtained from different runs. The distributions shown in the figure for all 4 runs are not symmetric

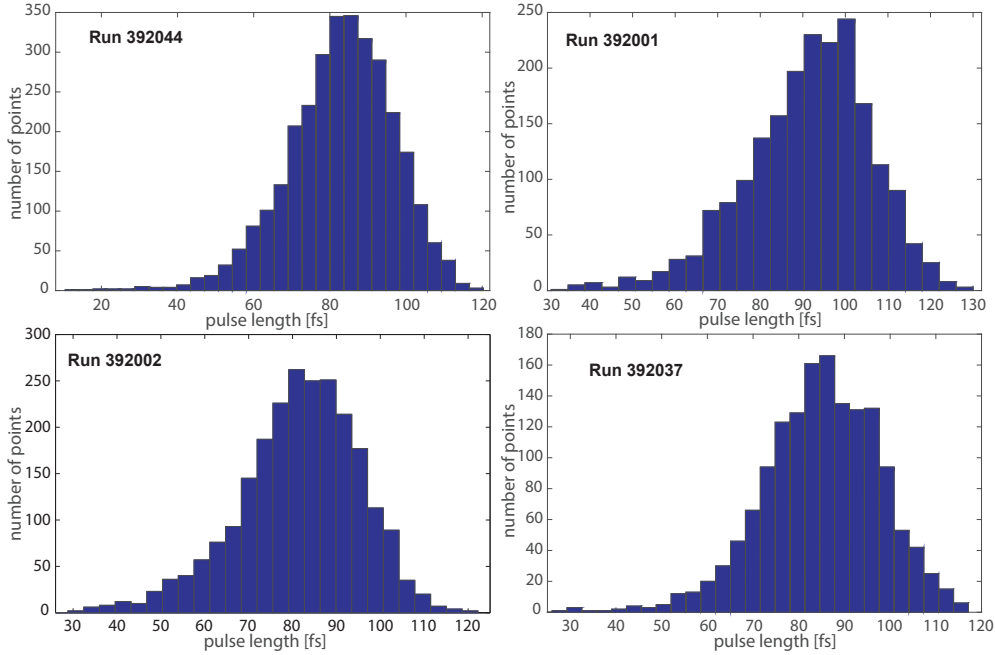


Figure 4.26: Distributions of the rms FEL pulse durations measured during different runs.

and have tails towards the lower values. The asymmetry is caused by the fact that some of the calculated pulse lengths are underestimated and the number of the shorter pulses is more than the number of the longer pulses.

In parallel to the PALM setup, the durations of the FEL pulses were also measured by the spectral method using the high-resolution spectrometer of SACLA [20, 115]. The results obtained from this method indicate values below 10 fs. The reasons of this inconsistency and possible explanations are provided in chapter 5.

The rms durations of the FEL pulses were also calculated for the measurements with the 2-color operation of SACLA. In this case the rms lengths were simultaneously calculated for both FEL pulses. For each photon pulse the length was obtained using a procedure similar to that of the single-color measurements. The results from the measurements with the 2-color mode are shown in table 4.6 for different temporal separations between the two FEL pulses. One can see from the table that the average pulse length values obtained for the first FEL pulse (with photon energy of 9000 eV) vary from 81 fs to 97 fs, while the pulse lengths for the second FEL pulse (with photon energy of 8800 eV) are in range of 55-67 fs. The overall pulse length jitter observed from the measurements is about 20.7 fs and 22 fs for the first

Chapter 4. Measurements

and the second pulses, respectively. The jitter for the 2-color mode is larger compared to the single-color mode. The pulse length measurement accuracies of the eTOFs were estimated from the measurements of the non-streak photoelectron spectra without the THz beam. The relative spectral width measurement accuracy for each eTOF was found to be on average 6.4% and 12.4% for the high-energy and low-energy photon pulses, respectively. Using these values, the uncertainties were propagated with a similar procedure as already described previously. The resulting pulse length calculation uncertainty caused by the eTOF accuracies is 10.7 fs for the first FEL pulse and about 12.3 fs for the second one. The remaining jitter is mostly caused

Table 4.6: Average rms durations of the FEL pulses and their standard deviations measured during the 2-color operation mode for different delay values. The measurement accuracy of the eTOFs, pulse length jitter and the linear energy chirp are presented for each FEL pulse.

Delay [fs]	Pulse 1, 9000 eV				Pulse 2, 8800 eV			
	Length [fs]	eTOF acc. [fs]	Jitter [fs]	Chirp [meV/fs]	Length [fs]	eTOF acc. [fs]	Jitter [fs]	Chirp [meV/fs]
0	81±20	10.0	17.1	0.6	55±20	11.7	16.2	38.5
10	97±19	10.9	15.6	-1.5	64±22	12.7	18.3	18.1
20	94±18	10.7	14.7	-1.2	63±22	12.2	17.9	24.8
30	93±22	10.9	19.3	5.4	65±23	12.4	19.5	10.1
40	94±19	10.7	15.2	1.4	67±22	12.4	17.8	15.9
50	89±26	11.1	23.4	10.9	65±23	12.4	19.7	10.3

by the shot-to-shot jitter of the FEL pulse durations (columns labeled Jitter in the table). The values for this jitter shown in table 4.6 are larger than the jitter values of the single-color FEL pulses shown in table 4.5. This shows that the machine was less stable during the 2-color operation, as already observed from other measurement results.

The average linear energy chirp of the first FEL pulse is mostly small and changes around zero from -1.5 meV/fs to 10.9 meV/fs, while the linear chirp of the second FEL pulse is larger and is positive for all the measurements. It changes from 10.1 meV/fs up to 38.5 meV/fs.

Comparing the rows of table 4.6 for different delay values between the two pulses, one can see that the measurement results are similar to each other. This result indicates the stability of the FEL beam and the reproducibility of the PALM setup during the measurements.

Using the results obtained from the measurements during the delay scan between the THz pulse and the FEL pulse, it was possible to reconstruct the electric field of the THz pulse. The reconstruction procedure is described in section 4.1 and it is based on equation 4.5. The obtained electric field of the THz pulse is shown in figure 4.27 for both eTOF1 and eTOF2. The frequency of the THz pulse is about 0.6 THz with a peak electric field strength of 8 MV/m. The obtained field strength value is consistent with the value provided by the measurements with the electro-optical sampling method.

4.3. FEL measurements with the second generation setup

The measurements with the second generation PALM setup proved the functionality of the system. For the first time ever, the arrival times and the rms lengths of two FEL pulses were simultaneously measured during the 2-color operation mode.

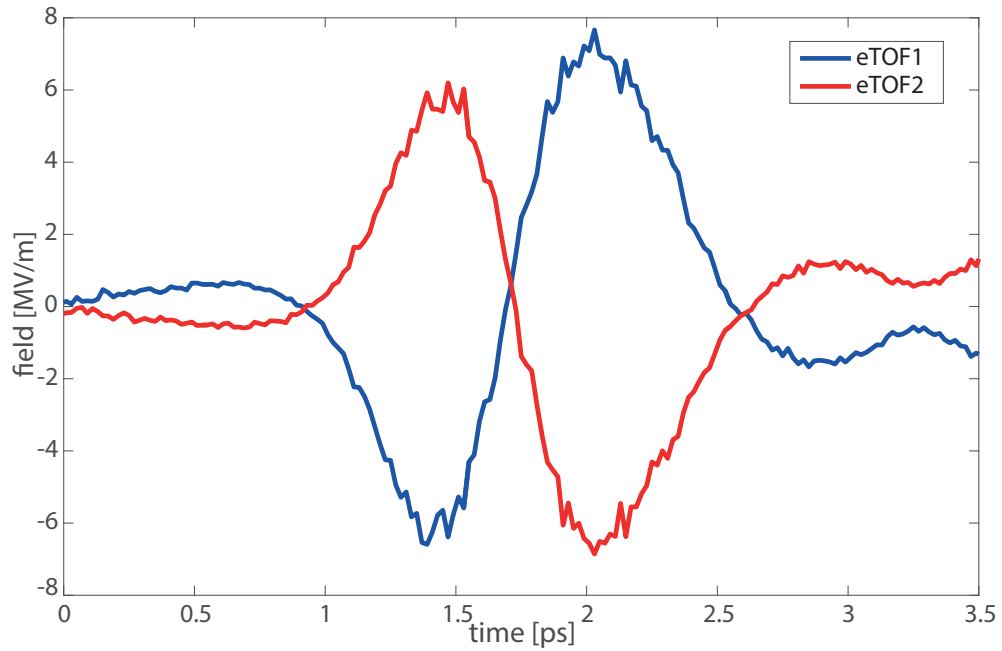


Figure 4.27: Electric field of the THz pulse reconstructed from the measurements with eTOF1 (blue curve) and eTOF2 (red curve).

5 Discussion

This chapter summarizes the results of the performed measurements and discusses the possible reasons of the discrepancy between the two pulse length measurement techniques observed at SACLA. It also provides various possibilities of improving the current measurement setup.

5.1 Discussion of the experimental results

The three experiments described in chapter 4 fulfilled their purpose of proving the concept of this thesis. The results obtained from the measurements showed that the light-field streaking method can be applied for the pulse length and arrival time measurement of the hard X-ray FEL pulses with a sub-10 fs accuracy.

During the first measurements performed with an HHG source, the streaking effect was observed for the first time with the prototype PALM setup, and the average rms durations of the HHG pulses were accurately calculated. The pulse lengths calculated for different harmonics using the steeper slope of the vector potential, had values in range from about 38 fs to 52 fs (figure 4.7), which is consistent with the expected values. The duration of each harmonic was calculated using the spectra from two different electron shells that were streaked by the THz pulse. The reproducibility of the measurements was determined by comparing the results from four different measurements, exhibiting precision values from 2 fs up to 18 fs, with better precisions corresponding to a stronger streaking (table 4.1). The linear energy chirp values obtained from the measurements were mainly negative and were in agreement with the expected values.

The number of the photoelectrons created by a single HHG pulse was not sufficient to represent the spectrum of the photon pulse, and for the pulse length calculation an average of 5000 spectra was used. As the HHG pulses are reproducible and do not vary largely from pulse to pulse, the spectral width jitter was smaller than the spectral broadening due to the streaking, and the averaging of the spectra did not induce a big uncertainty in the calculations. As a result, the average values of the HHG pulse lengths were calculated using the average of their spectra. The main contribution in the pulse length measurement uncertainty was

from the characterization of the streaked spectra. As the photon pulses ionized electrons from two shells $5p_{3/2}$ and $5p_{1/2}$ of Xe atoms with binding energies separated only by 1.3 eV, the spectra had a double-peak structure for each harmonic. When the two peaks were broadened due to the streaking effect, they had an overlap (figure 4.6), and characterizing the individual peaks was challenging. Meanwhile, the pulse length calculation uncertainties induced by the measurements and characterization of the non-streaked spectra were found to be in the order of a femtosecond or less.

The second experiment performed by the prototype PALM using the FEL beam at SACLA was the first measurement of the hard X-ray FEL pulses with a THz streaking technique. The arrival times of the FEL pulses with respect to the experimental laser were measured on a single-shot basis. The measurement results showed an rms jitter of about 115 fs between the arrival time of the FEL pulses and the experimental laser pulses (THz pulses). This result was in a good agreement with the specifications of the FEL beam at SACLA. The average accuracy of the arrival time measurement was about 5.5 fs for the photon beams without a monochromator and about 10.4 fs for the monochromatic beams. The measurement accuracy was worse in case of the monochromatic FEL beam as the photon intensity in this case was much lower than for the pink beam. This results in a smaller number of electrons being registered by the eTOFs and larger statistical fluctuations in the energy spectra. The rms pulse lengths measured for 10 different photon beams had values from about 26 fs up to 63 fs with an average value of 39 fs. Different pulse durations obtained at different measurement series are shown in figure 5.1. Subfigure (a) shows the obtained pulse lengths depending on the photon energy of

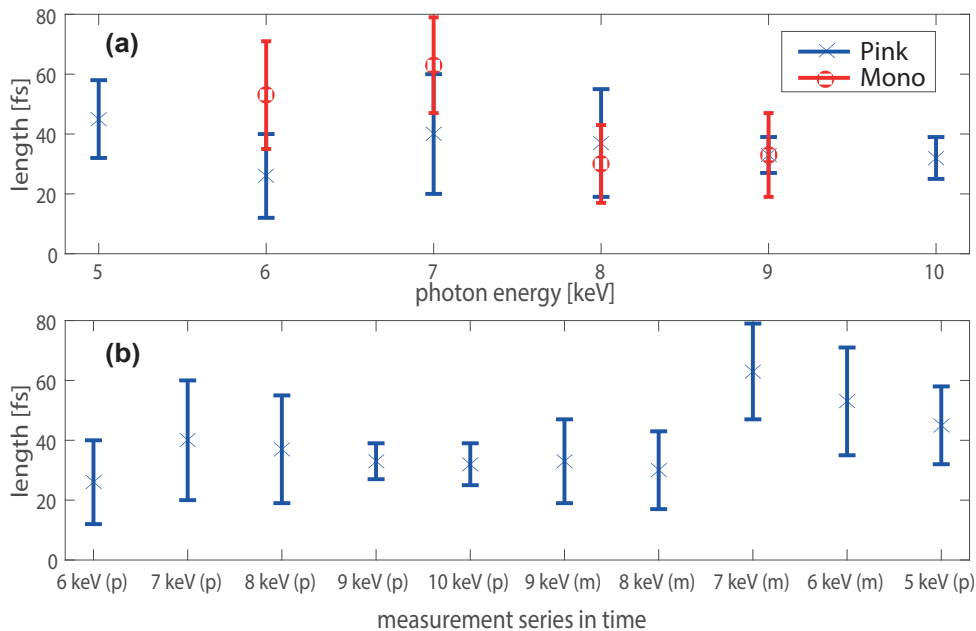


Figure 5.1: Pulse lengths depending on the photon energy (a) and the time of the measurements (b). Letters (p) and (m) in X-axis of (b) denote pink and monochromatic beams, respectively.

the pink (blue crosses) and the monochromatic (red circles) FEL beams. One can notice from the subfigure that there is no evident pattern describing a dependence of the pulse durations on the photon energy, and hence, different values of the pulse lengths are not correlated with the radiation wavelengths. On the other hand, in figure 5.1b the pulse length values are ordered chronologically, depending on the time they were measured. This plot shows that the pulse length was mostly stable and was varying around the value of 30 fs during the most of the measurements. However, towards the end of the beam time, it experienced a small jump and then started decreasing again. These results demonstrate how the measurements from PALM can be used for monitoring the behavior of the FEL beam and the performance of the machine itself.

The vertical bars in figure 5.1 show the overall spread of the measured values for each photon beam. The main contributions in this spread are from the eTOF measurement accuracies and the pulse length jitter itself. As shown in table 4.3, the pulse length uncertainties caused by the eTOF measurements were mainly below 10 fs during the measurements, with an average value of 7 fs. These uncertainties include both the eTOF accuracies and the statistical fluctuations of the measured spectra.

The rms values of the pulse lengths obtained from the measurements were longer than the sub-10 fs lengths specified by SACLA. Such short pulse length values provided by SACLA were obtained from simulations at SACLA and were not measured experimentally during the beam time. A possible explanation for such discrepancy can be that during the measurements some beam parameters at SACLA were different than those used in the simulations, and the delivered FEL pulses were, therefore, longer than expected.

Another issue encountered during the first measurements at SACLA was the temporal drifts between the FEL beam and the experimental laser beam. As already observed in figure 4.13, because of these drifts the reconstructed vector potential is not smooth and experiences small jumps. This complicates the process of choosing the linear area of the slope, along which the streaking strength remains unchanged, and may reduce the overall dynamic range of the detector.

The measurements with the prototype PALM setup at SACLA proved the capability of the method to measure FEL pulses with photon energies as high as 10000 eV with accuracies of down to sub-10 fs. The results from the measurements also pointed out the importance of measuring simultaneously the two streaked spectra as well as the non-streaked spectrum of the photoelectrons from the same photon pulse. The first measurements also showed that the correct reconstruction of the shape of the THz vector potential and calculation of the streaking strength is of big importance, and it can affect the final results.

The third experiment of this thesis was also carried out at SACLA, using the second generation experimental setup that is able to measure both the arrival time and the duration of the FEL pulses on a single-shot basis. During the measurements the photon diagnostics of SACLA were operated synchronously with the PALM setup and provided the relative arrival times of the FEL pulses and the widths of individual spikes of their spectra (allowing to reconstruct the pulse durations). In addition to the standard operation, measurements were performed using the 2-color mode of SACLA.

The arrival time of the FEL pulses during the standard operation mode was measured by PALM with an accuracy of about 14.8 fs. The results obtained from the measurements were compared to the measurements from the arrival time monitor of SACLA. The comparison showed an excellent agreement of the two techniques within their individual accuracies. During the 2-color operation the arrival time of both FEL pulses were measured simultaneously, and the temporal delay between them was calculated. This delay was set by a magnetic chicane that delayed the electron bunch between the two undulator sections. The second generation PALM setup was able to measure these delays, showing a high correlation ($\rho=0.99$) between the measured values and the delay values set by the chicane. The arrival time measurement accuracy of each individual pulse was about 17 fs. This is worse than the accuracy of the single-pulse arrival time measurement. Such a result is caused by the fact that the spectra measured during the 2-color operation were noisier because of smaller number of registered photoelectrons, and the peak positions of the spectra were, hence, defined less accurately.

The rms durations of the FEL pulses were also measured on a single-shot basis for the standard operation and the 2-color operation modes of SACLA. The measured pulse lengths in the standard operation mode were in range from 91 fs to 96 fs rms and did not vary largely, indicating a good stability of the FEL beam throughout the standard operation. The measurements with the 2-color operation revealed pulse lengths of about 91 fs for the FEL pulse with a photon energy of 9000 eV that arrives first, and about 63 fs for the 8800 eV pulse arriving second. The pulse length values obtained for both pulses during different runs did not experience large changes and showed a good stability during the measurements.

The durations of the FEL pulses were also obtained using the spectra from the high-resolution spectrometer available at SACLA. This spectrometer measures the individual spikes from the SASE spectrum of the FEL pulses within a small range of the overall spectrum (about 15%). Two examples of such measurements are shown in figure 5.2. Analyzing separate spikes from the waveforms shown in the figure, the FEL pulse lengths can be calculated [20] based on the fact that the profiles of the pulse in the frequency domain and in the time domain are related by a Fourier transformation. The rms durations of the FEL pulses retrieved by this method had values of sub-10 fs. Such a result does not agree with the results delivered by the THz streaking measurements. There are different effects that could have caused such a disagreement.

Longer durations of the photon pulses correspond to narrower spikes in the energy spectrum, which may not be resolved by the spectrometer at SACLA. The number of data points measured per individual spike (the red crosses shown in figure 5.2) in the spectrum is about 10 on average. This means that the spectrometer may not resolve the fine structure of the spectrum with energy spikes that are narrower than the ones shown in the figure with the rms widths of about 150 meV. For this reason the spectral measurement method may underestimate the pulse lengths by not being able to resolve the narrow spikes corresponding to the longer pulses. Furthermore, as it is mentioned in [20], this method is very sensitive to the linear energy chirp along the FEL pulse. Taking into account the energy chirp obtained from the measurements, the pulse length values provided by the high-resolution spectrometer may be underestimated by an order of magnitude or more. The overall pulse length can be accurately reconstructed from a single energy spike only when there is no energy chirp. This reconstruction method

gives information only about the photons that contribute to the frequencies within the FEL bandwidth ($\sim 10^{-4}$). The overall spectral bandwidth of the FEL pulses was at least an order of magnitude larger than the FEL bandwidth during the measurements. This means that in

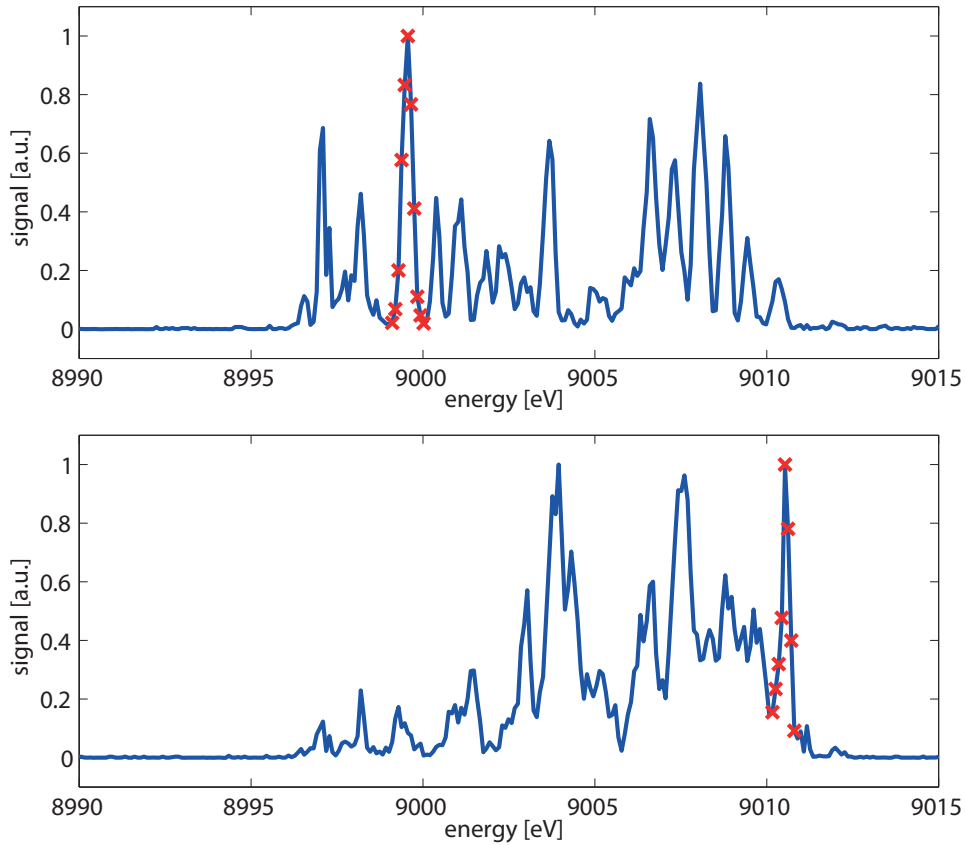


Figure 5.2: Energy spikes from the FEL spectra measured by the high-resolution spectrometer of SACLA. The red crosses correspond to the measured points in the spikes.

presence of a linear energy chirp, many photons along the FEL pulse had energies outside of the FEL bandwidth, and the analysis of single spikes shown in figure 5.2 could not provide any information about these photons. From this discussion one can conclude that the results obtained from the high-resolution spectrometer of SACLA provide the duration of only a small part of the overall pulse and, therefore, the two measurement methods did not measure the same thing during the beam time.

Figure 5.3 shows four different FEL spectra measured by the large bandwidth spectrometer of SACLA. Analyzing these spectra measured during the beam time at SACLA, it was found that they contain overall about 200 energy spikes. This corresponds to the same number of spikes in the temporal profile of the FEL pulse. Considering a pulse duration of only few femtoseconds, as obtained from the high-resolution spectrometer of SACLA, each of these 200 spikes would have a duration of only a few attoseconds (the separation between the spikes is about 5 times the spike width). Taking into account the parameters of the electron beam and the undulators used for the FEL generation, this would correspond to a lasing and a

saturation within only a few meters, which is not realistic. Such a result confirms the above mentioned statement that the spectral spike width measurement method underestimates the actual durations of the FEL pulses in presence of a linear energy chirp. Furthermore, assuming

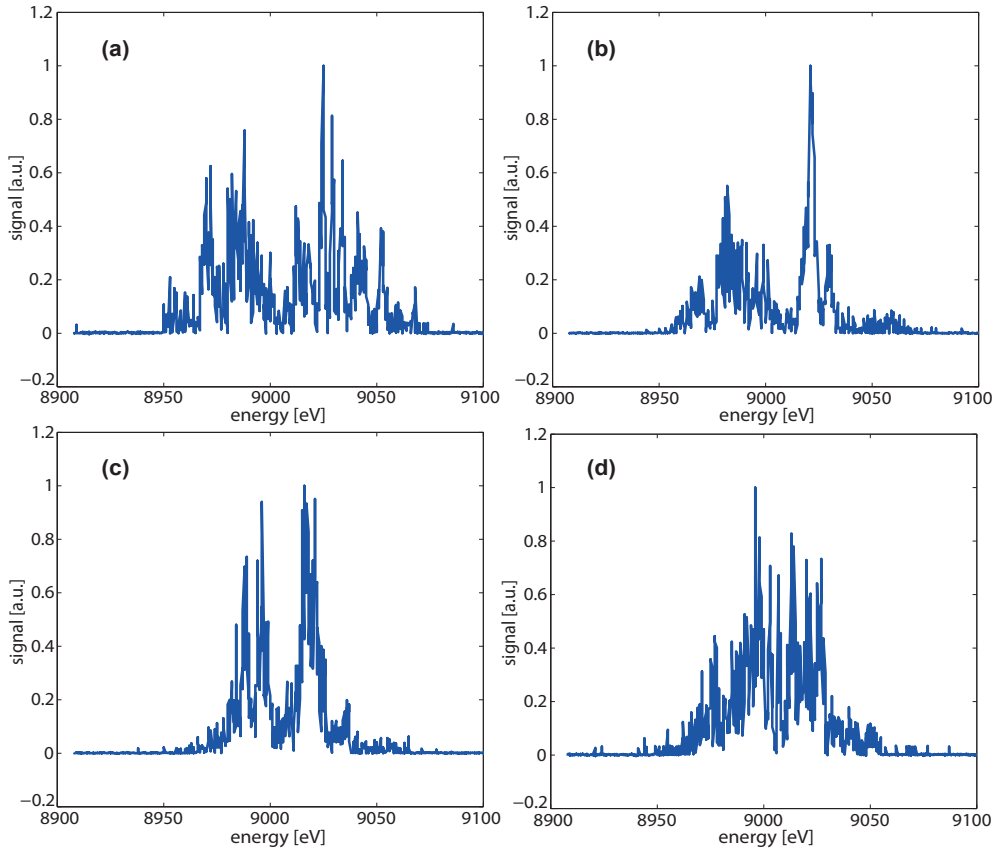


Figure 5.3: Energy spectra of different FEL pulses measured by the wide bandwidth spectrometer of SACLA.

a more realistic saturation length of about 40 m and using all the parameters of the standard operation at SACLA results in a width of a single temporal spike of at least 60 as. This means that based on the standard parameters of SACLA, the FEL pulse durations are expected to be 60 fs and longer. Such a result is in a good agreement with the pulse lengths of about 90 fs obtained from the measurements with the THz streak camera.

To summarize, the discrepancy between the two measurement methods is explained by the fact that they were measuring different things during the beam time; the spectral method of SACLA was measuring only a part of the FEL pulse due to the presence of a linear energy chirp, while the PALM setup was measuring the overall pulse length. An in-depth analysis of the FEL spectra and the lasing conditions at SACLA verifies that the photon pulse lengths cannot be as short as claimed by the spectral method, and predicts pulse durations more consistent with the values obtained from the THz streaking method.

Based on the three experiments performed during this thesis, some important conclusions can be drawn regarding the THz streaking measurement method. Measuring the photon

pulses at the HHG source and at SACLA demonstrated that the method is applicable for a wide range of photon energies changing from a few tens of electronvolts up to 10000 eV and possibly more. The setup is able to measure the arrival time and the duration of the FEL pulses with a dynamic range of about 500 fs, which depends on the frequency of the THz pulse. The measurement results and the accuracies depend greatly on the streaking strength, which is, therefore, of great importance to be defined correctly. Measuring the arrival time of the photon pulses by another technique during the THz delay scan (as done during the second beam time at SACLA) can be helpful to evaluate the streaking strength correctly and exclude the effects such as large temporal jitter and drifts between the FEL and the experimental laser beams. Good agreement between the THz field measured by PALM from the delay scan and obtained by the electro-optical sampling method during all three experiments indicates that the streaking strength was evaluated correctly during the measurements. The streaking strength depends on the electric field strength of the THz pulse and the initial kinetic energy of the photoelectrons. However, even though the electrons with higher kinetic energies are streaked more, they are measured by the eTOFs less accurately, and high initial kinetic energies of the electrons do not always mean better accuracy for the pulse length and arrival time measurement.

The experiments performed by the two experimental setups indicated that the measurement accuracy depends also on the number of measured electrons, as shown also by the simulations. In case of insufficient amount of measured electrons, the statistical fluctuations of the spectra are large, and this affects the measurement accuracy. If the spectra are reproducible as in case of the HHG pulses, an average of many spectra can be used for the calculations to reduce this effect. Meanwhile, for single-shot measurements as in case of SASE FEL beam, this effect can be important. As mentioned in chapter 3, the distance of the eTOFs from the interaction point was 20 mm larger for the second generation setup compared to the prototype setup. This fact reduces the number of electrons registered by the eTOFs and causes larger statistical fluctuations of the spectra. This is one of the reasons why the measurement accuracy was slightly worse during the measurements with the second generation setup (tables from 4.2 to 4.5).

Both the measurements and the simulations showed the importance of the method used for processing the measured data. Analysis of the measurements with the HHG source revealed that the dominant source of the uncertainties in the calculation was the fitting process of the streaked spectra with the double-peak structures from each harmonic. At the same time, during the analysis of the third measurements, the spectral widths were calculated using the standard deviation of the spectral distribution. In this case the obtained rms widths are sensitive to the shape of the spectra, and a correct range of the peak needs to be carefully defined for the calculations.

The results obtained from all three measurements were consistent to each other and to the simulation results discussed in chapter 2. The measurements showed that the THz streaking method is able to measure the arrival times and the lengths of photon pulses with wide range of photon energies for a single FEL pulse as well as for double pulses.

5.2 Outlook

As discussed in the previous section, the measurement accuracy with the THz streak camera method depends on different effects. One of the main ways to improve the accuracy and the precision is increasing the streaking strength during the measurements. This can be done by using a THz pulse with a stronger electric field. Different methods of THz generation were discussed in section 1.4. One of the ways of increasing the THz generation efficiency with the LiNbO₃ is cooling the crystal. Cooling reduces the absorption of the THz inside the crystal and increases the output power of the THz beam. A higher THz power can be achieved by using an organic crystal called DAST [64, 65]. In this case, however, the dynamic range of the measurements is smaller as the generated THz pulse has a higher frequency (smaller linear area). It is also possible to have a stronger electric field at the interaction region by applying a stronger focusing to the THz beam. In this case the effect of the Gouy phase shift becomes larger and it should be carefully accounted for.

Increasing the number of measured photoelectrons is another way of improving the accuracy and the precision of the measurements. With more photoelectrons the measured spectra are more stable and reproducible, which reduces the uncertainties in the measurements. The number of the registered electrons can be changed by the geometry of the setup. As it was found from the two measurements at SACLA, moving the eTOFs away from the interaction point increases the uncertainties in the measurements caused by a smaller number of the registered electrons. For this reason the eTOFs will be brought closer to the interaction zone in the second generation PALM, similar to the prototype setup, to increase the number of the measured electrons. It is possible to increase the number of the electrons also by increasing the ionization rate at the interaction region. By increasing the atomic density inside the gas pulses and ensuring the cluster formation of xenon atoms, more photoelectrons can be created.

Another important improvement that can be applied to the system for a better performance is the optimization of the data processing. As already seen from the performed measurements and the simulations, different data analysis methods should be utilized for different measurements. Depending on the shape and the content of the measured spectra, the optimal way should be found to characterize the parameters of the energy peaks for achieving higher accuracies.

The presence of two interaction points in the second generation PALM setup makes the system more flexible and versatile. Different types of measurements that can be performed by the second generation setup are discussed in [119]. The design of the setup allows to have a streaking THz beam at both interaction regions. If the THz pulses at the two interaction points are identical and are shifted relative to each other by 90°, the dynamic range of the measurements can be doubled. The schematic sketch of this concept is demonstrated in figure 5.4. The presence of the two THz pulses increases the temporal window, over which sensitive measurements can be performed. One can see from the figure that even when the FEL pulse (green in the figure) arrives at the peak of the first THz pulse (blue in the figure), at the second interaction region it is at the linear part of the second THz pulse (red in the figure), and the created photoelectrons experience a large streaking. Such operation can be particularly useful

when the arrival time of the FEL pulses jitters largely with respect to the experimental laser, and a large linear area is needed to accommodate all of them. This mode can be used also with shorter THz pulses of higher frequencies. In this case the overall dynamic range will remain the same as for a single THz pulse with lower frequency, but the measurements at each of the high-frequency THz pulses will have a better resolution. The modes using two similar THz

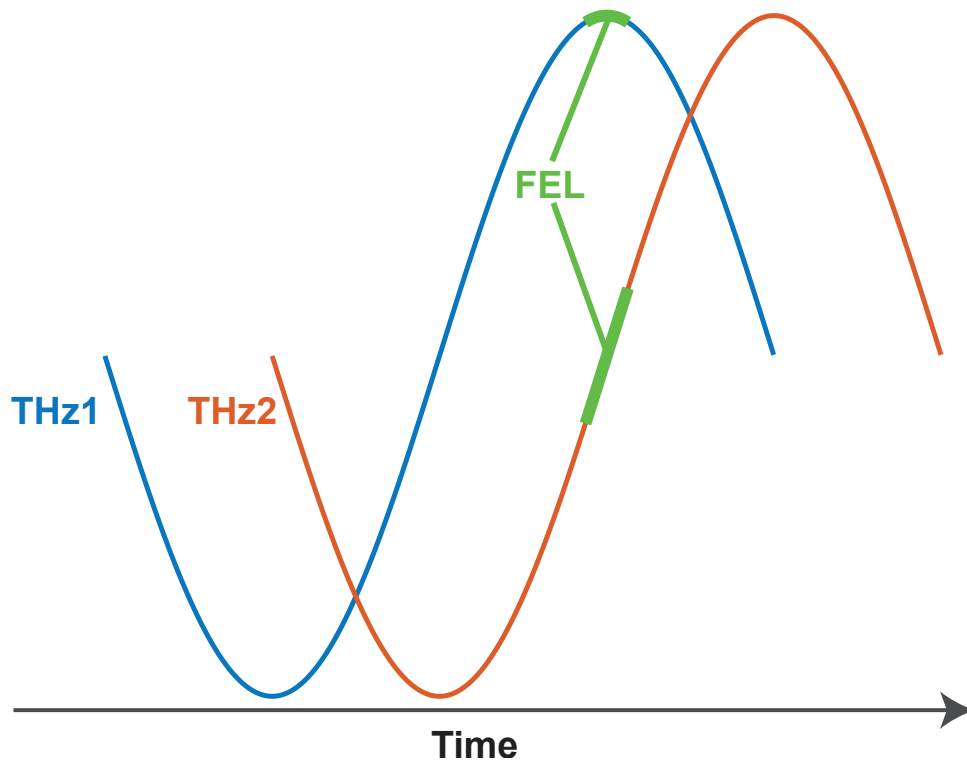


Figure 5.4: The concept of PALM performance with a large dynamic range utilizing two THz pulses with 90° shift between each other.

pulses have an additional complication of defining the correct interaction zone, where the accurate measurements are performed. This can be done using an additional arrival time monitor (as done during the second beam time at SACLA) or by carefully studying the spectra from both interaction points.

Another option of streaking at both interaction regions is to use two THz pulses of different strength and frequency as shown in figure 5.5. Using the THz pulse with a higher frequency and a stronger streaking field (shown in red in the figure) allows to perform measurements with a high resolution. However, the linear area of this pulse, where the measurements can be done is very short, and only a small number of the overall FEL pulses can be measured at that interaction point. The THz pulse with a smaller field, on the other hand, has a longer linear area and can measure most of the FEL pulses. From the arrival time measurements using the low-frequency THz pulse, it is possible to find the FEL pulses that arrive at the linear part of the high-frequency streaking pulse and are measured with a high resolution. One can see from figure 5.5 that the pulse FEL1 shown in green arrives exactly at the linear

Chapter 5. Discussion

part of the high-frequency THz pulse and corresponds to a large streaking. Meanwhile, FEL2 pulse shown in magenta in the figure completely misses the high-frequency THz pulse and is measured only by the other streaking pulse. This method can be used when high-resolution measurements are required with no need of measuring every single FEL pulse. It is worth noting that in case of operation with two streaking pulses, the non-streaked spectra are also required for single-shot measurements. The design of the second generation PALM

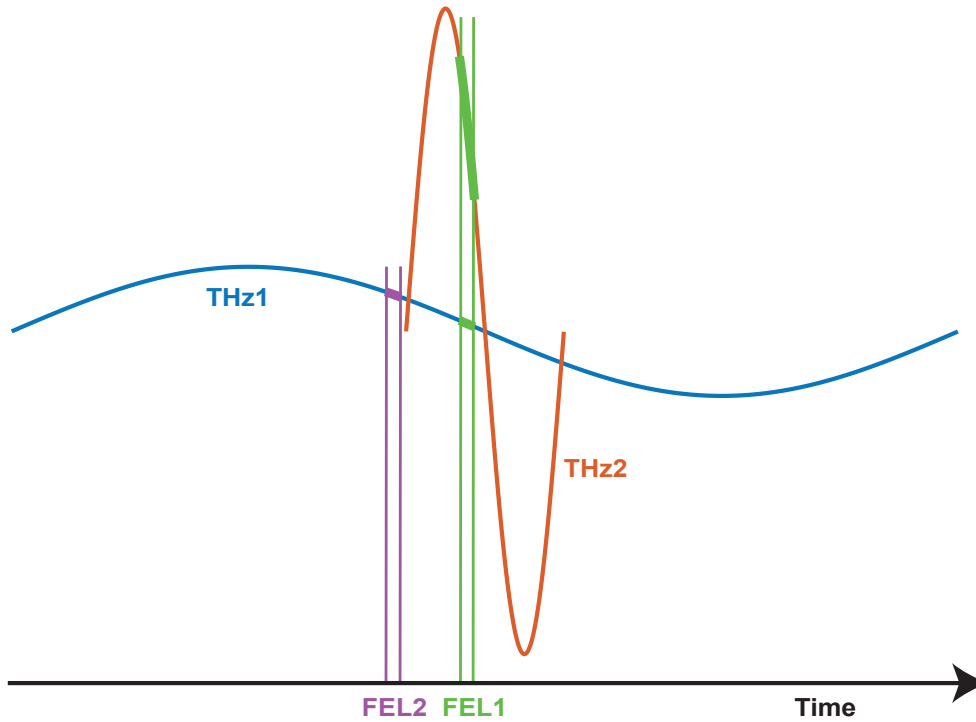


Figure 5.5: Sketch showing the concept of high-resolution measurement mode with two THz pulses. The first THz pulse has longer duration but smaller electric field, while the second one has a shorter duration but a stronger field.

is such that additional segments with a gas jet and eTOFs can be added to the current setup in future. Adding another interaction region will allow the operation of the setup with the described modes on a single-shot basis.

The second generation PALM setup is currently being installed in the beamline of SwissFEL and it will be used as an online single-pulse monitor for the temporal diagnostics of the FEL pulses.

6 Conclusion

The temporal photon diagnostics at the free electron laser facilities are of particular importance. These diagnostics allow the improvement of temporal resolution of the experiments carried out at the FEL sources and help to monitor and improve the temporal stability of the machine operation. This thesis presents a method that measures the arrival time and the duration of hard X-ray FEL pulses using the light-field streaking.

An in-depth study of the measurement method was done by simulating the photoionization and streaking processes. FEL pulses from both hard and soft X-ray regions were used in the simulation with different spectra and temporal durations. The results obtained from the simulations verified that the THz streaking method is able to measure FEL pulses of wide photon energy range with only a few femtoseconds accuracy. Different data processing methods were compared in the simulations for reconstructing the FEL pulse lengths. Based on the results provided by the simulations, various ways were pointed out for improvement of the measurements towards sub-femtosecond accuracies.

Two different experimental setups were used to perform three separate measurements with photon pulses of different properties. The prototype measurement setup had a single interaction region, where the electrons were ionized by the photon pulses and streaked by the THz field. This allowed the retrieval of the photon pulse lengths only by statistical comparison of the average widths of the streaked and non-streaked spectra or by reconstruction of the non-streaked spectral widths by indirect methods. The second generation setup was designed and assembled at PSI to achieve a single-shot measurement of the photon pulse durations. The presence of the second interaction zone in the setup allows the direct measurement of both the streaked and the non-streaked photoelectron spectra produced by the same photon pulse. Using these spectra, the lengths of single pulses were calculated without additional assumptions as used with the prototype setup. The availability of the second ionization region in the new design provides more flexibility and allows different operation modes.

The first measurements were performed with the prototype setup at a high harmonic generation beam line. The aim of the first experiment was to verify the THz streaking method for the pulse length measurements and to test the prototype setup. The first streaking was observed during the measurements and the average lengths of the HHG pulses were calculated.

Chapter 6. Conclusion

The results from the measurements showed an excellent agreement with the expected pulse duration values and with the results provided by the simulations.

The second experiment was carried out at SACLA, where SASE FEL pulses were measured. The aim of the measurements was to demonstrate the applicability of the THz streaking method in the hard X-ray region. This was the first ever evaluation of the durations and the arrival times of FEL pulses with photon energies of up to 10000 eV using the THz streaking technique. For both the arrival time and the pulse length measurements, accuracies below 10 fs were achieved. The value of the rms temporal jitter between the FEL pulses and the experimental laser pulses obtained from the measurements was in a good agreement with the expected jitter. Meanwhile, the pulse length values obtained from the measurements were longer than expected. Different explanations for the discrepancy were suggested in the thesis.

The third measurements were performed with the second generation experimental setup at SALCA. The goal was to test the new measurement setup, compare the method with other measurement techniques and to test the method with the 2-color operation. The relative arrival times measured by THz streaking were compared to the measurements from the spatial decoding setup operational at SACLA, and a good agreement was observed between the two methods. The relative jitter was consistent with the individual accuracies of the two detectors. The rms lengths of single FEL pulses were also measured during the experiments. The results were compared to the lengths reconstructed from the spectral spike width measurements. The comparison showed a large inconsistency between the two methods. The most possible explanation for such a result was the strong linear energy chirp and the complicated spectral content of the FEL pulses, which makes the measurements with the spectral method unreliable. The arrival times and the pulse durations were also measured during the 2-color operation of SACLA. The arrival times of both FEL pulses were measured and the temporal separation between them was calculated. The obtained delay values were highly correlated with the delays set by the magnetic chicane, resolving the 10 fs steps of the delay scan. The length measurements from the two FEL pulses showed that the first pulse had the same rms length as the pulses from the standard operation, while the second pulse was shorter by about 30 fs. This was the first ever simultaneous measurement of two different photon pulses.

This work has performed an in-depth analysis and characterization of the THz streaking method for the arrival time and length measurement of photon pulses. It has pushed further the applicability limits of the method demonstrating its ability to measure in a wide range of photon energies with an accuracy of only several femtoseconds. Furthermore, this work has shown that the method is capable of measuring two photon pulses of different energies at the same time. Different ways of improving the measurement accuracy and the overall performance of the setup were also discussed in the thesis.

The results provided in this work can be used to improve the temporal photon diagnostics in different FEL facilities and can contribute to further development of time-resolved experiments in femtosecond scales.

A Simulation code in MATLAB

```
1 %% defining basic quantities
2 clear all
3 % some constants
4 eV = 1.602*1e-19;
5 h = 6.62606896e-34;%in J.s
6 hbar=6.58211928e-16;% in eV*s/rad
7 fs = 1e-15;
8 hfs=hbar*2*pi/fs; % eV*fs
9 nm = 1e-9;
10 c = 3e8;
11 f_0=0.52; %1 THz
12 E_1= 6; % MV/m
13 % the streaking is given by sqrt(8*E_0*U_p)*sin(w*t)
14 % with U_p=(q^2*E_1^2)/(4*m_e*w^2)
15 U_p=sqrt(E_1^2/f_0^2)*3.34e-2;
16 chrp=0.05; % chirp in eV/fs
17 np=2.5e3; % particles per fs: 5e4/20fs
18 restof=1.2; % resolution of the eTOF 1.2 eV
19 %% spectrum from the ionization time}
20 % constructing the ionization time gaussian
21 % sigma of ionization 50 attosecond
22 tsigma=0.05;
23 trange=5; % fs
24 tn=10000; % steps
25 dt=2*trange/tn; % fs
26 ionT = dt*linspace(-tn/2,tn/2-1,tn);
27 tgauss=exp(-ionT.^2./(2*tsigma.^2)); % ionisation time Gaussian
28
29 dE = hfs/dt/tn; % eV*fs/fs = eV
30 ionE=dE.*linspace(-tn/2,tn/2-1,tn);
31 % spectrum corresponding to the ionization time of 50 as
32 Egauss=abs(ifftshift(fft(fftshift(tgauss))));
33 Esigma=(hbar/fs)/tsigma;
34 %% loading data from the pulses
35 % loading the 1st pulse
36 tic
37 files=dir('FEL pulses');
38 for lst=1:length(files)-2
39     load(['FEL pulses/' files(lst+2).name]);
40     % temporal porfile
41     % flip the direction if needed
42     if length(temp.power(:,1)) > length(temp.power(1,:))
```

Appendix A. Simulation code in MATLAB

```

43     prof = temp.power(:,end);
44     else
45         prof = temp.power(end,:);
46     end
47     prof = prof./max(prof);
48     % loading time
49     t = temp.s/c./fs; % in Femtoseconds
50     % taking only the "nonzero" part of the profile
51     tlog=logical(prof>5e-3);
52     t=t(tlog);
53     prof=prof(tlog);
54     % finding the mean point of the profile
55     tavg(lst)=sum(t.*prof')/sum(prof);
56     % rms lengths
57     tsig(lst)=sqrt(sum((t-tavg(lst)).^2.*prof')/sum(prof));
58     % centering the profile around 0
59     t=t-tavg(lst);
60     % average intensity of profile
61     meanprof(lst)=mean(prof);
62     % loading the energy
63     eng=c./(spect.x).*h./eV; % in eV
64     % taking a smaller range for faster calculation (removing the 0 tails)
65     energy=eng(int32(length(eng)/2)-2000:int32(length(eng)/2)+2000);
66     spec=spect.y(int32(length(eng)/2)-2000:int32(length(eng)/2)+2000)./max(spect.
        y);
67     % frequency for the spectrum
68     w=fs*energy./(hbar);
69     % change of sine function along the temporal profile at 0-crossing
70     ssin=sin(f_0.*1e-3.*t*2*pi);
71     chirp=chrp.*t;
72     % saving the data in a structure
73     pulse(lst).prof=prof;
74     pulse(lst).t=t;
75     pulse(lst).energy=energy;
76     pulse(lst).spec=spec;
77     % energy of the weighted average (central energy)
78     w0(lst)=sum(energy.*spec)/(sum(spec));
79     pulse(lst).w=w;
80     pulse(lst).ssin=ssin;
81     pulse(lst).chirp=chirp;
82     % uncomment to see the spectrum and temp profile of each loaded pulse
83     %     subplot(2,1,1)
84     %     plot(t, prof, 'g', t, ones(1, length(t)).*meanprof(lst), 'r')
85     %     title(['Profile #' num2str(lst)])
86     %     xlabel('time [fs]')
87     %     ylabel('signal [a.u.]')
88     %     subplot(2,1,2)
89     %     plot(energy, spec, 'r', energy, exp(-(energy-w0(lst)).^2/(2*Esigma^2)), 'g
        '),
90     %     title(['Spectrum #' num2str(lst)])
91     %     xlabel('energy [eV]')
92     %     ylabel('signal [a.u.]')
93     %     pause(0.8);
94     % emptying some variables
95     clear temp spect t w spect temp prof enlog tlog phase energy nm spec ssin
        chirp
96
97 end
98 toc
99 %% generation of spectra and streaking

```

```

100 tic
101 % number of iterations
102 iters=100;
103 % creating matrices for data
104 % lengths with Gaussian fit
105 glen=zeros(iters, length(pulse));
106 % lengths with rms
107 len=zeros(iters, length(pulse));
108 chirp1=zeros(iters, length(pulse));
109 gchirp1=zeros(iters, length(pulse));
110 Nres=zeros(iters, length(pulse));
111 for itr=1:iters
112     % defining the arrays
113     % rms spectral widths
114     sigma0=zeros(1, length(pulse));
115     sigma1=zeros(1, length(pulse));
116     sigma2=zeros(1, length(pulse));
117     sigmasq1=zeros(1, length(pulse));
118     sigmasq2=zeros(1, length(pulse));
119     % rms spectral widths from Gauss fitting
120     gsigma0=zeros(1, length(pulse));
121     gsigma1=zeros(1, length(pulse));
122     gsigma2=zeros(1, length(pulse));
123     gsigmasq1=zeros(1, length(pulse));
124     gsigmasq2=zeros(1, length(pulse));
125     % streaking strengths in fs/eV
126     slope=zeros(1, length(pulse));
127     nres0=zeros(1, length(pulse));
128     nres1=zeros(1, length(pulse));
129     nres2=zeros(1, length(pulse));
130     tic
131     for lst=1:length(pulse)
132         % number of electrons for the pulse
133         Nel=int32(np*tsig(lst));
134         % energy values of electrons
135         E0=zeros(1, Nel);
136         E1=zeros(1, Nel);
137         E2=zeros(1, Nel);
138         n=0;
139         while n<Nel
140             % random position along the photon pulse
141             tpos=randi(length(pulse(1st).t));
142             amp=rand;
143             % checking if the photon ionizes electron or not
144             if amp<=pulse(1st).prof(tpos)
145                 % resolution of the eTOF and chirp for non-streaked
146                 E0(n+1)=w0(1st)/2+randn.*Esigma+randn*restof+pulse(1st).chirp(
147                     tpos);
148                 % the chirped particles from different interaction points
149                 % without streaking
150                 Echirp1=w0(1st)/2+randn.*Esigma+pulse(1st).chirp(tpos);
151                 % adding the streak and the resolution of the eTOF
152                 E1(n+1)=Echirp1+sqrt(8.*Echirp1).*U_p.*(pulse(1st).ssin(tpos))+
153                     randn.*restof;
154                 % the same for the second detector opposite streak
155                 Echirp2=w0(1st)/2+randn.*Esigma+pulse(1st).chirp(tpos);
156                 E2(n+1)=Echirp2-sqrt(8.*Echirp2).*U_p.*(pulse(1st).ssin(tpos))+
157                     randn.*restof;
158                 n=n+1;
159             end
160         end
161     end

```

Appendix A. Simulation code in MATLAB

```

157     end
158     % getting the streaking strength
159     slope(1st)=sqrt(8*w0(1st)/2)*U_p*(pulse(1st).ssin(end)-pulse(1st).ssin(1)
        )/(pulse(1st).t(end)-pulse(1st).t(1));
160     % spectral widths
161     sigma0(1st)=std(E0);
162     sigma1(1st)=std(E1);
163     sigma2(1st)=std(E2);
164     % difference between the streaked and non-streaked spectra
165     sigmasq1(1st)=sigma1(1st)^2-sigma0(1st)^2; % eV^2
166     sigmasq2(1st)=sigma2(1st)^2-sigma0(1st)^2; % eV^2
167     % checking the length to be positive
168     if (sigmasq1(1st)+sigmasq2(1st))>= 0
169         % pulse rms length
170         len(itr, 1st)=sqrt((sigmasq1(1st)+sigmasq2(1st))/(2*slope(1st)^2));
171         % defining the chirp
172         chirp1(itr, 1st)= (sigmasq1(1st)-sigmasq2(1st))/(8*len(itr, 1st)^2*
            slope(1st));
173     else
174         % addin 0 instead of non physical values
175         len(itr, 1st)=0;
176         chirp1(itr, 1st)=0;
177     end
178     % calculating the pulse lengths with gauss fitting
179     % getting the gaussfit of the energy points for 100 pins
180     [par, resid, gfits]=histgauss(E0, 100);
181     % spectral width of non-streaked spectrum
182     gsigma0(1st)=par(3);
183     % saving the goodnes of the fit and normalizing it to the max
184     nres0(1st)=sqrt(sum(resid.^2)/(length(resid)-1));
185     nres0(1st)=nres0(1st)/max(gfits(:,2));
186     % spectral width of streaked_1 spectrum
187     [par, resid, gfits]=histgauss(E1, 100);
188     gsigma1(1st)=par(3);
189     % saving the goodnes of the fit and normalizing it to the max
190     nres1(1st)=sqrt(sum(resid.^2)/(length(resid)-1));
191     nres1(1st)=nres1(1st)/max(gfits(:,2));
192     % spectral width of streaked_2 spectrum
193     [par, resid, gfits]=histgauss(E2, 100);
194     gsigma2(1st)=par(3);
195     % saving the goodnes of the fit and normalizing it to the max
196     nres2(1st)=sqrt(sum(resid.^2)/(length(resid)-1));
197     nres2(1st)=nres2(1st)/max(gfits(:,2));
198     % defining the lengths with the gauss fits
199     % difference between the streaked and non-streaked spectra
200     gsigmasq1(1st)=gsigma1(1st)^2-gsigma0(1st)^2; % eV^2
201     gsigmasq2(1st)=gsigma2(1st)^2-gsigma0(1st)^2; % eV^2
202     % checking the length to be positive
203     if (gsigmasq1(1st)+gsigmasq2(1st))>= 0
204         % pulse rms length
205         glen(itr, 1st)=sqrt((gsigmasq1(1st)+gsigmasq2(1st))/(2*slope(1st)^2))
            ;
206         % defining the chirp
207         gchirp1(itr, 1st)= (gsigmasq1(1st)-gsigmasq2(1st))/(8*glen(1st)^2*
            slope(1st));
208     else
209         % adding 0 instead of non-physical values
210         glen(itr, 1st)=0;
211         gchirp1(itr, 1st)=0;
212     end

```



```

213         EE(1st).E0=E0;
214         EE(1st).E1=E1;
215         EE(1st).E2=E2;
216         clear E0 E1 E2
217     end
218     Nres(itr, :)=sqrt(2.*nres0.^2+nres1.^2+nres2.^2);
219     clear sigma0 sigma1 sigma2 gsigma0 gsigma1 gsigma2 sigmasq1 sigmasq2
220         gsigmasq1 gsigmasq2 nres0 nres1 nres2
221     itr
222     toc/60
223 end
224 % input lengths
225 len0=tsig;
226 toc/60
227 %% averages and the stds
228 for pls=1:length(pulse)
229     % removing 0 elements corresponding to negative lengths
230     lg=logical(len(:,pls)~=0);
231     nonz(pls)=sum(lg);
232     % average lengths with standard deviations
233     meanlen(pls)=mean(len(lg, pls));
234     stdlen(pls)=std(len(lg, pls));
235     lg=logical(glen(:,pls)~=0);
236     gnonz(pls)=sum(lg);
237     % average lengths with standard deviations
238     gmeanlen(pls)=mean(glen(lg, pls));
239     gstdlen(pls)=std(glen(lg, pls));
240 end

```


Bibliography

- [1] J. Madey, “Stimulated emission of bremsstrahlung in a periodic magnetic field,” *Journal of Applied Physics*, vol. 42, no. 5, pp. 1906–1913, 1971.
- [2] W. Colson, “Theory of a free electron laser,” *Physics Letters A*, vol. 59, no. 3, pp. 187–190, 1976.
- [3] W. Ackermann, G. Asova, V. Ayvazyan, A. Azima, N. Baboi, J. Bähr, V. Balandin, B. Beutner, A. Brandt, A. Bolzmann, *et al.*, “Operation of a free-electron laser from the extreme ultraviolet to the water window,” *Nature Photonics*, vol. 1, no. 6, pp. 336–342, 2007.
- [4] P. Emma, R. Akre, J. Arthur, R. Bionta, C. Bostedt, J. Bozek, A. Brachmann, P. Bucksbaum, R. Coffee, F.-J. Decker, *et al.*, “First lasing and operation of an ångstrom-wavelength free-electron laser,” *Nature Photonics*, vol. 4, no. 9, pp. 641–647, 2010.
- [5] E. Allaria, R. Appio, L. Badano, W. Barletta, S. Bassanese, S. Biedron, A. Borga, E. Busetto, D. Castronovo, P. Cinquegrana, *et al.*, “Highly coherent and stable pulses from the fermi seeded free-electron laser in the extreme ultraviolet,” *Nature Photonics*, vol. 6, no. 10, pp. 699–704, 2012.
- [6] T. Ishikawa, H. Aoyagi, T. Asaka, Y. Asano, N. Azumi, T. Bizen, H. Ego, K. Fukami, T. Fukui, Y. Furukawa, *et al.*, “A compact x-ray free-electron laser emitting in the sub-ångstrom region,” *Nature Photonics*, vol. 6, no. 8, pp. 540–544, 2012.
- [7] J. Oh, D. Kim, E. Kim, S. Park, H. Kang, T. Lee, T. Koo, S. Chang, C. Chung, S. Nam, *et al.*, “0.3-nm sase-fel at pal,” *Nuclear Instruments and Methods in Physics Research Section A: Accelerators, Spectrometers, Detectors and Associated Equipment*, vol. 528, no. 1, pp. 582–585, 2004.
- [8] T. Lee, Y. Bae, J. Choi, J. Huang, H. Kang, M. Kim, D. Kuk, J. Oh, Y. Parc, J. Park, *et al.*, “Design and physics issues of the pal-xfel,” *JOURNAL-KOREAN PHYSICAL SOCIETY*, vol. 48, no. 4, p. 791, 2006.
- [9] M. Altarelli *et al.*, “The european x-ray free-electron laser technical design report,” tech. rep., DESY, 2007.

Bibliography

- [10] R. Ganter *et al.*, “Swissfel-conceptual design report,” tech. rep., Paul Scherrer Institute (PSI), 2010.
- [11] M. Bionta, H. Lemke, J. Cryan, J. Glowonia, C. Bostedt, M. Cammarata, J.-C. Castagna, Y. Ding, D. Fritz, A. Fry, *et al.*, “Spectral encoding of x-ray/optical relative delay,” *Optics Express*, vol. 19, no. 22, pp. 21855–21865, 2011.
- [12] T. Maltezopoulos, S. Cunovic, M. Wieland, M. Beye, A. Azima, H. Redlin, M. Krikunova, R. Kalms, U. Frühling, F. Budzyn, *et al.*, “Single-shot timing measurement of extreme-ultraviolet free-electron laser pulses,” *New Journal of Physics*, vol. 10, no. 3, p. 033026, 2008.
- [13] M. Beye, O. Krupin, G. Hays, A. Reid, D. Rupp, S. de Jong, S. Lee, W. Lee, Y.-D. Chuang, R. Coffee, *et al.*, “X-ray pulse preserving single-shot optical cross-correlation method for improved experimental temporal resolution,” *Applied Physics Letters*, vol. 100, no. 12, p. 121108, 2012.
- [14] M. Harmand, R. Coffee, M. Bionta, M. Chollet, D. French, D. Zhu, D. Fritz, H. Lemke, N. Medvedev, B. Ziaja, *et al.*, “Achieving few-femtosecond time-sorting at hard x-ray free-electron lasers,” *Nature Photonics*, vol. 7, no. 3, pp. 215–218, 2013.
- [15] C. Gahl, A. Azima, M. Beye, M. Deppe, K. Döbrich, U. Hasslinger, F. Hennies, A. Melnikov, M. Nagasono, A. Pietzsch, *et al.*, “A femtosecond x-ray/optical cross-correlator,” *Nature Photonics*, vol. 2, no. 3, pp. 165–169, 2008.
- [16] O. Krupin, M. Trigo, W. Schlotter, M. Beye, F. Sorgenfrei, J. Turner, D. Reis, N. Gerken, S. Lee, W. Lee, *et al.*, “Temporal cross-correlation of x-ray free electron and optical lasers using soft x-ray pulse induced transient reflectivity,” *Optics Express*, vol. 20, no. 10, pp. 11396–11406, 2012.
- [17] F. Tavella, N. Stojanovic, G. Geloni, and M. Gensch, “Few-femtosecond timing at fourth-generation x-ray light sources,” *Nature Photonics*, vol. 5, no. 3, pp. 162–165, 2011.
- [18] N. Hartmann, W. Helml, A. Galler, M. Bionta, J. Grünert, S. Molodtsov, K. Ferguson, S. Schorb, M. Swiggers, S. Carron, *et al.*, “Sub-femtosecond precision measurement of relative x-ray arrival time for free-electron lasers,” *Nature Photonics*, vol. 8, no. 9, pp. 706–709, 2014.
- [19] Y. Ding, C. Behrens, P. Emma, J. Frisch, Z. Huang, H. Loos, P. Krejcik, M. Wang, *et al.*, “Femtosecond x-ray pulse temporal characterization in free-electron lasers using a transverse deflector,” *Physical Review Special Topics-Accelerators and Beams*, vol. 14, no. 12, p. 120701, 2011.
- [20] Y. Inubushi, K. Tono, T. Togashi, T. Sato, T. Hatsui, T. Kameshima, K. Togawa, T. Hara, T. Tanaka, H. Tanaka, *et al.*, “Determination of the pulse duration of an x-ray free electron laser using highly resolved single-shot spectra,” *Physical Review Letters*, vol. 109, no. 14, p. 144801, 2012.

-
- [21] R. Riedel, A. Al-Shemmary, M. Gensch, T. Golz, M. Harmand, N. Medvedev, M. Prandolini, K. Sokolowski-Tinten, S. Toilekis, U. Wegner, *et al.*, “Single-shot pulse duration monitor for extreme ultraviolet and x-ray free-electron lasers,” *Nature Communications*, vol. 4, p. 1731, 2013.
- [22] E. Saldin, E. Schneidmiller, and M. Yurkov, “Optical afterburner for an x-ray free electron laser as a tool for pump-probe experiments,” *Physical Review Special Topics-Accelerators and Beams*, vol. 13, no. 3, p. 030701, 2010.
- [23] S. Düsterer, P. Radcliffe, C. Bostedt, J. Bozek, A. Cavalieri, R. Coffee, J. Costello, D. Cubaynes, L. DiMauro, Y. Ding, *et al.*, “Femtosecond x-ray pulse length characterization at the linac coherent light source free-electron laser,” *New Journal of Physics*, vol. 13, no. 9, p. 093024, 2011.
- [24] N. Medvedev, “Femtosecond x-ray induced electron kinetics in dielectrics: application for fel-pulse-duration monitor,” *Applied Physics B*, vol. 118, no. 3, pp. 417–429, 2015.
- [25] A. Einstein, “Über einen die erzeugung und verwandlung des lichtes betreffenden heuristischen gesichtspunkt,” *Annalen der Physik*, vol. 322, no. 6, pp. 132–148, 1905.
- [26] M. Shakya and Z. Chang, “Achieving 280fs resolution with a streak camera by reducing the deflection dispersion,” *Applied Physics Letters*, vol. 87, no. 4, p. 041103, 2005.
- [27] J. Feng, H. Shin, J. Nasiatka, W. Wan, A. Young, G. Huang, A. Comin, J. Byrd, and H. Padmore, “An x-ray streak camera with high spatio-temporal resolution,” *Applied Physics Letters*, vol. 91, no. 13, p. 134102, 2007.
- [28] M. Hentschel, R. Kienberger, C. Spielmann, G. Reider, N. Milosevic, T. Brabec, P. Corkum, U. Heinzmann, M. Drescher, and F. Krausz, “Attosecond metrology,” *Nature*, vol. 414, no. 6863, pp. 509–513, 2001.
- [29] M. Drescher, M. Hentschel, R. Kienberger, G. Tempea, C. Spielmann, G. Reider, P. Corkum, and F. Krausz, “X-ray pulses approaching the attosecond frontier,” *Science*, vol. 291, no. 5510, pp. 1923–1927, 2001.
- [30] J. Itatani, F. Quéré, G. Yudin, M. Ivanov, F. Krausz, and P. Corkum, “Attosecond streak camera,” *Physical Review Letters*, vol. 88, no. 17, p. 173903, 2002.
- [31] M. Uiberacker, E. Goulielmakis, R. Kienberger, A. Baltuska, T. Westerwalbesloh, U. Keineberg, U. Heinzmann, M. Drescher, and F. Krausz, “Attosecond metrology with controlled light waveforms,” *Laser Phys*, vol. 15, pp. 195–204, 2005.
- [32] B. Schütte, U. Frühling, M. Wieland, A. Azima, and M. Drescher, “Electron wave packet sampling with laser-generated extreme ultraviolet and terahertz fields,” *Optics Express*, vol. 19, no. 20, pp. 18833–18841, 2011.

Bibliography

- [33] U. Frühling, M. Wieland, M. Gensch, T. Gebert, B. Schütte, M. Krikunova, R. Kalms, F. Budzyn, O. Grimm, J. Rossbach, *et al.*, “Single-shot terahertz-field-driven x-ray streak camera,” *Nature Photonics*, vol. 3, no. 9, pp. 523–528, 2009.
- [34] M. Drescher, U. Frühling, M. Krikunova, T. Maltezopoulos, and M. Wieland, “Time-diagnostics for improved dynamics experiments at xuv fels,” *Journal of Physics B: Atomic, Molecular and Optical Physics*, vol. 43, no. 19, p. 194010, 2010.
- [35] U. Frühling, “Light-field streaking for fels,” *Journal of Physics B: Atomic, Molecular and Optical Physics*, vol. 44, no. 24, p. 243001, 2011.
- [36] I. Grguraš, A. Maier, C. Behrens, T. Mazza, T. Kelly, P. Radcliffe, S. Düsterer, A. Kazansky, N. Kabachnik, T. Tschentscher, *et al.*, “Ultrafast x-ray pulse characterization at free-electron lasers,” *Nature Photonics*, vol. 6, no. 12, pp. 852–857, 2012.
- [37] W. Helml, A. Maier, W. Schweinberger, I. Grguraš, P. Radcliffe, G. Doumy, C. Roedig, J. Gagnon, M. Messerschmidt, S. Schorb, *et al.*, “Measuring the temporal structure of few-femtosecond free-electron laser x-ray pulses directly in the time domain,” *Nature Photonics*, vol. 8, no. 12, pp. 950–957, 2014.
- [38] B. Henke, E. Gullikson, and J. Davis, “X-ray interactions: photoabsorption, scattering, transmission, and reflection at $E= 50\text{-}30,000$ eV, $Z= 1\text{-}92$,” *Atomic Data and Nuclear Data Tables*, vol. 54, no. 2, pp. 181–342, 1993.
- [39] H. Wiedemann *et al.*, *Particle Accelerator Physics*, vol. 314. Springer, 2007.
- [40] P. Schmüser, M. Dohlus, J. Rossbach, and C. Behrens, “Free-electron lasers in the ultraviolet and x-ray regime,” *Free-Electron Lasers in the Ultraviolet and X-Ray Regime: Physical Principles, Experimental Results, Technical Realization, Springer Tracts in Modern Physics*, vol. 1, 2014.
- [41] J. Jackson, *Classical Electrodynamics*. New York: J Wiley and Sons, 1962.
- [42] H. Motz, “Applications of the radiation from fast electron beams,” *Journal of Applied Physics*, vol. 22, no. 5, pp. 527–535, 1951.
- [43] G. Loew and O. Altenmueller, “Design and applications of rf separator structures at SLAC,” in *5th International Conference on High-Energy Accelerators, Frascati*, pp. 438–442, 1965.
- [44] J. Krzywinski, E. Saldin, E. Schneidmiller, and M. Yurkov, “A new method for ultra-short electron pulse-shape measurement using synchrotron radiation from a bending magnet,” *Nuclear Instruments and Methods in Physics Research Section A: Accelerators, Spectrometers, Detectors and Associated Equipment*, vol. 401, no. 2, pp. 429–441, 1997.
- [45] E. Saldin, E. Schneidmiller, and M. Yurkov, “Statistical properties of radiation from vuv and x-ray free electron laser,” *Optics Communications*, vol. 148, no. 4, pp. 383–403, 1998.

-
- [46] A. Lutman, Y. Ding, Y. Feng, Z. Huang, M. Messerschmidt, J. Wu, and J. Krzywinski, "Femtosecond x-ray free electron laser pulse duration measurement from spectral correlation function," *Physical Review Special Topics-Accelerators and Beams*, vol. 15, no. 3, p. 030705, 2012.
- [47] P. Juranić, A. Stepanov, P. Peier, C. Hauri, R. Ischebeck, V. Schlott, M. Radović, C. Erny, F. Ardana-Lamas, B. Monozslai, I. Gorgisyan, *et al.*, "A scheme for a shot-to-shot, femtosecond-resolved pulse length and arrival time measurement of free electron laser x-ray pulses that overcomes the time jitter problem between the fel and the laser," *Journal of Instrumentation*, vol. 9, no. 03, p. P03006, 2014.
- [48] F. Quéré, Y. Mairesse, and J. Itatani, "Temporal characterization of attosecond xuv fields," *Journal of Modern Optics*, vol. 52, no. 2-3, pp. 339–360, 2005.
- [49] U. Frühling, *Lichtfeld getriebene Streak-Kamera zur Einzelschuss Zeitstrukturmessung der XUV-Pulse eines Freie-Elektronen Lasers*. PhD thesis, DESY, 2009.
- [50] N. Stojanovic and M. Drescher, "Accelerator-and laser-based sources of high-field terahertz pulses," *Journal of Physics B: Atomic, Molecular and Optical Physics*, vol. 46, no. 19, p. 192001, 2013.
- [51] M. Bass, P. Franken, J. Ward, and G. Weinreich, "Optical rectification," *Physical Review Letters*, vol. 9, no. 11, p. 446, 1962.
- [52] R. W. Boyd, *Nonlinear optics*. Academic press, 2003.
- [53] Y. Shen, "Recent advances in nonlinear optics," *Reviews of Modern Physics*, vol. 48, no. 1, p. 1, 1976.
- [54] A. Nahata, A. S. Weling, and T. F. Heinz, "A wideband coherent terahertz spectroscopy system using optical rectification and electro-optic sampling," *Applied Physics Letters*, vol. 69, no. 16, pp. 2321–2323, 1996.
- [55] J. Hebling, G. Almasi, I. Kozma, and J. Kuhl, "Velocity matching by pulse front tilting for large area thz-pulse generation," *Optics Express*, vol. 10, no. 21, pp. 1161–1166, 2002.
- [56] J. Hebling, "Derivation of the pulse front tilt caused by angular dispersion," *Optical and Quantum Electronics*, vol. 28, no. 12, pp. 1759–1763, 1996.
- [57] K. Ravi, W. R. Huang, S. Carbajo, X. Wu, and F. Kärtner, "Limitations to thz generation by optical rectification using tilted pulse fronts," *Optics Express*, vol. 22, no. 17, pp. 20239–20251, 2014.
- [58] Q. Meng, R. Ye, Z. Zhong, J. Yu, and B. Zhang, "Analysis on thz radiation generation efficiency in optical rectification by tilted-pulse-front pumping," *Journal of Infrared, Millimeter, and Terahertz Waves*, vol. 36, no. 9, pp. 866–875, 2015.

Bibliography

- [59] A. G. Stepanov, L. Bonacina, S. V. Chekalin, and J.-P. Wolf, "Generation of 30 μJ single-cycle terahertz pulses at 100 Hz repetition rate by optical rectification," *Optics Letters*, vol. 33, no. 21, pp. 2497–2499, 2008.
- [60] H. Hirori, A. Doi, F. Blanchard, and K. Tanaka, "Single-cycle terahertz pulses with amplitudes exceeding 1 MV/cm generated by optical rectification in LiNbO₃," *Applied Physics Letters*, vol. 98, no. 9, p. 091106, 2011.
- [61] M. Kunitski, M. Richter, M. D. Thomson, A. Vredenburg, J. Wu, T. Jahnke, M. Schöffler, H. Schmidt-Böcking, H. G. Roskos, and R. Dörner, "Optimization of single-cycle terahertz generation in LiNbO₃ for sub-50 femtosecond pump pulses," *Optics Express*, vol. 21, no. 6, pp. 6826–6836, 2013.
- [62] C. Vicario, B. Monoszlai, C. Lombosi, A. Mareczko, A. Courjaud, J. Fülöp, and C. Hauri, "Pump pulse width and temperature effects in lithium niobate for efficient THz generation," *Optics Letters*, vol. 38, no. 24, pp. 5373–5376, 2013.
- [63] F. Blanchard, X. Ropagnol, H. Hafez, H. Razavipour, M. Bolduc, R. Morandotti, T. Ozaki, and D. Cooke, "Effect of extreme pump pulse reshaping on intense terahertz emission in lithium niobate at multimillijoule pump energies," *Optics Letters*, vol. 39, no. 15, pp. 4333–4336, 2014.
- [64] C. P. Hauri, C. Ruchert, C. Vicario, and F. Ardana, "Strong-field single-cycle thz pulses generated in an organic crystal," *Applied Physics Letters*, vol. 99, no. 16, p. 161116, 2011.
- [65] C. Ruchert, C. Vicario, and C. P. Hauri, "Scaling submillimeter single-cycle transients toward megavolts per centimeter field strength via optical rectification in the organic crystal oh1," *Optics Letters*, vol. 37, no. 5, pp. 899–901, 2012.
- [66] F. Junginger, A. Sell, O. Schubert, B. Mayer, D. Brida, M. Marangoni, G. Cerullo, A. Leitenstorfer, and R. Huber, "Single-cycle multiterahertz transients with peak fields above 10 mv/cm," *Optics Letters*, vol. 35, no. 15, pp. 2645–2647, 2010.
- [67] J. Hebling, A. Stepanov, G. Almási, B. Bartal, and J. Kuhl, "Tunable THz pulse generation by optical rectification of ultrashort laser pulses with tilted pulse fronts," *Applied Physics B*, vol. 78, no. 5, pp. 593–599, 2004.
- [68] F. Ardana-Lamas, C. Erny, A. G. Stepanov, I. Gorgisyan, P. Juranić, R. Abela, and C. P. Hauri, "Temporal characterization of individual harmonics of an attosecond pulse train by thz streaking," *Physical Review A*, vol. 93, p. 043838, 2016.
- [69] A. McPherson, G. Gibson, H. Jara, U. Johann, T. S. Luk, I. McIntyre, K. Boyer, and C. K. Rhodes, "Studies of multiphoton production of vacuum-ultraviolet radiation in the rare gases," *JOSA B*, vol. 4, no. 4, pp. 595–601, 1987.
- [70] M. Ferray, A. L'Huillier, X. Li, L. Lompre, G. Mainfray, and C. Manus, "Multiple-harmonic conversion of 1064 nm radiation in rare gases," *Journal of Physics B: Atomic, Molecular and Optical Physics*, vol. 21, no. 3, p. L31, 1988.

- [71] P. B. Corkum, "Plasma perspective on strong field multiphoton ionization," *Physical Review Letters*, vol. 71, no. 13, p. 1994, 1993.
- [72] M. Ammosov, N. Delone, and V. Krainov, "Tunnel ionization of complex atoms and atomic ions in a varying electromagnetic field," *Zhurnal Eksperimentalnoi I Teoreticheskoi Fiziki*, vol. 91, no. 6, pp. 2008–2013, 1986.
- [73] A. L'Huillier, K. J. Schafer, and K. C. Kulander, "Theoretical aspects of intense field harmonic generation," *Journal of Physics B: Atomic, Molecular and Optical Physics*, vol. 24, no. 15, p. 3315, 1991.
- [74] A. L'Huillier, K. Schafer, and K. Kulander, "Higher-order harmonic generation in xenon at 1064 nm: The role of phase matching," *Physical Review Letters*, vol. 66, no. 17, p. 2200, 1991.
- [75] A. L'Huillier, M. Lewenstein, P. Salieres, P. Balcou, M. Y. Ivanov, J. Larsson, and C.-G. Wahlström, "High-order harmonic-generation cutoff," *Physical Review A*, vol. 48, no. 5, p. R3433, 1993.
- [76] M. Lewenstein, P. Balcou, M. Y. Ivanov, A. L'hullier, and P. B. Corkum, "Theory of high-harmonic generation by low-frequency laser fields," *Physical Review A*, vol. 49, no. 3, p. 2117, 1994.
- [77] I. Gorgisyan, R. Ischebeck, E. Prat, S. Reiche, L. Rivkin, and P. Juranić, "Simulation of fel pulse length calculation with thz streaking method," *Journal of Synchrotron Radiation*, vol. 23, no. 3, 2016.
- [78] P. Juranić, A. Stepanov, R. Ischebeck, V. Schlott, C. Pradervand, L. Patthey, M. Radović, I. Gorgisyan, L. Rivkin, C. Hauri, *et al.*, "High-precision x-ray fel pulse arrival time measurements at sacla by a thz streak camera with xe clusters," *Optics Express*, vol. 22, no. 24, pp. 30004–30012, 2014.
- [79] M. Schultze, M. Fieß, N. Karpowicz, J. Gagnon, M. Korbman, M. Hofstetter, S. Neppl, A. L. Cavalieri, Y. Komninos, T. Mercouris, *et al.*, "Delay in photoemission," *Science*, vol. 328, no. 5986, pp. 1658–1662, 2010.
- [80] J. Dahlström, T. Carette, and E. Lindroth, "Diagrammatic approach to attosecond delays in photoionization," *Physical Review A*, vol. 86, no. 6, p. 061402, 2012.
- [81] A. Kheifets, "Time delay in valence-shell photoionization of noble-gas atoms," *Physical Review A*, vol. 87, no. 6, p. 063404, 2013.
- [82] D. Guenot, D. Kroon, E. Balogh, E. Larsen, M. Kotur, M. Miranda, T. Fordell, P. Johnsson, J. Mauritsson, M. Gisselbrecht, *et al.*, "Measurements of relative photoemission time delays in noble gas atoms," *Journal of Physics B: Atomic, Molecular and Optical Physics*, vol. 47, no. 24, p. 245602, 2014.

Bibliography

- [83] J. M. Dahlström, M. Vacher, A. Maquet, J. Caillat, and S. Haessler, “Photoionization time delays,” in *Ultrafast Dynamics Driven by Intense Light Pulses*, pp. 177–202, Springer, 2016.
- [84] A. Kheifets, S. Saha, P. Deshmukh, D. Keating, and S. Manson, “Dipole phase and photoelectron group delay in inner-shell photoionization,” *Physical Review A*, vol. 92, no. 6, p. 063422, 2015.
- [85] M. Wellhöfer, J. T. Hoeft, M. Martins, W. Wurth, M. Braune, J. Viefhaus, K. Tiedtke, and M. Richter, “Photoelectron spectroscopy as a non-invasive method to monitor sase-fel spectra,” *Journal of Instrumentation*, vol. 3, no. 02, p. P02003, 2008.
- [86] S. Reiche, “Genesis 1.3: a fully 3d time-dependent fel simulation code,” *Nuclear Instruments and Methods in Physics Research Section A: Accelerators, Spectrometers, Detectors and Associated Equipment*, vol. 429, no. 1, pp. 243–248, 1999.
- [87] A. Kondratenko and E. Saldin, “Generating of coherent radiation by a relativistic electron beam in an undulator,” *Part. Accel.*, vol. 10, pp. 207–216, 1980.
- [88] R. Bonifacio, C. Pellegrini, and L. Narducci, “Collective instabilities and high-gain regime in a free electron laser,” *Optics Communications*, vol. 50, no. 6, pp. 373–378, 1984.
- [89] J. Feldhaus, E. Saldin, J. Schneider, E. Schneidmiller, and M. Yurkov, “Possible application of x-ray optical elements for reducing the spectral bandwidth of an x-ray sase fel,” *Optics Communications*, vol. 140, no. 4, pp. 341–352, 1997.
- [90] E. Saldin, E. Schneidmiller, Y. V. Shvyd’ko, and M. Yurkov, “X-ray fel with a mev bandwidth,” *Nuclear Instruments and Methods in Physics Research Section A: Accelerators, Spectrometers, Detectors and Associated Equipment*, vol. 475, no. 1, pp. 357–362, 2001.
- [91] G. Geloni, V. Kocharyan, and E. Saldin, “A simple method for controlling the line width of sase x-ray fels,” *arXiv preprint arXiv:1004.4067*, 2010.
- [92] J. Amann, W. Berg, V. Blank, F.-J. Decker, Y. Ding, P. Emma, Y. Feng, J. Frisch, D. Fritz, J. Hastings, *et al.*, “Demonstration of self-seeding in a hard-x-ray free electron laser,” *Nature Photonics*, vol. 6, no. 10, pp. 693–698, 2012.
- [93] W. R. Gilks and P. Wild, “Adaptive rejection sampling for gibbs sampling,” *Applied Statistics*, pp. 337–348, 1992.
- [94] C. Robert and G. Casella, *Monte Carlo statistical methods*. Springer Science & Business Media, 2013.
- [95] K. Tono, T. Togashi, Y. Inubushi, T. Sato, T. Katayama, K. Ogawa, H. Ohashi, H. Kimura, S. Takahashi, K. Takeshita, *et al.*, “Beamline, experimental stations and photon beam diagnostics for the hard x-ray free electron laser of sacla,” *New Journal of Physics*, vol. 15, no. 8, p. 083035, 2013.

-
- [96] D. J. Kennedy and S. T. Manson, "Photoionization of the noble gases: cross sections and angular distributions," *Physical Review A*, vol. 5, no. 1, p. 227, 1972.
- [97] O. Hemmers, M. Blackburn, T. Goddard, P. Glans, H. Wang, S. Whitfield, R. Wehlitz, I. Sellin, and D. W. Lindle, "Dipole and nondipole angular-distribution effects in valence photoemission from neon," *Journal of Electron Spectroscopy and Related Phenomena*, vol. 123, no. 2, pp. 257–264, 2002.
- [98] D. Irimia, D. Dobrikov, R. Kortekaas, H. Voet, D. A. van den Ende, W. A. Groen, and M. H. Janssen, "A short pulse (7 μ s fwhm) and high repetition rate (dc-5kHz) cantilever piezovalve for pulsed atomic and molecular beams," *Review of Scientific Instruments*, vol. 80, no. 11, p. 113303, 2009.
- [99] D. Irimia, R. Kortekaas, and M. H. Janssen, "In situ characterization of a cold and short pulsed molecular beam by femtosecond ion imaging," *Physical Chemistry Chemical Physics*, vol. 11, no. 20, pp. 3958–3966, 2009.
- [100] O. Hagena and W. Obert, "Cluster formation in expanding supersonic jets: effect of pressure, temperature, nozzle size, and test gas," *The Journal of Chemical Physics*, vol. 56, no. 5, pp. 1793–1802, 1972.
- [101] O. Hemmers, S. Whitfield, P. Glans, H. Wang, D. W. Lindle, R. Wehlitz, and I. A. Sellin, "High-resolution electron time-of-flight apparatus for the soft x-ray region," *Review of Scientific Instruments*, vol. 69, no. 11, pp. 3809–3817, 1998.
- [102] D. A. Dahl, "Simion for the personal computer in reflection," *International Journal of Mass Spectrometry*, vol. 200, no. 1, pp. 3–25, 2000.
- [103] A. D. Appelhans and D. A. Dahl, "Simion ion optics simulations at atmospheric pressure," *International Journal of Mass Spectrometry*, vol. 244, no. 1, pp. 1–14, 2005.
- [104] L. G. Gouy, *Sur une propriété nouvelle des ondes lumineuses*. Gauthier-Villars, 1890.
- [105] L. G. Gouy, "Sur la propagation anormale des ondes," *Ann. Chim. Phys.*, vol. 24, pp. 145–213, 1891.
- [106] R. W. Boyd, "Intuitive explanation of the phase anomaly of focused light beams," *JOSA*, vol. 70, no. 7, pp. 877–880, 1980.
- [107] A. Ruffin, J. Rudd, J. Whitaker, S. Feng, and H. Winful, "Direct observation of the gouy phase shift with single-cycle terahertz pulses," *Physical Review Letters*, vol. 83, no. 17, p. 3410, 1999.
- [108] S. Feng and H. G. Winful, "Physical origin of the gouy phase shift," *Optics Letters*, vol. 26, no. 8, pp. 485–487, 2001.

Bibliography

- [109] U. Flechsig, A. Jaggi, S. Spielmann, H. Padmore, and A. MacDowell, “The optics beamline at the swiss light source,” *Nuclear Instruments and Methods in Physics Research Section A: Accelerators, Spectrometers, Detectors and Associated Equipment*, vol. 609, no. 2, pp. 281–285, 2009.
- [110] J. Mauritsson, P. Johnsson, R. López-Martens, K. Varju, W. Kornelis, J. Biegert, U. Keller, M. Gaarde, K. Schafer, and A. L’Huillier, “Measurement and control of the frequency chirp rate of high-order harmonic pulses,” *Physical Review A*, vol. 70, no. 2, p. 021801, 2004.
- [111] K. Varjú, Y. Mairesse, B. Carré, M. Gaarde, P. Johnsson, S. Kazamias, R. López-Martens, J. Mauritsson, K. Schafer, P. Balcou, *et al.*, “Frequency chirp of harmonic and attosecond pulses,” *Journal of Modern Optics*, vol. 52, no. 2-3, pp. 379–394, 2005.
- [112] Z. Lu, P. Campbell, and X.-C. Zhang, “Free-space electro-optic sampling with a high-repetition-rate regenerative amplified laser,” *Applied Physics Letters*, vol. 71, no. 5, pp. 593–595, 1997.
- [113] H. Ohashi, M. Yabashi, K. Tono, Y. Inubushi, T. Sato, T. Togashi, Y. Senba, T. Koyama, H. Yumoto, K. Miyokawa, *et al.*, “Beamline mirrors and monochromator for x-ray free electron laser of sacla,” *Nuclear Instruments and Methods in Physics Research Section A: Accelerators, Spectrometers, Detectors and Associated Equipment*, vol. 710, pp. 139–142, 2013.
- [114] C. T. Kelley, *Iterative methods for optimization*, vol. 18. Siam, 1999.
- [115] T. Katayama, S. Owada, T. Togashi, K. Ogawa, P. Karvinen, I. Vartiainen, A. Eronen, C. David, T. Sato, K. Nakajima, *et al.*, “A beam branching method for timing and spectral characterization of hard x-ray free-electron lasers,” *Structural Dynamics*, vol. 3, no. 3, p. 034301, 2016.
- [116] T. Sato, T. Togashi, K. Ogawa, T. Katayama, Y. Inubushi, K. Tono, and M. Yabashi, “Highly efficient arrival timing diagnostics for femtosecond x-ray and optical laser pulses,” *Applied Physics Express*, vol. 8, no. 1, p. 012702, 2014.
- [117] M. Yabashi, J. B. Hastings, M. S. Zolotarev, H. Mimura, H. Yumoto, S. Matsuyama, K. Yamauchi, and T. Ishikawa, “Single-shot spectrometry for x-ray free-electron lasers,” *Physical review letters*, vol. 97, no. 8, p. 084802, 2006.
- [118] T. Hara, Y. Inubushi, T. Katayama, T. Sato, H. Tanaka, T. Tanaka, T. Togashi, K. Togawa, K. Tono, M. Yabashi, *et al.*, “Two-colour hard x-ray free-electron laser with wide tunability,” *Nature communications*, vol. 4, 2013.
- [119] I. Gorgisyan, P. Juranic, R. Ischebeck, A. Stepanov, V. Schlott, C. Pradervand, L. Patthey, M. Radovic, R. Abela, C. Hauri, *et al.*, “The new design of the thz streak camera at psi,” in *SPIE Optics+ Optoelectronics*, pp. 95120D–95120D, International Society for Optics and Photonics, 2015.

Personal information

Name Ishkhan Gorgisyan
Address Albulagasse 8, Brugg AG 5200, Switzerland
Phone +41 78 902 06 87
Email ishkhan.gorgisyan@psi.ch
Date of birth 02 March 1989
Nationality Armenian

Education

2013-present École polytechnique fédérale de Lausanne (EPFL)
Route Cantonale, 1015 Lausanne, Switzerland
Doctoral student

2011-2013 École polytechnique fédérale de Lausanne (EPFL)
Route Cantonale, 1015 Lausanne, Switzerland
Master in Applied Physics

2006-2010 Yerevan State University, Faculty of Physics
Alex Manoogian 1, Yerevan, Armenia
Bachelor in Physics and Pedagogy

Projects and Thesis

Master thesis (2013) *“Characterisation of electron beams with coherent diffraction radiation”*, GFA, PSI, Villigen, Switzerland

Internship (2012) *“Implementation and commissioning of a moving wire system for the SwissFEL magnets”*, GFA, PSI, Villigen, Switzerland

Semester project (2012) *“SwissFEL Injector beam diagnostics with SR and cross-shaped band-pass filters”*, GFA, PSI, Villigen, Switzerland

Semester project (2011) *“A feedback system for beam stability in CTF3, Test Beam Line”*, CTF3, CLIC, CERN, Geneva, Switzerland

Bachelor thesis (2010) “*Laser-electron beam interaction in the undulator*”, Center for the Advancement of Natural Discoveries using Light Emission (CANDLE), Yerevan, Armenia

Work experience

10.2013-12.2016 Doctoral student, Diagnostics section, Paul Scherrer Institut (PSI), Villigen, Switzerland

09.2010-07.2011 Senior lab assistant, Center for the Advancement of Natural Discoveries using Light Emission (CANDLE), Yerevan, Armenia

02.2010-07.2011 Physicist, Engineering of Safety Ltd (attached to the Armenian Nuclear Power Station), Yerevan, Armenia

List of publications

May 2016, first author Simulation of FEL pulse length calculation with THz streaking method, *Journal of Synchrotron Radiation*, 23, 643-651, 2016

April 2016, co-author Temporal characterization of individual harmonics of an attosecond pulse train by THz streaking, *Physical Review A*, 93, 043838, 2016

May 2015, first author The new design of the THz streak camera at PSI, *Proceeding at SPIE Optics+ Optoelectronics*, 95120D– 95120D, 2015

December 2014, co-author High-precision X-ray FEL pulse arrival time measurements at SACLA by a THz streak camera with Xe clusters, *Optics Express*, 22(24), 30004–30012, 2014

March 2014, co-author A scheme for a shot-to-shot, femtosecond resolved pulse length and arrival time measurement of free electron laser X-ray pulses that overcomes the time jitter problem between the FEL and the laser, *Journal of Instrumentation*, 9(03), P03006, 2014

Courses and Schools

09.2015-10.2015	CERN Accelerator School, Course: <i>Advanced Accelerator physics</i>
06.2015	U.S. Particle Accelerator School, Courses: 1. <i>Linear Accelerator Design for Free Electron Lasers</i> , 2. <i>Project Management for Scientists and Engineers</i>
11.2014	CERN Accelerator School, Course: <i>Plasma Wake Acceleration</i>
09.2014-10.2014	<i>LA3NET Advanced School of Laser Applications at Accelerators</i>
01.2014	U.S. Particle Accelerator School, Course: <i>Accelerator Physics</i>
09.2009-05.2010	USAID Armenia and EIF school, Courses: <i>Web technologies, PHP, JAVA, OOP, Data bases</i>

Languages

English (fluent), **German** (good), **French** (basic), **Russian** (fluent), **Armenian** (native)

Programming Skills

MATLAB (everyday use), Mathematica (good knowledge), Python (basic knowledge), C++ (basic knowledge)

Other Programs

Microsoft Office (Word, Excel, PowerPoint, Outlook), LaTeX (everyday use), Adobe Illustrator (good knowledge), COMSOL Multiphysics (basic knowledge), Elegant particle tracking code (basic knowledge).

References

Prof. Leonid Rivkin	EPFL, PSI: leonid.rivkin@epfl.ch , leonid.rivkin@psi.ch .
Dr. Rasmus Ischebeck	PSI: rasmus.ischebeck@psi.ch .
Dr. Pavle Juranic	PSI: pavle.juranic@psi.ch .